Alma Mater Studiorum · Università di Bologna

School of Science
Department of Physics and Astronomy
Master Degree Program in
Astrophysics and Cosmology

Adaptive Optics corrected simulations of star forming clumps observations at high-z for MORFEO/MICADO@ELT

Graduation Thesis

Presented by:
Alessio Taranto

Supervisor:
Chiar.mo Prof. Leonardo Testi

Co-Supervisors:
Dott.ssa Francesca Annibali
Dott.ssa Anita Zanella

Accademic Year 2023/24

Abstract

In the framework of galaxy formation, the star-forming regions, typicaly dubbed as clumps, play an important role in the definition of the galaxy properties observed today. Clumps have been observed from cosmic noon ($z \approx 1$) up to the highest redshift (up to $z \approx 10$). To study them, high spatial resolution and sensitivity are needed, given their small size and faintness. Thanks to the unprecedented dimension of the next generation of telescopes, it will be possible to investigate the smallest and faintest objects in the universe. With the help of Adaptive Optics systems, the seeing effect introduced by the atmospheric turbulence can be compensated, allowing near-diffraction limit observations also from ground-based observatories. In this work I focus on studying the possibility of observing and resolving star forming clumps using the ELT. In particular I focus on the simulation of the PSF that is expected to be obtained from the Adaptive Optics module MORFEO in the case of different natural guide star configurations, and on the effects that different configurations will have on the observations. Then I explore how the combination of different observing conditions and intrinsic properties of the targets (photometric filter, NGS asterism, source surface brightness and redshift) will impact the scientific performance of the Near-Infrared imager MICADO, fed with MORFEO-corrected wavefront.

The scientific case taken into exam is the detection and characterization of star-forming clumps with size < 10 pc at different redshifts up to z=6. This will be accomplished through specific software developed for the prediction of adaptive optics PSF and for the simulation of MICADO+MORFEO data.

Starting from well motivated assumptions on star forming clumps and their host galaxies, I produced simulated data of these systems in the I, J, H and K MICADO bands at different redshifts. Then I analyzed the simulated data to characterize how well the clumps can be detected and characterized on particular observing conditions and target properties. This work provides a first step for preparing to real on-sky observations of high-z star forming clumps in the near future.

Contents

Chapter 1

Introduction to star forming clumps

High-redshift galaxies mostly experience star formation processes over long timescales, being the merger-driven events only a minority. The study of the morphology of galaxies at different redshifts offers powerful tools to investigate galaxy formation and evolution. Nearby starburst galaxies are often considered to be local analogs to high-redshift primeval gaalxies (e.g., Adamo et al 2011; Bian et al 2016) thus using them can help to better understand how their distant counterparts behave. Having insights on distant galaxies properties from their "local twins" could help to define the best observing strategies to be used when studying them.

High-redshift galaxies have a sustantially higher gas fraction with respect to local galaxies (e.g., Tacconi et al 2010; Scoville et al 2023). This, combined with their higher density, leads to violent instabilities in the proto-disk structure, resulting in disk fragmentation. These phenomena causes these galaxies to have very clumpy and irregular morphologies (e.g. Cervino et al 2010). While local galaxies are mainly categorized in the three morphological classes proposed in the Hubble classification (i.e. spirals, spheroids and irregulars (Hubble 1926)), more distant ones host several bright spots and are dominated by massive and bright structures called *clumps*, which are defined as areas with elevated specific star formation rates. Clumps are generally luminous in the rest-frame UV band, due to the strong star formation processes which they host. When searching for them at high-z, one shuold go into Near-Infrared (NIR) bands to catch the peak produced from young and massive stars.

Studies from local starburst galaxies suggest that the hierarchical nature of star formation processes increases as the spatial resolution increases (Elmegreen et al 2014). In the local Universe it is possible to observe and resolve star forming regions up to the parsec scales. For high-redshift galaxies, this is possible with present instrumentations only in the cases of gravitationally lensed system, where spatial resolution is gained thanks to the magnification produced by the lens.

Two different mechanisms have been proposed to explain clumps' formation: 1. violent disk instability (Dekel et al 09a, 13) and 2. galaxy mergers as a trigger for gas collapse and clump assembly (Di Matteo et al 08). These two channels are also known as "in-situ" and "ex-situ" formation mechanisms. Despite their origins, the fate of the clumps can determine the future morphology of the host galaxy, and can have important feedback effect on the galaxy environment. Different studies and numerical simulations (e.g., Immeli et al. 2004a, 2004b; Dekel et al. 2009a; Ceverino et al. 2012) predict that clumps, regardless of their in-situ or ex-situ formation, migrate towards the galactic center due to dynamical friction, thus contributing to the formation of the galaxy proto-bulge. Instead, other studies (e.g., Di Matteo et al 2008) suggest that clumps can not make their way up to the central regions of their host galaxy; instead, they end up destroyed by the feedback process produced by the most massive stars present in the clumps itself or by galactic feedback. In that way, what remains of the clumps goes into the formation of the galactic disk.

Understanding how clumps form and evolve with redshift is a key point in today studies of galaxy formation and evolution. We need to probe the very high redshift domain to better understand the formation of the first luminous objects, which were the first to shine in the Universe and played a key role in the reionization epoch. That is when simulations (Reina-Campos et al 2022) predict the formation of the first proto-globular clusters, containing the first stars, i.e. the hypotetic population III stars.

To perform these kind of studies, high spatial resolution and high contrast imaging techniques are required. This allows to break clumps into their foundamental components, so that their behavior and their formation can be investigated. At the moment the James Webb Space Telescope (JWST) and the Hubble Space Telescope (HST) are the two existing facilities that offer the required sensitivity and spatial resolution to study such systems in

detail. In the next future, thanks to the new generation of large telescopes, the scientific community will have the opportunity to use more sophisticated instrumentations and gain knowledge on still open astrophysics problems, such as those mentioned above.

1.1 Aims and goals of the thesis

This thesis enters in the field of galaxy formation and evolution from a technical point of view, exploring the specific scientific case about the possibility to detect parsec-scale star forming clumps in high-redshift galaxies. In particular, the performance of the MICADO+MORFEO instrument[1] will be simulated, in order to study which observational parameters will affect real observations the most.

This is the first time that the impact of the adopted Natural Guide Star configuration used in MORFEO, is tested against a scientific case. This is a crucial step since we aim at assesing the realistic capabilities of the instrument while performing observations of high redshift star-forming clumps under a variety of observing conditions and availability of NGSs, which are required to perform adaptive optics correction. The MORFEO AO-corrected PSF will be simulated using a set of asterisms proposed to us by the ESO staff, and the goodness of the correction will be estimated and discussed. Here the goal is to understand which are the asterism parameters, among magnitude, relative position of the NGSs and their proximity to the science field of view, that impact the most the goodness of the AO correction.

These evaluations have been done first by looking at the performance related parameters describing the instrumental PSF (such as FWHM and Strehl ratio) and then by appliyng the AO-corrected PSF to a real scientific case.

Here it comes the second part of the thesis, with more scientific oriented goals about the detection of star forming clumps at different redshifts. Using observation simulators specifically designed for this goal, ELT-like data have been produced and the ability of the system to detect parsec scale clumps has been studied and discussed. The goal is to understand up to which redshift the ELT, coupled with the MICADO+MORFEO, instrument will be able to observe and eventually resolve clumps. In addition, also the effects of using

[1]First generation ELT imager and its related adaptive optics module

different NGS asterisms has been explored, in order to understand how this will impact the clump dtectability.

Last, a brief discussion on the ability of the system to resolve close clumps is carried out. In recent studies clumps obseved at high redshift, even with gravitational lensing, are resolved up to a > 10 pc scale (Vanzella et al 2023). With more spatial resolution, they might come out as composed by even smaller components, a scenario which is briefly explored and discussed in the very last part of the thesis.

Summarizing the goals and the expected final results of this work, we have explored:

- The role of the adopted NGS asterism on the ability of the instrument MORFEO to correct the incoming astronmical wavefront from the effects of the atmospheric turbulence;
- The limits and capability of MICADO+MORFEO to detect clumps at high redshift;
- The effects of the adopted observing configuration (asterism, z, photometric band) on the detectability of the clumps;
- The ability of MICADO+MORFEO to resolve multiple parsec scale clumps confined within a ≈ 100 parsec size region.

Chapter 2

ELT: design and instruments

2.1 European Extremely Large Telescope

The European Southern Observatory (ESO) is currently building what will be the biggest telescope ever built, the Extremely Large Telescope (ELT). This ground-based telescope will have a 39-meter diameter primary mirror, allowing it to collect 15 times more light than the actual biggest 10m class telescopes. It will operate in the near-IR and will allow us to get new insights on a variety of astrophysical themes, from the study of objects in our Solar System to the characterization of the most distant sources in the universe.

ELT is actually under construction in Cile, more precisely on the flattened mountainop of Cerro Armazones in the Antofagasta region, at an altitude of 3064m over the sea level. This unique location will ensure optimal atmospheric conditions to maximaze the performances of the telescope. The peculiar climatic and terrestrial configurations on this site produce one of the lowest seeing level on Earth, that, together with the power of adaptive optics will provide, near diffraction limted imaging.

Thanks to the ELT's very large diameter it will be not only possible to gather more light and observe fainter objects, but also to acquire images at an unprecedented resolution. In fact, the resolution (or sharpness) of an image produced by an optical system, i.e. the ability to spatially resolve objects separated by a certain angular distance, can be approximated as:

$$\theta = \frac{\lambda}{D} \tag{2.1}$$

when λ is the wavelenght of observation and D is the pupil aperture, the primary mirror diameter in the case of telescopes. For instance, adopting

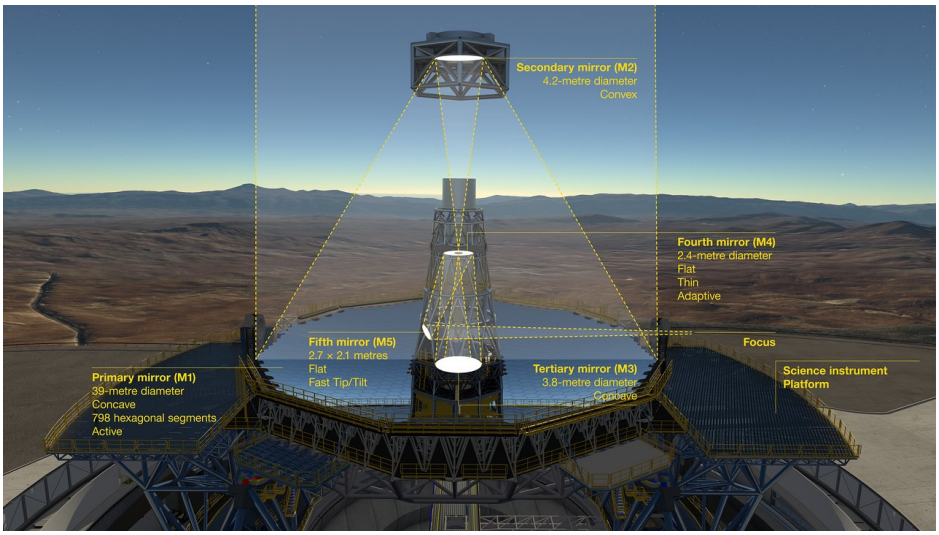

Figure 2.1: View of the mirrors that will compose the main body of the ELT. Post focal instruments like MORFEO and MICADO (sections 3.3 and 2.3) will be placed after the mirror M5. Credit:ESO

the central λ of the I, J, H and K filters that will be implemented in the ELT/MICADO camera, see section 2.3.

	800nm	1200nm	1600nm	2200nm
θ (arcsec)	0.004	0.006	0.008	0.012

As a result, images are 17 times sharper than HST images and nearly 6 times sharper than JWST. HST has a $2.4m$ primary mirror and a filter wheel containing several filters, for comparison the IR medium wide filters F098M, F127M, F139M, F153M filters producing a resolution limits which are 20, 17, 14 and 11 times bigger than ELT's counterparts showed in the table. The James Webb Space Telescope (JWST) primary mirror diameter is 6.5m, it does not suffer from atmospheric turbolence and seeing so its resolution is linked only to its dimension, to compare the resolution limit with the ELT ones one can use the central wavelenght of F090W, F115W, F162M, F212N obtaining a ratio between the resolution power of ELT and JWST of 6.7, 5.8, 6.1, 5.8 respectively. This numbers are obtained assuming that the adaptive optics correction provides diffractio limited images.

To account for the turbulence introduced by the atmosphere, the ELT is equipped with adaptive optics to obtain images near the diffraction limits.

2.2 ELT optical path

The main body of the ELT is composed by 5 mirrors, in an anastigmat configuration of 3 convex mirrors. Each mirror has a different role in the optical path and together feed the scientific instruments described in section 2.3. Here there is a brief description of the main properties of each mirror, listed following the optical path from the telescope aperture to the focal point:

- Primary Mirror M1: with a diameter of 39m it will be the biggest mirror ever built. It will be composed by 931 exagonal segments (798 fixed on the telescope and 133 spare), aligned and placed to form a surface with a convex curvature radius of $\approx 68.7m$. Each segment weights $\approx 250kg$ and must be kept aligned with the others with an accuracy down to nanometer size to ensure optimal performances, the whole structure will move during observations due to thermal and mechanical actions. To maintain the segments aligned thousands of sensors and actuators must be placed behind the primary mirror to control each segment;

- Scondary Mirror M2: with a diameter of 4.25m it will be the biggest secondary mirror ever built. As opposed to the primary mirror, M2 will be a single-piece mirror thanks to its reduced dimension. It will have a convex radius of curvature of $\approx 8.8m$ and a central hole of 80cm, it will hang 60m above the primary mirror and redirect the light to M3;

- Tertiary Mirror M3: the presence of this third curved element makes ELT fall in the category of three-mirror anastigmat telescopes. As the name suggests the astigmatism effect can be reduced thanks to the optical configuration (like come can be corrected using two-mirrors designs). M3 will have a dameter of $\approx 4m$, very similar to M2 but the main difference is that it will be concave, instead of convex as M1 and M2, with a radius of curvature of $\approx 21m$. Both M2 and M3 weight around $250kg$ considering the mirror and the holding structure;

- Mirror M4: In ELT design M4 is the first part of the intrinsic adaptive optics, M4 is the mirror dedicated to high-order corrections, hence a deformable mirror. With a diameter of $\approx 2.4m$ divided in 6 sections of 60° it will be the biggest deformable mirror ever built. To correct for atmospherical turbulence it will use more than 5000 actuators to re-shape its surface up to 1000 times per second;

- Mirror M5: It will be a flat mirror used to correct for the Tip&Tilt effects introduced by the Earth's atmosphere and mechanical motion of the hole system, it will also serve as a folding mirror and will have an elliptical shape with axis $2.7m$ by $2.2m$.

A graphical rapresentation of the optical path of ELT can be seen in figure 2.1 and a more technical one is shown in figure 2.2, where also the orientation and the relative position of the five mirrors can be appreciated.

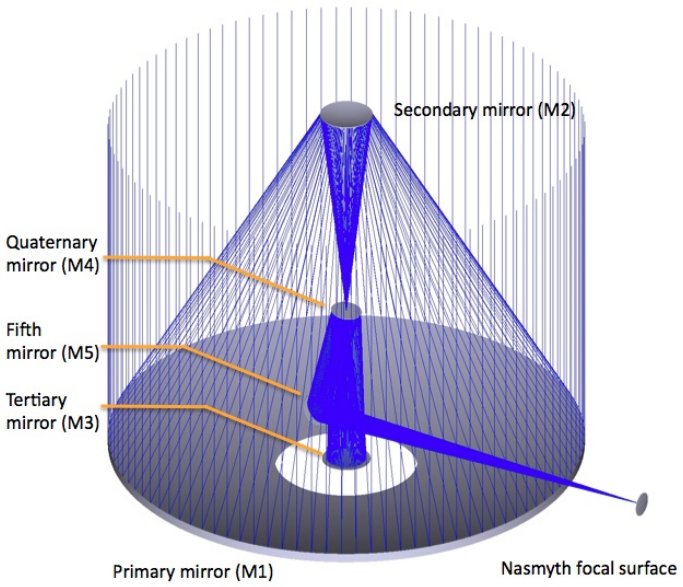

Figure 2.2: Schematic rapresentation of the ELT pre-focal optical path up to Nasmyth focal surface. Credit: ESO.

2.3 ELT instruments

In this section are briefly described the instruments that will be mounted on the ELT, both first light and later settling ones. The Adaptive Optics MORFEO module, dedicated to the MICADO imager, will be described more in detail in the next chapter at section 3.3, because its functioning and in geenral the concept of adaptive optics is of crucial interest for this work.

Near-IR imager: MICADO

MICADO (Multi-AO Imaging CAmera for Deep Observations) will be the first light wide field near-IR camera of the E-ELT. After an initial phase of operations at the ELT's first light, during which MICADO will be in "stand-alone" mode with only its own instrinsic SCAO correction available, it will

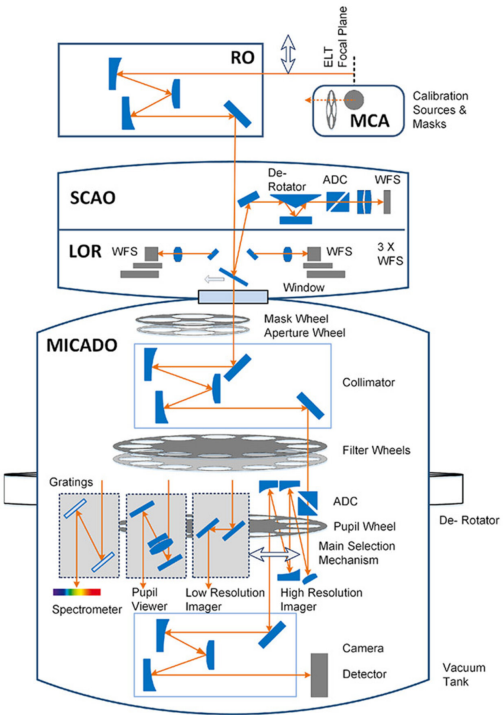

Figure 2.3: Optical design of the MICADO module. Credit: ESO

move to its final configuration where it will interfacewith MORFEO, thus having both SCAO and MCAO correcting modes. Together with MORFEO, MICADO will record nearly diffraction limited images in the 800-2200nm range. It will offer two different imaging modes: a wide field option with a field of view of 50.4"x50.4" and a pixel scale of 4mas, plus a zoom option with 18.9"x18.9" field of view and a pixel scale of 1.5mas allowing for high-precision astrometry. The instrument is equipped with a large filter wheel able to host up to 30 Near-IR narrow band filters and IJHK broad band filters. To avoid thermal interaction between the imager and its surroundings, it is held inside a cryostat at 80K. In that way, it is possible to isolate the infrared radiation coming from the astronomical target from the thermal infrared emission of the telescope and the dome themselves. Besides imaging, MICADO will provide also coronography and slit spectroscopy with a resolution between 10.000 and 20.000 using a 16mas slit.

The detector is composed of a matrix of 9 CCDs, each with 4096x4096 pixels, that will sense both the wide field and the zoom mode. MICADO will provide imaging with sensitivity similar to that of JWST, but the resulting images will have six times higher accuracy due to the primary mirror diameter.

METIS

METIS (Mid-infrared ELT Imager and Spectrograph) is a spectrograph and high-contrast imager and will be part of the first generation of instrument at the E-ELT. The use cases of that instrument span from Solar System observations thanks to the coronography mode for high contrast imaging, to the study of the central region of the Milky Way up to AGNs. METIS will have two imaging functionalities, one in the L/M band and the other in the N band, in additio to that the instrument will also perform spectroscopy observation with differente resolutions and different modes. METIS will be able to perform low, medium and high resolution spectroscopy, respectively with 400, 1400 and 100000 resolution. Spectroscopy will be made in the same optical bands as imaging, so in N and L/M bands. To achieve diffraction limited performances, METIS will use a single-conjugate adaptive-optics system, the aberration will be measured directly inside METIS and the information will be used to control the adaptive mirror of the E-ELT itself, M4 and M5, so that METIS will not require a dedicated Adaptive optics module like MICADO.

HARMONI

HARMONI (High Angular Resolution Monolithic Optical and Near-infrared Integral field spectrograph) will be one of the first generation ELT instruments. The main feature of this instrument will be its 3D spectrograph that will operate in the near-IR using an integral field unit combined with an image slicer to divide the observed field of view in many spatial pixels (spaxels), the signal of each spaxel will be fed into a spectrograph generating a spectra for each one. HARMONI will allow different plate scales, from 4 to 60 mas resulting in different fields of view. The instrument will work with two different adaptive optics systems: a single conjugate adaptive optics to obtain the best possible correction when observing smaller regions of the sky, and a laser tomography adaptive optics to correct for atmospheric effectswith an higher sky coverage thanks to the combination of natural guide stars and laser guide stars. HARMONI will operate in the Near-IR and Visible bands.

ANDES

ANDES (ArmazoNes high Dispersion Echelle Spectrograph), formerly known as HIRES, is a second generation instrument for the E-ELT and it is a powerful spectrograph that covers the optical and NIR spectral ranges simul-

taneously. It is composed by three different echelle spectrographs covering different bands providing a simultaneous coverage of 0.4-1.8 μm at resolution 100.000, over the bands UBV for the first echelle, RIZ for the second echelle and YJH for the third echelle. Moreover ANDES will be equipped with an Integral Field Unit (described in section 2.3) fed by a single conjugate adaptive optics module. Thanks to the wide spectral range and the very high resolution ANDES could be used to investigate many scientific cases, from the measure of the expansion of the Universe to the search for signs of life in exoplanets.

MOSAIC

It is a Multi Object Spectrograph that will operate both in VIS and NIR spectral ranges. MOSAIC will use the largest possible field ofview offered by ELT, $40x40$ $arcmin$, allowing to study several objects during the same observation. The instrument will serve also as a follow-up observer of space telescopes discoveries, the bigger primary mirror diameter will allow to observe more in deatil the same targets; helping to study the matter distrubution in ancient galaxies in order to improve our understanging of the galaxy formation and evolution mechanisms. The instrument will have three modes, two of which will be used to target unresolved sources in the visible and infrared respectively, with resolutio that depends on the choosen band and goes from $R = 9000$ to $R \geq 18000$. It will feature also a third operative mode able to spatially resolve sources using IFU techniques.

Chapter 3

Adaptive Optics: The MORFEO module

Every optical system is characterized by a Point Spread Function (PSF) which describes how the light coming from a point source is imaged by the system. A perfect reconstruction of the point source is not possible due to the dispersive nature of the optical elements (such as lenses and mirrors); hence, a point source imaged by an aberration-free optical system results in a discrete image. In general, the function describing the PSF is the Fourier transform of the function describing the aperture under which the system gathers light. An infinite aperture would result in a Dirac delta PSF (i.e. a perfect point source is imaged as a perfect point source). The ideal PSF of a diffraction limited telescope is described by a first order Bessel function. The parameters associated with this Bessel function are linked to the dimension of the telescope and to the wavelength of the incoming wavefront.

The distance between the first two zeros in the PSF is called the Airy disk and sets the resolution limit of the optical system, which is roughly $1.22\frac{\lambda}{D}$. Two objects separated by less than this value in the image plane cannot be resolved and they result in the sum of the two, as can be seen in figure (3.1).

The diffraction limit, imposed by the nature of the imaging system, is the best possible way to image a target, but unfortunately other effects take place degrading the image quality:

- Manufacturing residuals and imprecisions on the optical components;
- Deformations due to gravity and thermal load;
- Effects of the wind during long time exposure observations;
- Atmospheric turbulence (i.e. Seeing);

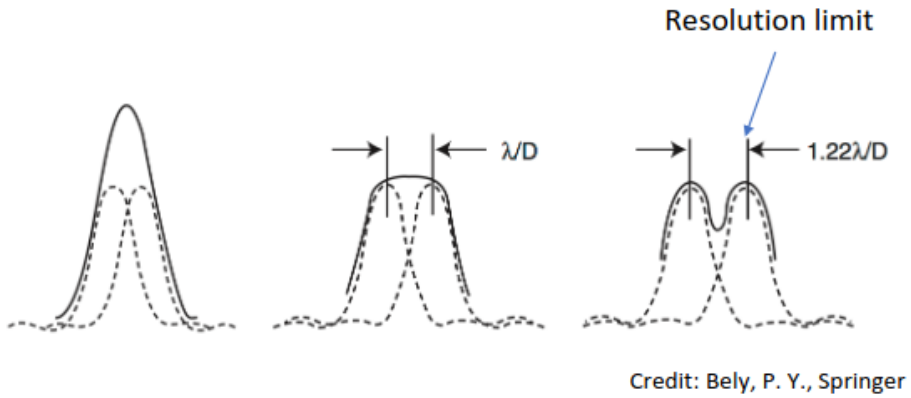

Figure 3.1: Example of how two sources, observed at a wavelength λ by a telescope of diameter D, appear in the image plane if they are located at different separations.

- Alignment errors;
- Other smaller effects.

The aim of adaptive optics is to correct for these kinds of effects to provide a close to diffraction limit image quality.

3.1 Active Optics

The first proposed solution to correct for slow image perturbations is to use active optics technique. This technique was first developed in the mid 70s on the New Technology Telescope (NTT), and it comprises an array of mechanical actuators glued to the mirror to push or pull the surface in order to compensate for mirror deformations due to gravity and thermal load.

The Active Optics system receives multiple feedbacks in open-loop to reshape the mirror from look-up tables regarding thermal, gravity and manufacturing errors.

These kinds of deformations happen slowly (or are even fixed in time, like manufacturing residuals), so it is easy to predict and tabulate their effects. By sensing the mirror at different temperatures and in different orientations it is possible to produce tables containing the expected deformations and program the actuators to counteract this deformation.

In today's instruments, the Active Optics part regulates the derotation, the deformation of the mirrors and the mutual alignment between the telescope's optics through a derotator module and a 6 axis exapod able to move the mirror (usually the secondary since it is smaller) to provide perfect alignment.

In the end, Active Optics is in charge of correcting for the effects produced by the optical elements themselves, but this accounts only for a portion of the total errors. The biggest image quality degradation is introduced by the seeing; to compensate for this, Adaptive Optics are necessary since they work for faster changes as the ones associated with the atmospheric turbulence.

3.2 Adaptive Optics

Adaptive Optics (AO) is a technique used to compensate for the aberrations of a wavefront coming from a celestial body. When emitted, the wavefront is in the form of planar waves, but when it encounters Earth's atmosphere the turbulence in it produces several different refracting indexes, which distort the wavefront. This effect is called seeing. Seeing manifests as a broadening of the PSF, and it varies in time, degrading the image quality and decreasing the resolution. AO modules are capable of sampling the atmospheric turbulence and compensating for it in order to obtain diffraction-limited images as if they were taken from space.

The AO modules are composed of three main components that work together in a close loop to provide a fast and precise correction for the real-time seeing to which the astronomical images are subjected.

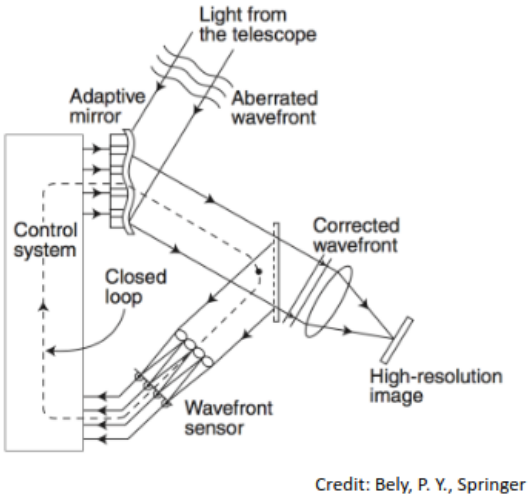

Figure 3.2: Basic scheme of a generic AO module, the three main components are the deformable mirror(adaptive mirror in the figure), the wavefront sensor and the control system often referred as Real Time Controller.

Wavefront Sensor (WFS)

A wavefront sensor (WFS) is the main measurement device inside the Adaptive Optics (AO) modules, it measures the aberration of the incoming wavefront. The aberrations are detected as intensity variations at the WFS focal plane and are then fitted using the Zernike polinomials (Noll 1976). This allows for the reconstruction of the aberrated wavefront and helps identifying which types of aberrations are present.

Aberrations are divided in high and low order depending on the spatial frequency of the distortions they produce. High-order aberrations include complex distortions like spherical aberration and coma, which affect the fine details of the image. Low-order aberrations include defocus and astigmatism, which have a more significant impact on the overall shape of the image. Different WFS are more suitable for different orders; quad-cell WFSs for example, are used to compensate for low order aberrations and to retrieve the Tip and Tilt measures and they are usually coupled with a fast mirror mounted on a exapod to counter the PSF jitter motion. For higher order aberrations the two most used WFS nowadays are the Shack-Hartmann and the pyramid ones.

Real Time Controller (RTC)

The Real Time Controller (RTC) is the brain of the AO system, it receives raw data from the WFSs and fits them using Zernike polinomials, or other mathematical functions, to determine the exact nature of the aberrations. Then it commands to the adaptive component(s) of the system the computed corrections and works in close loop together with both WFSs and deformable mirrors (Figure 3.2) to verify that the applied corrections result in an improvement of the PSF and image quality.

Since the main target of the AO system is to correct for atmospheric turbulence, the RTC needs to compute and command corrections at a very high rate, of the order of KHz, since this is the typical coherence time of the atmosphere.[1] Speed, accuracy and latency are the three key performance requirements that the RTC must satisfy.

[1]The coherence time can be computed as the time for which an astrophysical object is seen inside a bubble of atmosphere with a constant refractive index. Bigger bubbles or slower bubbles result in a bigger coherence time, and it becomes easier to compensate for the seeing effects.

Deformable Mirrors (DM)

Deformable mirrors (DM) are the key components in the AO systems and they are actively shaped as the opposite of the reconstructed wavefront computed by the RTC from the WFS data. The ability of a deformable mirror to resemble the Zernike fit of the wavefront is defined by the number of actuators attached to the mirror itself; more specifically, the N number of actuators attached to the mirror defines the highest Zernike term achievable. As the number of Zernike terms goes on, the number of actuators must also increase, but this leads to more complex and sophisticated calculations for the RTC that become unable to keep it up and so it would be useless to have countless actuators with a poor RTC. The same concept holds for the WFS: a sensor able to sample the finest wavefront error is useless if the number of actuators in the mirror is small.

A large variety of deformable mirrors are available nowadays, depending on the application. The most common are:

- Piezoelectric stacked array
  Actuators are ferroelectric plates that can change shapes when subjected to an electrical field and can push/pull the mirror surface because they elongate/shrink perpendicularly to the mirror surface.

- Bimorph
  They can locally change their curvature thanks to the same piezoelectric effect mentioned before, but this time the actuators elongate/shrink parallel to the mirror surface.

- Voice coil
  The actuators are composed of a permanent magnet glued to the mirror, coupled with a coil through which electrical current can flow to generate a force to pull/push the magnet. [2]

The interconnection between the three main components of the adaptive optics modules leads the designers to find compromises and to balance all the properties of the subsystems.

3.3 The MORFEO Instrument

The MORFEO instrument (Multiconjugate adaptive Optic Relay For ELT Observations) formerly known as MAORY, is the post focal adaptive op-

[2]Both MORFEO deformable mirrors and M4 mirror of ELT will use this technology.

tics module that will be installed as one of the first generation instruments, initially MICADO will be mounted in a standalone mode, only later the MORFEO instrument will be added to the setup to provide adaptive optics corrections. MORFEO will be mounted on the Nasmyth focal platform at ELT. It is in charge of compensating for the turbulence effect introduced by the atmosphere and other smaller disturbances of the wavefront.

The MORFEO instrument can provide two different types of correction:

- **Single Conjugate Adaptive Optics (SCAO)**:
  It is able to correct a small field of view ($\sim$10 arcsec) around a very bright object (mag $\leq$ 16.0) to be used as a reference. The correction can be very precise, but the performance degrades very quickly over the field of view. For this reason, to apply SCAO, the target must be very close to the reference object. In the ideal case, the reference star (Natural Guide Star) used to probe the wavefront is also the target object, as in the case of exoplanet imaging.

- **Multi Conjugate Adaptive Optics (MCAO)**:
  It is able to provide a decent correction over a wider field of view ($\sim$60 arcsec) with nearly constant performances. To adopt this method the presence of three NGS (mag $\leq$ 21.0) and six Laser Guide Stars (LGS) is required to produce a correction that can be valid for a larger portion of the field of view. Furthermore, the MCAO mode offers the advantage of a much larger sky coverage than the SCAO, thanks to the fainter magnitude limit allowed for the 3 NGSs. That implies that scientific targets can be selected based on astrophysical relevance rather than on feasibility criteria.

In Figure 3.3 is presented a schematic overview of the operating differencies between the two modes just described.

In MORFEO the 3 NGS are used to correct for the low order errors present in the aberrated PSF, while the 6 LGS are used to correct high order errors. LGS are used to sense the optical turbulence introduced by the atmosphere above the telescope itself. LGS are produced by shooting six sodium laser beacons in the sky, surrounding the target object for which the correction is required. Natural and Laser guide stars are used to probe different modes of the turbulence, respectively high and low order. Both the NGSs and LGSs must be positioned inside a so called "technical field" which surrounds the scientific field of the MICADO camera. The projected

position in the technical field is referred to as "asterism" from now on, and its shape is one of the major actors defining the resulting correction from the instrument, as will be intensively discussed in the next chapter.

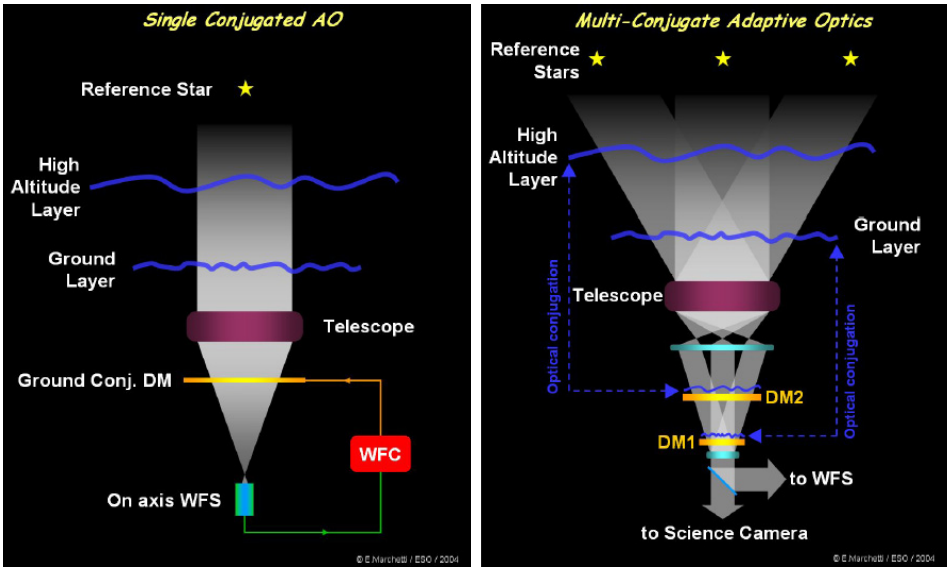

Figure 3.3: Schematic representation of the working differences between SCAO (on the left) and MCAO (on the right). Credit:ESO

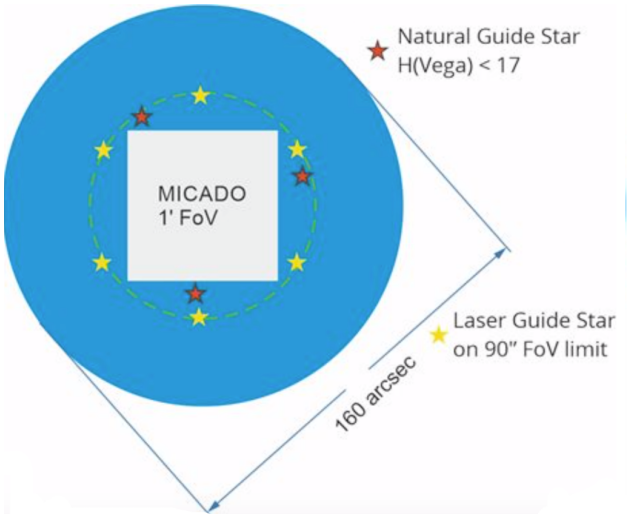

Figure 3.4: Schematic representation of MICADO "large" (≈ 50"x50") science field and of the MORFEO technical field where the NGSs and the LGSs are located.

In terms of the optical design of the MORFEO instrument, it comprises 8 reflective components: 3 aspheric concave mirrors, 2 spherical deformable mirrors, 1 dichroic mirror, and 2 fold mirrors as it is shown in figure 3.5. Where the two deformable mirrors are one convex and the other concave, respectively, in this order in the optical path. Using two deformable surfaces

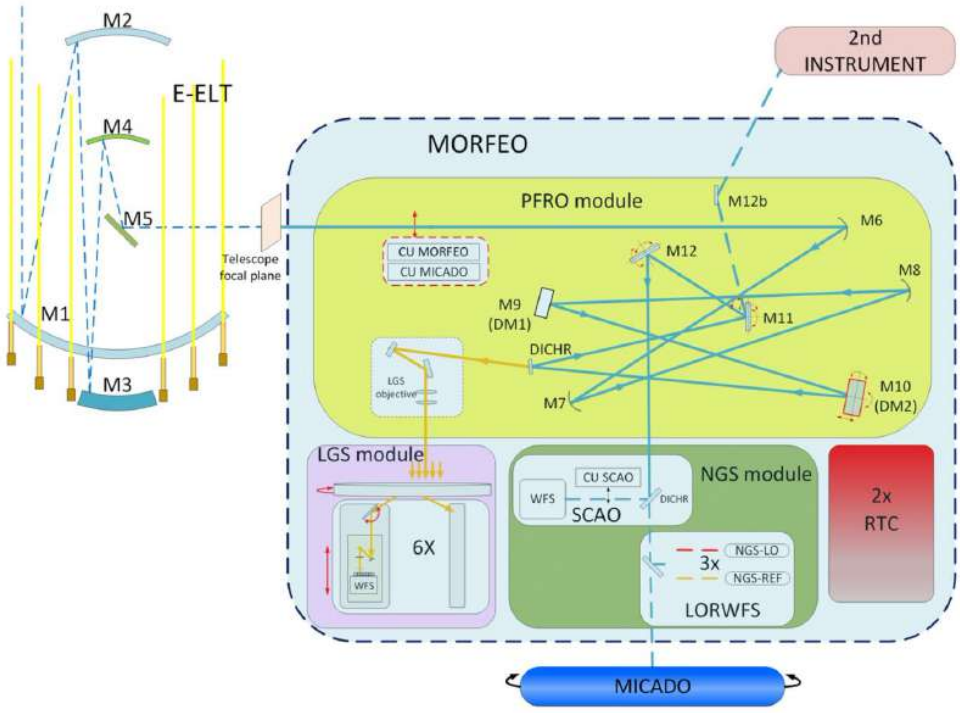

Figure 3.5: Functional overview of the optical components and optical path inside MORFEO.

instead of only one will increase the image quality and the stability of the corrections under the variations of the atmosphere. The increased correcting power resulting from this configuration makes it possible to increase the number of observable targets on the sky, i.e. the sky coverage of the instrument, with respect to other existing AO modules. The sky coverage can be defined as the portion of the sky that can be corrected with sufficient precision; in other words, it is the portion of the sky where the AO correction produces a PSF with a Strehl ratio [3] over a defined value.

[3]It is the ratio between the peak intensity of the aberrated PSF over the peak intensity of the ideal PSF related to the observing optical system

Chapter 4

Tools for simulating ELT data

In this chapter I will describe the software used to produce the simulations of ELT data and the main functionalities of these software. Simulations are produced with two separate steps: fristly, I simulated the PSF relative to the MORFEO-MICADO instrument, then I used these results inside the software ScopeSim to produce ELT-like observations. The PSF simulation is indipendent from the studied scientific case of clumps detection, but an estimate of the PSF under different configurations is necessary to study the impact of them on the observed data.

4.1 Simulating the PSFs with TIPTOP

One crucial aspect of simulating ELT data is the knowledge of the PSF. A way to compute PSFs for AO systems is to make use of Monte Carlo end-to-end (E2E) numerical simulations (like those produced with the PASSATA code, e.g. Agapito et al 2016) that model the dynamical behavior of the adaptive optics system implementing detailed atmospheric models. However, E2E simulations are higly computationally expensive, so that PSFs are typically computed for a limited number of configurations (in terms, e.g., of atmospheric conditions of guide star asterisms), which may not represent the real conditions that one encounters when performing real observations at the telescope. The way around this limitation is to produce PSFs that can be considered "good approximations" of the E2E ones but that can be computed in a much faster way, thus allowing to reproduce a larger set of possible observing configurations and explore a wider portion of the parameter space.

TIPTOP (Neichel et al 2020) is a software able to compute in a fast way

the PSF for any sort of AO system (SCAO, MCAO, etc) under different configurations. Hence TIPTOP is able to produce AO-corrected PSFs for a large set of observing configurations, thus allowing to explore all the conditions that can be met at the telescope. Compared to higly computationally expensive E2E simulations, TIPTOP is extremely fast, thanks to the fact that it uses analytic prescriptions, rather than Monte Carlo simulations, to predict the response of the AO system. In particlar, TIPTOP uses Foureir transforms to decompose the distorted light in several components and in the end combines them, makes the Fourier anti-transform, and retrieves the final PSF. More specifically, the strategy is to decouple the high-order (HO) part of the PSF, which only depends on the LGS constellation and atmospheric condition, from the Low-Order (LO) part (a.k.a. the jitter), which strongly depends on the chosen NGS asterism.

The final product of that kind of simulations is a file containing the PSFs in different regions of the field of view, with attached all the parameters used to peform the simulations and some other useful analysis results like the Full Widht at Half Maximum (FWHM), Strehl ratio and encircled energy. This kind of simulations are useful to predict the instrument performance applied to specific scientific cases under realistic observing conditions. This is exactly the aim of this work: make realistic predictions about the performance of MORFEO-MICADO for future studies of star forming clumps in star forming galaxies at different redshifts. To fullfill this goal, the system response (i.e. the transferring function), in the form of the PSF, is the main ingredient because it sets the maximum achievable contrast and the resolving power. The contrast is linked to the Strehl ratio, while the resolution is linked to the FWHM. Studying the relation of these two quantities with asterism configurations is important because it will make us able to predict the performances, achievable during an observation, before even taking it. Just by knowing the NGS configuration one could make first estimations on the achievable resolving power and contrast level.

Simulation parameters

TIPTOP is a Python library, not a standalone software, so the user has to write its own code to simulate the desired PSFs. TIPTOP is structured in such a way that it needs a configuration file containing all the specifications of the system for which the user wants to predict the PSF. This configuration file contains several sections:

- **Telescope specifications**: diameter, obscutation ratio, field of view dimension, the optical path with all the reflective and refractive components and some other parameters that help to track and take care of other errors;

- **Atmosphere**: it contains all the information about the atmospheric conditions at the observing site, such as wind and density profiles;

- **Source section**: it is dedicated to setting the position of both NGS and LGS plus it sets the positions inside the field of view where PSF estimations are made and for which wavelenght;

- **Sensor section**: here all the specifications about the high and low order sensor are defined; the pixelscale and the number of pixels to used to sample the resulting PSF are also specified. In my work, I fixed these values to 2mas/pix and 1024 pixels due to limited computing resources;

- **AO module**: here all the specifications about the deformable mirrors and the Real Time Controller are defined.

In this work I used median atmospheric conditions taken from the ESO rewiew document number: E-MAO-SS0-INA-TNO-004 (Annibali et al 2021) of the ELT site, and a set of six different NGS asterisms selected by the ESO staff listed from best to worst [1], plus the nominal specifications for the MORFEO-MICADO instrument. Notice, instead, that the LGS asterism, which has already been decided during the instrument design phase, will be kept fixed to the configuration shown in figure 4.1. What makes the difference between good and poor performing asterisms is supposed to be both the geometric location of the stars and also their magnitude. One of the aims of this work is to study which parameter is relevant to define the goodness of NGS asterism to be adopted for AO corrections. The magnitude plays a foundamental role, more luminous stars allow for a better detection of the atmosheric distorted wavefront, hence for a better sampling of the turbulence. This results in a higher accuracy in the AO-correction. While the request of bright stars around scientific target is a limitation for the number of observable objects, the MCAO concept of MORFEO coupled with the high ELT sesnsitivity will increase significantly the sky coverage with respect to previous systems (Arcidiacono et al 2024). The stars suitable to be used for

[1]From now on I will refer to the asterism using numbers, where 0 is related to the best and 5 to the worse, as intended by ESO staff and not by their real performance.

percentile	10	25	50	75	90
seeing[arcsec]	0.5	0.6	0.7	0.9	1.0
avg wind speed[m/s]	8.09	8.94	10.3	12.2	14.4
coherence time[ms]	7.7	5.8	4.2	2.9	2.05
mean height[Km]	4.5	4.4	4.5	4.5	4.6

Table 4.1: Reference atmospheric conditions at Paranal, from very good (2nd column) to very bad (6th column). In my work, I used median atm. conditions, corresponding to the 50th percentile.

AO correction must have an H magnitude between 10 an 21; exceeding that range can cause either saturation of the detector, or the situation in which the star is too faint to be properly detected and it becomes harder to study its wavefront.

In figure 4.1 the ESO selected asterisms, used to estimate the AO-corrected PSF, can be observed in their geometrical configuration with attached their relative magnitude.

As for the atmosphere, the different percentiles listed in Table 4.1 represent the probability of obtaining some specific atmospheric conditions at ELT site: for instance, only 10% of the observing nights will have a seeing around 0.5 arcseconds. Allowing observations to be taken at high percentile conditions implies that there will be more slots that match the requirements. Usually percentiles are referred as P10, P25, P50, P75 and P90, I used only P50 (median) conditions for my simulations.

4.1.1 Simulation results

A simulation was run for each NGS asterism (the LGS asterism being kept fixed) displayed in figure 4.1 and for each photometric filter, resulting into 24 simulations. For each run, 9 PSFs were produced inside the MICADO field of view to map how the performances change over the FoV. This means a total amount of 216 PSFs, all done in median atmospheric conditions. While prevoius works (e.g. Annibali et al 2021, ESO document number: E-MAO-SS0-INA-TNO-004) have explored the change in performance with atmospheric profiles, in this study the atmospheric conditions are fixed to the median profile P50 and I explored, for the first time, the impact due to the choice of different NGS asterisms.

Two important parameters that can be used to study the simulated PSFs are the FWHM and the Strehl ratio (see 3.3). A good correction is achieved, for example, when the measured FWHM is similar to the diffraction limit

value given by equation 2.1. This means that the AO module is able to compensate for almost all the atmospheric turbulence, making it possible to reach the diffraction limit. Measuring a FWHM significatively higher than the value given by 2.1 means that the configuration of the instrument fails to compensate for some aberrations. Having an high Strehl ratio is important, because it means that the AO module is able not only to compensate for the presence of aberrations, but it also converges the majority of the light from a source to the central part of the PSF. This leads to an increase in the contrast with respect to the background and thus to an easier detection of the source.

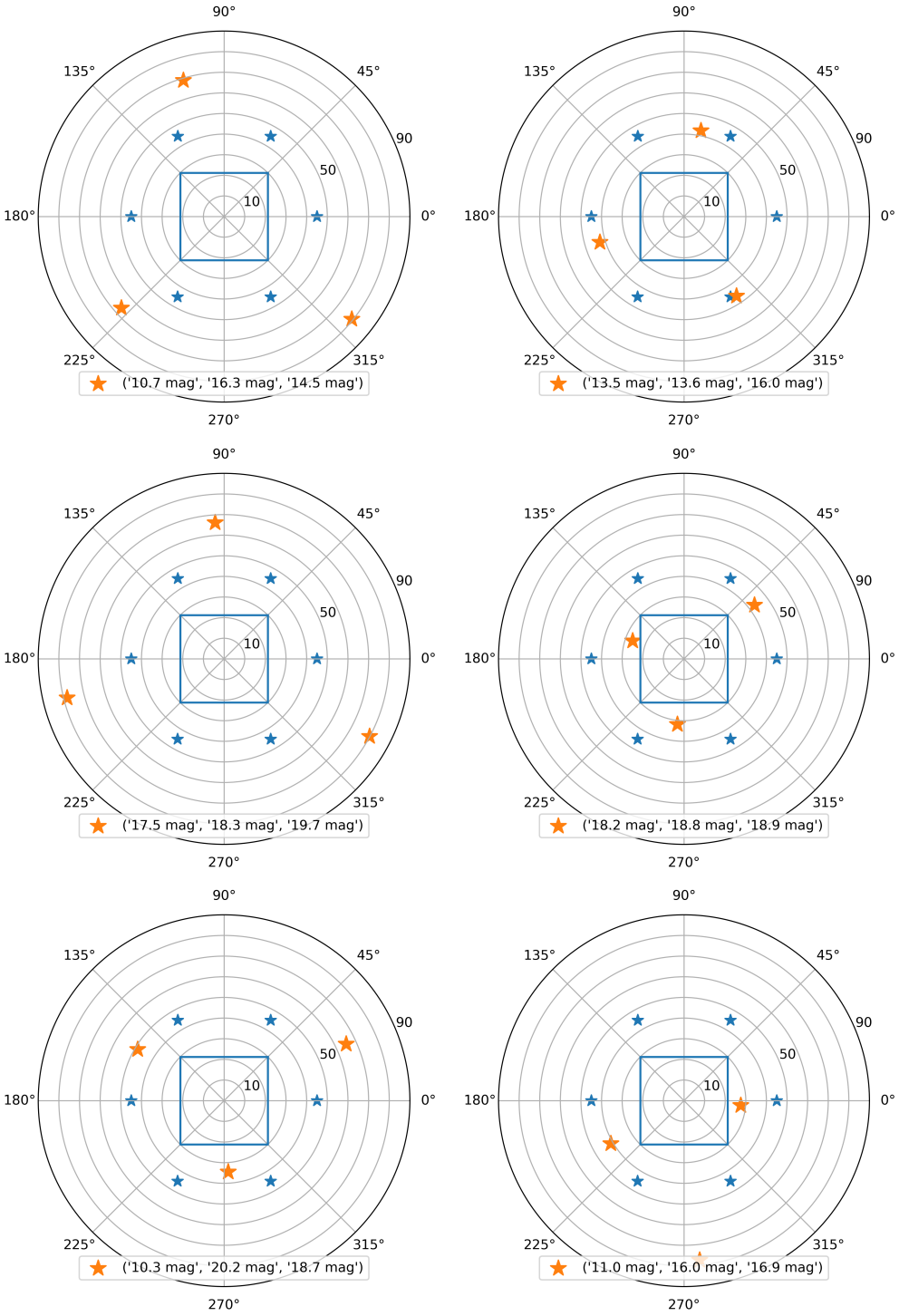

Figure 4.1: Adopted asterism configurations. Blue stars represents the fixed LGS position; orange stars represent the NGS stars position; the square in the central part of each plot represent the dimension of the scientific dedicated detector of the MICADO imager.

Full Width at Half Maximum

The results presented in figure 4.2 show a good agreement between the simulated resolution and the theoretical diffraction limit, and the accordance increase with the wavelength. This correlation is not a surprise, since in general for longer (or redder) wavelengths it is easier to compensate for atmospheric effects. The difference between shorter and longer wavelengths happens because longer waves are associated to shorter frequencies, and since frequency sets the typical timescale over which the ligth rays are scattered inside the atmosphere, shorter frequencies imply slower variations that become easier to compensate for the instruments. This behavior is responsible of what can be observed in figure 4.2, where at high wavelenghts the residuals between simulated and theoretical FWHM decrease, i.e. in the red part of the spectrum the AO-correction is better than in the blue.

Going to even redder wavelengths could seem the perfect solution to compensate for all the atmospheric effects, but the Earth atmosphere becomes opaque to the infrared radiation, so going too far in the infrared regime is useless for ground-based observatories.

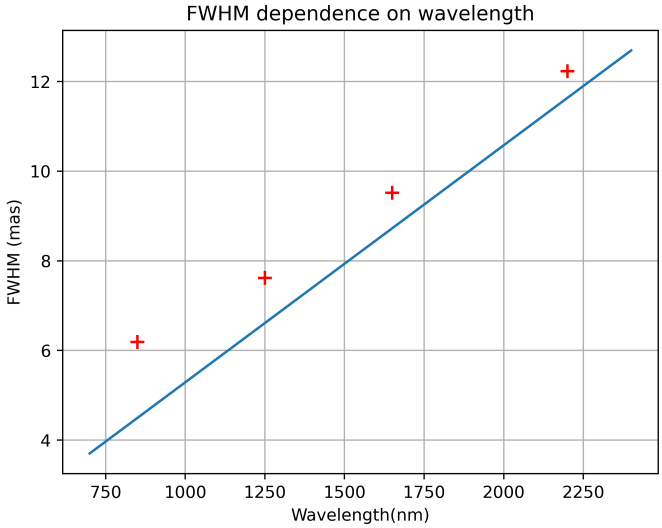

Figure 4.2: The blue line shows the expected diffraction limited locus while red crosses show the mean FWHM obtained using the different MICADO photometric filters. Also an errorbar at 2 σ is plotted, but it is lost inside the red crosses because of its small dimension.

Figure 4.3 shows the FWHM for the simulated PSFs as a function of the asterisms. It can be noticed that the main variable that drives the correcting ability of the adaptive optics system is the wavelenght, as it can be seen from the huge difference between the median FWHM lines traced in figure 4.3 for different photometric bands: these lines show that in each band the response is nearly indipendent from the asterism configuration. Nonetheless, it is still possible to observe some better and worse performing asterisms (i.e. asterism number 2 which performs worse at all wavelenghts with respect to the others).

Notice that while the value of FWHM sets the resolution limit (i.e. the minimum resolvable scale in the field of view), also the sampling of the PSF takes an important role. Following the Nyquist sampling theorem, to have a well sampled signal one should use at least three resolving units to sample the FWHM, usually five or six resolving elements would be a better choise. What is really important is that both the scientific detector and the optical system are matched, because it is useless to have a narrow PSF when the detector is unable to sample it with enough pixels and also the opposite is true, because using a over-performing detector to sample a broad PSF is a waste of resources.

To conclude, it is not only important to have an instrument, like MORFEO, able to produce images with diffraction limited PSF, but also the detector plays a key role in obtaining high quality astronomical images. This is the reason why MORFEO is coupled with the high resolution detector MICADO, which offers two different imaging modes: a zoom view with a pixel scale of $1.5 mas/px$ over 18" and a wide field view with $4 mas/px$ over 50".

Strehl ratio

As already discussed above and in section 3.3, the Strehl ratio is a measure of the light concentration in the central peak of the PSF: as this value gets closer to unity, the optical system maps the majority of the light from a point-like source in the central part of the PSF. Low values of Strehl ratio instead mean that the majority of light is dispersed inside the wings of the PSF, producing a worse constrast and a less sharp final image.

In the case of MORFEO, the Strehl ratio also affects the sky coverage (NGS stars in the technical FoV are better measured for higher Strehl ratios), and for this reason it is important to characterize this parameter and to

understand its dependencies with other quantities or observing setups. The results obtained from my simulations show a strong dependence of the Strehl ratio with wavelength, while the results are nearly constant with respect to the adopted asterisms. This means that the asterism configurations adopted in this expreiment all provide quite good Strehl ratios, as can be clearly seen in the lower panel of figure 4.3. However, lower performances could be obtained for NGS configurations less favorable than those proposed by the ESO staff, e.g. in the case where all NGSs are very faint or in the case where only 1 or 2 NGSs are available. This case shuold be explored in future works.

The low performance of the asterism number 2 is also shown in the Strehl ratio meaning that this configuration is not optimal for being used as NGS triplet to correct for atmospheric effects. This is probably due to the faintness of the three NGSs and to their relatively large distance from the centre of the MICADO field of view.

4.2 Using ScopeSim to simulate ELT observations

ScopeSim (Leschiniski et al 2020) is a flexible multipurpose instrument data simulation framework built in Python. It allows users to simulate both raw and reduced data for a wide range of telescopes and instruments. At the moment the software is mainly used to simulate raw data for developing the reduction pipelines for many different instruments, especially MICADO and METIS at the ELT.

The ScopeSim software ecosystem is composed by three differents packages: ScopeSim, ScopeSim templates and IRDB, which regulates different parts of the data simulation being completely agnostic with respect to each others. The main engine package, ScopeSim, makes no assumption about what is being observed, the characterization of the source is done by the ScopeSim templates package, while the definition of the optical train is accomplished by the IRDB package; then all the information is passed to the simulation engine to produce the output data. A scheme representing the task division is displayed in figure 4.4.

In general ScopeSim aims to simulate images of astronomical objects observed with visual and infrared instruments. It creates models of the optical train and astronomical objects and then pushes the object through the optical train. The resulting 2D image is then broadcasted to a detector chip and

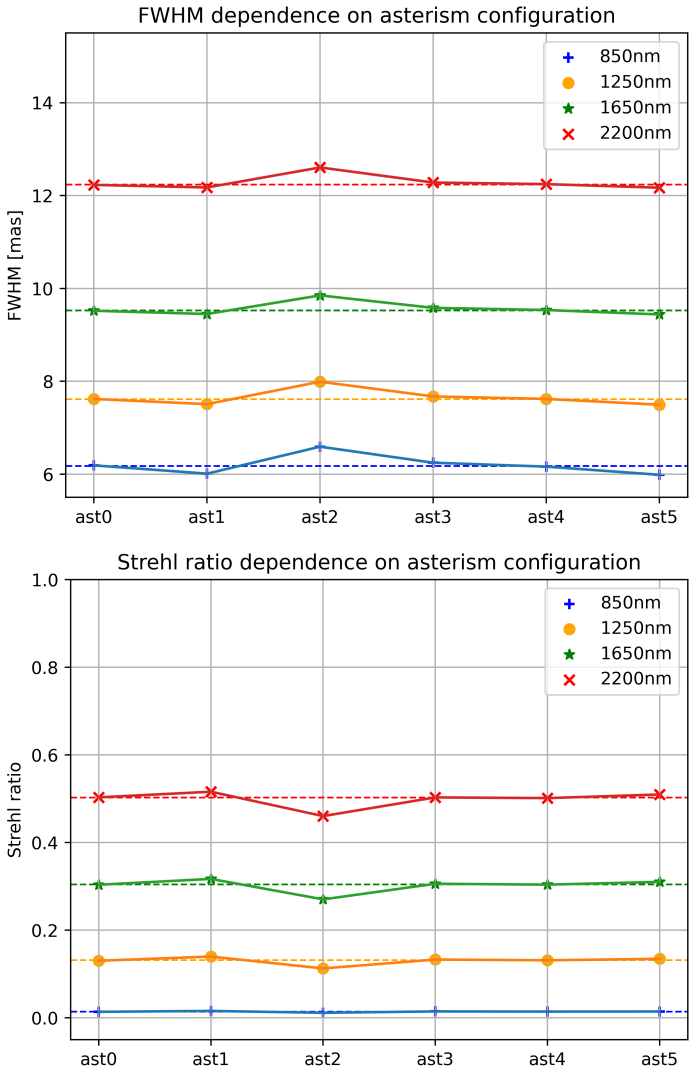

Figure 4.3: In the top and bottom panels I present the behavior of the FWHM and of the Strehl ratio, respectively, asa function of the asterisms adopted for the simulations. The median line is traced as an indicator of the overall performances; points above/below this line represent good/poor performances.

saved as a FITS file.

ScopeSim offers the possibility to the user to choose the observing target from the template packages or to insert new ones. This allows the user to produce simulations using real images as input and to obtain the result as if the same object wuold be observed under the conditions associated to the selected instruments. In this work, I considered local galaxies and local objects as reference models to map more distant ones. Thus, I use synthetic images produced with Galfit as input for all the simulations that will be described below. Since a reference spectrum is also required by ScopeSim to correctly run the simulations, a local spectrum moved to different redshifts will be

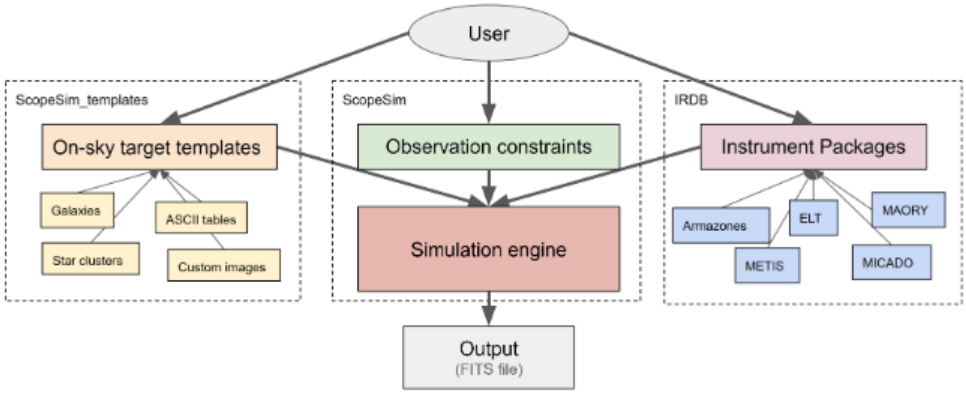

Figure 4.4: Illustration of the scopes of the three main packages in the ScopeSim envirorment. The simulation engine requires inputs from both the template and the instrument package in order to produce the desired output which is in the form of a (or many) FITS file(s). Credit: (Leschiniski et al 2020)

attached to each input image. The procedure to compute the spectrum is discussed in detail in sections 5.1 and 5.2.

The simulation workflow adopted in this experiment can be divided in three main steps:

- Definition of the source object by passing the spectro-spatial information of the target to observe. The spatial distribution comes from a FITS file generated using the Galfit package (Peng et al 2010), while the spectrum depends on the nature of the source to simulate. Both procedures are described in detail in the next section;

- Introduction of spectral, spatial, electronic and statistical aberrations to the budget of the simulation. At this point, the PSF resulting from the TIPTOP simulations is attached to the optical train so that the source, defined above, results observed under this specific PSF.

- Definition of all the instrumental/observing parameters and actual simulation by the main engine. Finally the data on the detector are extracted in the form of a FITS file, which contains the simulated image.

Instrumental and observing parameters

ScopeSim offers a unique possibility to choose from a wide set of observing instruments and telescopes, where for each of them the optical path must be specified along with specific parameters for each individual instrument. Of course in this experiment the telescope used is the ELT, and the observing

instrument is the couple MICADO-MORFEO. The speficic values and the effects included during the simulations are:

- Filters: I, J, H, K;
- Exposure time: 5 hours (divided in 100 blocks of 180 seconds);
- Telescope effective collecting area: $1.1 \cdot 10^7 cm^2$
- MORFEO temperature: 5°C;
- MICADO temperature: 5°C;
- reference room temperature: 5°C;
- Airmass: 1.1;
- Effects: dark current, shot noise, detector non-linearity, readout noise, PSF obtained from TIPTOP simulations.
- MICADO imaging mode: Wide mode, plate-scale $4 mas/px$

Chapter 5

Preparing the source data for simulations

To study the clump detectability and assess the instrument performance, it is necesary to produce source images to be used as input in the ScopeSim simulations. This chapter is about the process of image and spectrum construction followed to prepare the data to be injected into the software that will produce simulated MORFEO+MICADO data of star-forming clumps.

Since the input images for MORFEO+MICADO simulations are produced through softwares that require some assumptions on the properties of the source, I will describe in this chapter the parameters defining both the clumps and the host galaxy: size, magnitude, sufrace brightness profile and spatial position within the MICADO FoV. To study the dependence on redshift, images of the same target are reproduced at different redshifts to understand what are the capabilities of the instrument. More specifically, I adopted redshift values of 0.5, 1, 2, 4 and 6 where HST and then JWST have detected the presence of clumps in gravitationally lensed systems (Vanzella et al 2022, Messa et al 2022, Vanzella et al. 2023) and, at lower z, in non-lensed ones.

The chapter is organized as follows: first I will present an overview of the parameters used to characterize the host galaxy and the clumps; then I will discuss the approach to associate a spectrum to the galaxy and to the clumps; next, the resulting images are shown and discussed. The final MORFEO+MCADO simulations will be presented in the next chapter.

5.1 Host galaxy

Star forming regions are not observed as standalone structures in the Universe but are always located into host galaxies. Thus it is important to start the analysis by modelling the galaxy which hosts the star-forming clumps, because the most important parameter for their detectability is the contrast between the light emitted from the galaxy and the light emitted from the clumps. Assuming a surface brightness profile for the host galaxy is therefore a key step when producing syntehtic images. For the scope of this work, the required parameters to characterize a galaxy are:

- Mass ;
- Effective radius ;
- Total magnitude ;
- Surface brightness profile.

These parameters must be give in input to the Galfit software (Peng et al 2010), along with other parameters defining the position of the galaxy in the final image.

The surface brightness profile adopted in this work is from the family of Sersic profiles (figure 5.1)

$$I(R) = I_e \cdot exp\left\{-b_n\left[\left(\frac{R}{R_e}\right)^{1/n} - 1\right]\right\} \tag{5.1}$$

where I_e is the intensity at the effective radius R_e that encloses half of the total galaxy light and b_n is a dimensionless parameter whose value is determined by the definition of R_e; in particular the value of b_n can be computed using the linear fit approximation (Caon et al. 1993; see also Ciotti 1991):

$$b_n = 2n - 0.324 \tag{5.2}$$

where in the case of $n = 1$ it results $b_{n=1} = 2 \cdot 1 - 0.324 = 1.676$. A Sersic profile with index 1 will be the adopted brightness profile to characterize the host galaxy at each redshift.

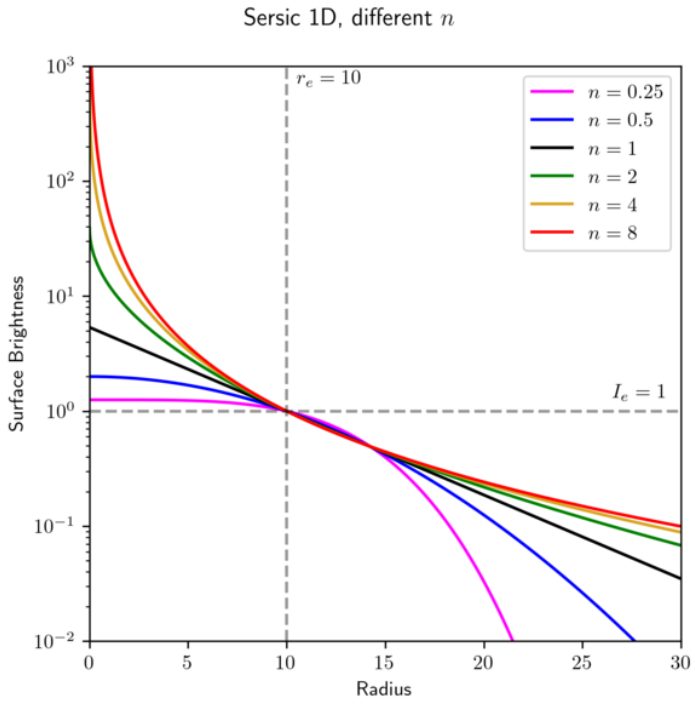

Figure 5.1: Unidimensional Sersic profiles for different indexes n. Index n=1 and n=0.5 are the two used in this work. Credits: Wikipedia.org

To start with, I assumed for the host galaxy a mass of $5 \cdot 10^{10} M_{\odot}$ and an effective radius of 4.5kpc, which are typical values for a moderate-mass local spiral galaxy, e.g. NGC 6744, and are in agreement with mass-size scaling relations derived for nearby star-forming galaxies (e.g. Shen et al 2003: van der Wel et al 2014).

Inside Galfit, the value of effective radius must be given in units of pixels (Peng et al. 2010). Therefore, one has first to compute the apparent angular radius of the galaxy as a function of redshift, and then to convert this value into number of pixels adopting a specific pixel size. To convert physical size into angular ones, I adopted equations 5.3 to 5.5

$$\theta = \frac{D}{D_a} \tag{5.3}$$

$$\theta(z) = \frac{D \cdot (1+z)^2}{D_L} \tag{5.4}$$

$$D_L(z) = D_a(z)(1+z)^2 \tag{5.5}$$

In equation 5.3, θ is the angle in radians subtended by the source on sky, D_a is the angular distance and D is the physical dimension of the astrophysi-

z	0.5	1	2	4	6
Radius [kpc]	4.5	4.5	4.5	4.5	4.5
θ[mas]	0.729	0.554	0.528	0.634	0.771
pixels	182	138	132	159	193

Table 5.1: Table providing the number of pixels and the angular size corresponding to the same physical size $R_e = 4.5kpc$ adopted for the host galaxy at different redshifts of 0.5, 1, 2, 4, 6.

cal object. This equation is valid for local sources. However, when observing sources at high redshift, the expansion of the universe must be taken into account: objects of the same physical dimension will appear smaller with increasing redshift up to z=2, but then their apparent size will start increasing as illustrated in figure 5.2. Equation 5.4 provides the behavior of the angular size theta as a function of z, while the luminosity distance D_L is related to the angular distance D_a through equation 5.5.

To compute the galaxy apparent effective radius at various z, I assumed a physical R_e of 4.5kpc, and applied equation 5.4. The derived effective radii are reported in table 5.1.

Finally, these values were divided by the MICADO plate scale of $4mas/px$ to infer the pixel number to be used inside Galfit. The results obtained by this procedure are shown in table 5.1.

As for the magnitude of the host galaxy, I adopted from NED the values obtained for the local spiral NGC 6744, at a distance of $\approx 7Mpc$: this galaxy has an AB magnitude of 7.41 at 8140 Å that, once correctd for the distance modulus of

$$\mu = m - M = 5log_{10}(Distance) - 5 = 29.22 \tag{5.6}$$

provides an absolute magnitude at 8140 Å of $M_{8140} = -21.81$.

To translate this absolute magnitude to observed magnitudes at different redshifts, we need to recall that the apparent magnitude of an astrophysical object depends on how far it is from the observer, because the emitted luminosity is an intrinsic property and the received flux changes depending on the solid angle over which the light is emitted and received. Considering also the Universe expansion, the relation linking intrinsic luminosity to received flux for unit area is

$$F = \frac{L}{4\pi(a_0 r)^2(1+z)^2} \tag{5.7}$$

where we can see that the intrinsic luminosity is divided by a factor $4\pi(a_0 \cdot r)^2$, which represents the fact that photons are "spread out" over a sphere with that area, where a_0 is the cosmological scale factor for the current Universe. The apparent flux is also diminished by a factor $(1+z)^2$ because the redshift acts by decreasing the energy of each photon as well as the rate of arriving photons. Appliyng the definition of luminosity distance $D_L = a_0 r(1+z)$, it is possible to re-write equation 5.7 obtaining

$$F = \frac{L}{4\pi D_L^2} \tag{5.8}$$

Recalling the relation between cosmological scale factor a, its present value a_0 and the redshift z

$$\frac{a_0}{a} = 1 + z \tag{5.9}$$

it is possible to find out that the flux observed at a specific emitted wavelenght λ_{em}, in reality comes from $\lambda_{em} = \lambda_{obs}(a/a_0)$. So the Universe expansion has a duoble effect: it shifts the emission at redder wavelenghts and also introduce a redshift dependent damping in the flux intensity. It is possible to move local quantities to a desired redshift using the relations:

$$\lambda_z = \lambda_0(1+z) \tag{5.10}$$

$$F_{\lambda,z} = F_{\lambda/(1+z),0}(\frac{D_{L,0}}{D_{L,z}})^2 \frac{1}{(1+z)} \tag{5.11}$$

where λ_0 is the rest-frame wavelength, λ_z is the observed one, $F_{\lambda,z}$ is the observed flux at the wavelength λ, and $F_{\lambda/(1+z),0}$ is the emitted flux at the corresponding rest-frame wavelength.

The process of computing the observed magnitudes at different redshifts starts assuming a spectrum for the host galaxy; in this work a starbrust spectrum is assumed and it is shown in black in the upper panel of figure 5.4. The spectrum was taken from the Swire library of galaxy spectra. In particular, I adopted a starbrust type because of the intense star formation expected in the targets that will be simulated. To compute the observed magnitude in all the four MICADO filters [I J H K], it is necessary to modify the starbrust spectrum according to redshift. This process implies a shift to redder wavelenghts and also a dimming in the flux intensity. Equation 5.11 shows how the wavelenght and the flux are modified as a function of redshift. First, adopting the reference absolute magnitude of $M_{8140} = -21.81$

for NGC6744, I normalized the Swire starbrust spectrum to this value at $\lambda = 8140$; then, for each redshift value, the spectrum was modified using equations 5.11 and magnitudes were computed at the wavelenghts corresponding to the centroids of the I, J, H, K MICADO filters. The resulting magnitudes are provided in table 5.2. The values obtained from this procedure are then given as input to Galfit to simulate the host galaxy at different z.

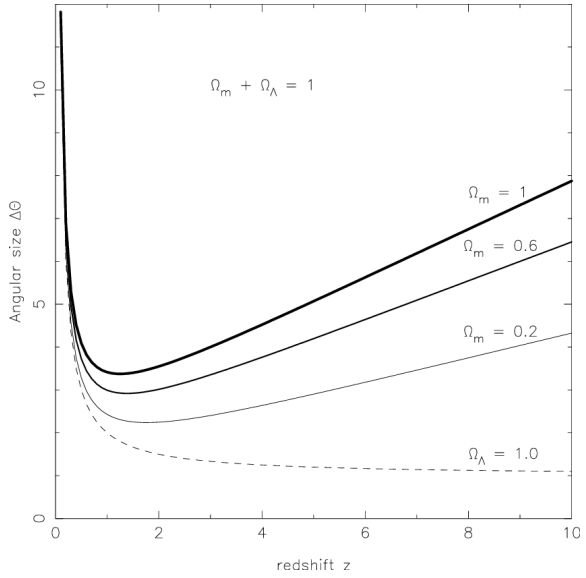

Figure 5.2: Plot representing the angular size as a function of redshift for an object of fixed physical dimension. This behavior is the motivation behind the scale change presented in table 5.1.

z	I	J	H	K
0.5	20.5	21.0	X	X
1	21.9	22.6	23.1	X
2	24.1	24.3	25.0	25.0
4	24.7	25.5	25.9	26.0
6	X	25.9	26.6	26.9

Table 5.2: Table providing the magnitude values associated to the host galaxy at diferent redshifts in all the different MICADO filters. The 'X' means that the band do not sample the adopted spectrum at that specific redshift, so we can not make magnitude estimations.

5.2 Star forming clumps

The approach used to simulate the presence of star-forming clumps inside the host galaxy is very similar to the one described in the previous section. Assumptions on the clumps' parameters are based on local observations. In particuar, they come from the population of Super Star Clusters (SSC) observed in nearby starburst dwarf galaxies, e.g. NGC 1705 at 5 Mpc distance (Annibali et al 2009); these SSC are thought to be similar to star-forming clumps in early Universe (e.g. Vanzella et al 2019). Once defined the "local" clump quantities, these will be modified according to redshift, as done in the previous section for the magnitude and the radius of the host galaxy. In each host galaxy I simulated 20 different clumps with various combinations of radius and magnitude.

This time the parameters requested by Galfit are:

- Effective radius
- Total magnitude
- Surface brightness profile
- Position of the clumps around the host galaxy

For the clumps, the radius is choosen inside a plausible range of 2-10 pc from the observed size of massive star clusters at different redshifts (Livermore et al 2015, Messa et al 2022, Annibali et al 2009). In particular, the size associated to the clumps are selected by a Python code which randomly selects values between 2 and 10 pc.

The choosen brightness profilefor the clumps is once again a Sersic profile (equation 5.1, figure 5.1) but this time I adopted an index $n = 0.5$, corresponding to a Gaussian profile.

The position of the clumps around the galaxy is of crucial importance to determine if it is possible to detect them on top of the galaxy. As figure 5.1 suggests, the surface brightness is higher in the central parts of the galaxy, making it harder to detect the clumps there. In general, it reasonable to expect that clumps are distributed following the surface brightness profile of the host galaxy, but this is an unnecessary complication for the porpouse of this work. Therefore, the position of the clumps is choosen in the same

way as for their radius: using a random number generator, to select for each clump a distance from the center of the galaxy in the range $0.1R_e - 2R_e$. To ensure even coverage over all the directions, the azimuth associated to the clump position is once again choosen randomly. In order to cancel out all the randomness associated to the results, a set of thousands images should be produced and analyzed in the same way, and then the results shuold be averaged. Although this kind of analysis is out of the purposes of this work, it is worth to point out possible future prespectives to increase the reliability and statistical significance of the results. In all the simulations, the relative position of the clumps has been kept fixed, but the distances from the center of the host galaxy and the inter-clumps distances have been modified according to the variation of the angular scale with redshift. The initial positions at z=0.5 are presented in table 5.5 together with informaton about the effective radius.

Magnitude is a crucial parameter needed to determine the contrast between the light received from the galaxy and the light received from the clump itself. High contrast imaging allows for the detection of fainter clumps.

To associate a magnitude value to the clumps at each redshift I started defining a "local" magnitude, using as reference the SSC (mass of $\approx 5{\cdot}10^5 M_\odot$) at the center of NGC1705. NGC1705 is an highly star-forming, blue compact dwarf galaxy located at $5Mpc$; it hosts various young clusters, the brightest of which may resemble star-forming clumps observed at higher redshift (Messa et al 2022, Adamo et al 2023). For this reason I used the magnitude of the SSC in NGC 1705 as a reference to simulate the clumps at different redshifts. The SSC has an apparent magnitude of 13.6 in UV at 3330Å (Calzetti et al 2015), corresponding to an absolute magnitude of $M_{UV} = -14.9$.

To determine the magnitude of the clumps at each redshift value, it is once again necessary to assume a spectrum. For simplicity, I adopted the same starburst spectrum used for the host galaxy in section 5.1. This is a reasonable assumption since, although the adopted spectrum contains also the contribution from several Gyrs old stellar population, obviously absent in the star-forming clumps, the old stellar component provides negligible contribution to the integrated flux, which is instead dominated by luminous, young stars (Zanella et al 2015, 2019 and Mestric et al 2022).

Then I normalized the Swire library spectrum to the UV flux of the SSC in NGC 1705, to obtain a local reference frame.The equations 5.10 and 5.11 were used to modify the spectrum, producing the results observed in figure

Z Filter	I	J	H	K
0.5	27.23	27.74	X	X
1	27.97	28.56	29.12	X
2	29.3	29.45	30.19	30.22
4	29.59	30.39	30.79	30.85
6	X	30.32	31.05	31.35

Table 5.3: Table providing the magnitude values associate to the the clumps at different redshifts in all the observing bands. For my simulations, I adopted a ± 1 interval around these reference values.

5.4. These are very similar to those obtained for the host galaxy because the starting spectrum is the same, the difference being only in the order of magnitude of the flux. Once moved the spectrum at different redshifts, the flux at the wavelenghts corresponding to the centroids of the MICADO filters' transmission curve was used to compute the clumps' the magnitudes at different radshifts. In table 5.3 are reported all the magnitudes obtained wih this procedure. Notice that to produce images of the clumps with Galfit, I assumed a ± 1 magnitude interval around the reference magnitudes tabulated in table 5.3. This will allow to characterize how the clumps' detectability depends also on their luminosity (see table 5.5)

The last parameter required by Galfit to produce the source images is the radius associated to each clump. Thus, I converted the adopted radius range of 2-10pc in the number of pixels at various redshifts, following the same procedure as in Section 5.1 for the effective radius of the host galaxy. The values are reported in table 5.4. We notice that even the largest adopted radius is well below the sampling capability of the MICADO detector, which can reach 1.5 mas/px when in zoom mode. This means that all the clumps appear as point like sources when observed and simulated through ScopeSim, thus they will assume the shape of the PSF. For that reason it is crucial to have well defined PSFs, producing the most collimated posible outcome, otherwise the light coming from these compact objects wuold be spread apart losing contrast and so losing the ability to detect the target.

After the definition of all the parameters needed by Galfit to produce the input images, it is possible to launch the software and produce the synthetic images that will be used later as source images in ScopeSim.

I produced with Galfit 16 images, which will be used as source data for the ScopeSim simulations, where each source must be observed using different

z	0.5	1	2	4	6
Scale[Kpc]	6.169	8.122	8.521	7.097	5.836
θ_{max} [mas]	1.6	1.23	1.17	1.40	1.71
pixel max	0.4	0.31	0.29	0.35	0.42
θ_{min}[mas]	0.32	0.25	0.23	0.28	0.34
pixel min	0.08	0.06	0.05	0.07	0.08

Table 5.4: Table providing the upper and lower limit, both in arcseconds and in pixel number, of the clumps radius at different redshift. The adopted pixel scale is 4mas/px.

PSFs depending on the adopted NGS asterism configuration and observing band.

ID	X	Y	R	Mag
1	1041	1059	0.32	26.2
2	1042	1240	0.117	26.5
3	921	1010	0.33	27
4	1149	798	0.13	26.8
5	1037	1015	0.37	26.5
6	1112	1281	0.32	26.6
7	1028	814	0.32	27.2
8	809	1152	0.18	26.9
9	1237	1094	0.24	26
10	1110	765	0.29	27.4
11	991	1068	0.38	27.3
12	1033	1012	0.12	26.8
13	1298	1259	0.22	27.1
14	801	1141	0.32	27.3
15	1021	930	0.36	27.6
16	1129	1099	0.16	26.3
17	824	980	0.11	27.1
18	874	1103	0.22	27.3
19	813	1014	0.13	27.7
20	1060	1032	0.18	26.8

Table 5.5: This table contains the fixed informations about the clumps such as position, radius and magnitude in the case of z=0.5, I band. X and Y represent the position on the deector and are in unit of pixels, while R is the clump radius in units of pixels. The radius is always smaller than the sampling limit of the MICADO detector, hence I used the same radius for all redshifts. Even adjusting the clumps radius as a function of redshift results in negligible differencies.

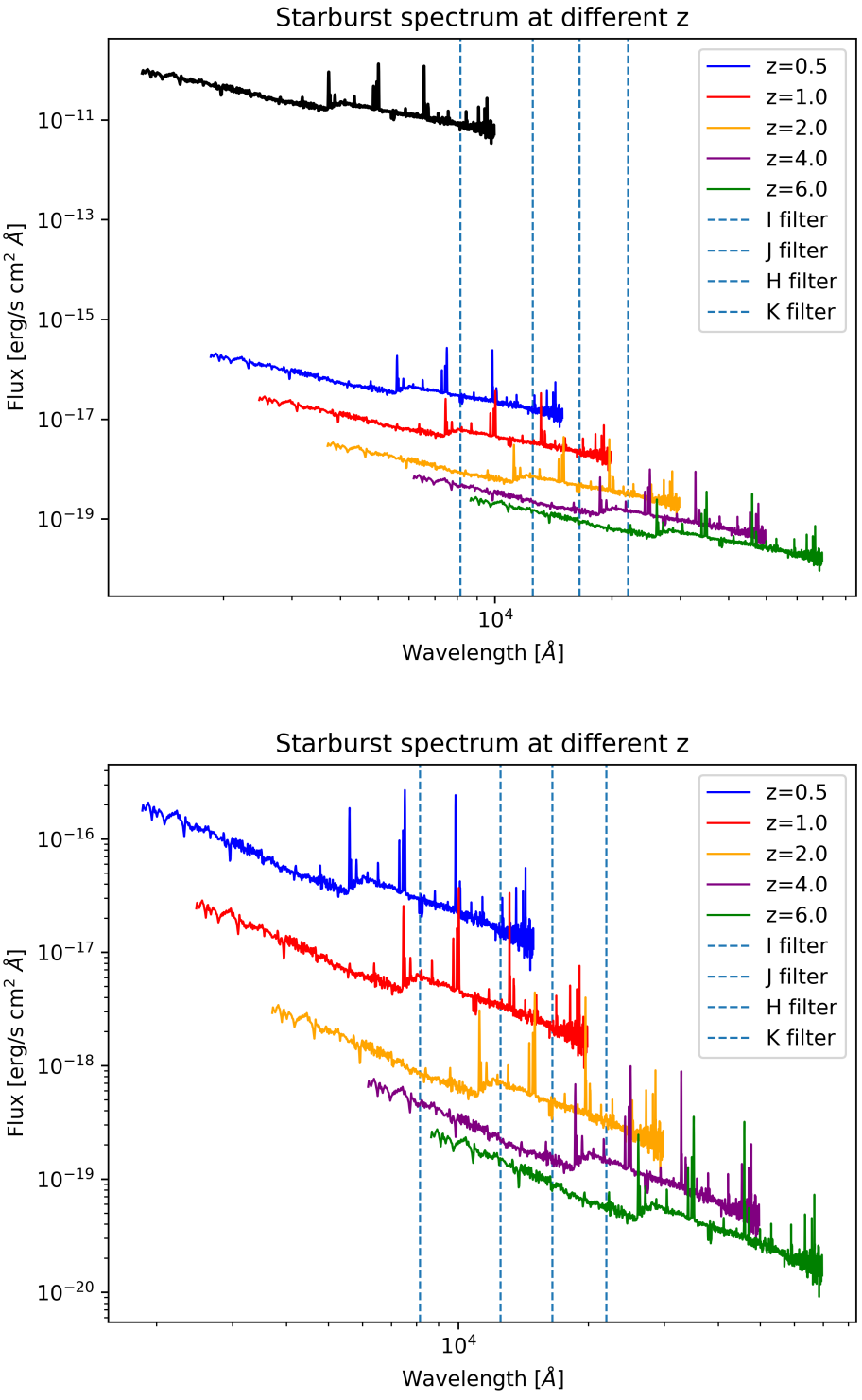

Figure 5.3: Plot showing how the host galaxy spectrum changes depending on redshift. Vertical dashed lines represent the wavelength centroid of the I, J, H, K MICADO filters. It is important to notice that not all the spectra are sampled by all the filters, therefore some combinations of band-redshift will not be simulated. *Upper panel*: Spectra are shown for all redshifts, starting from the local one (black) at z=0. *Bottom panel*: Closer look at the redshifted galaxy spectra.

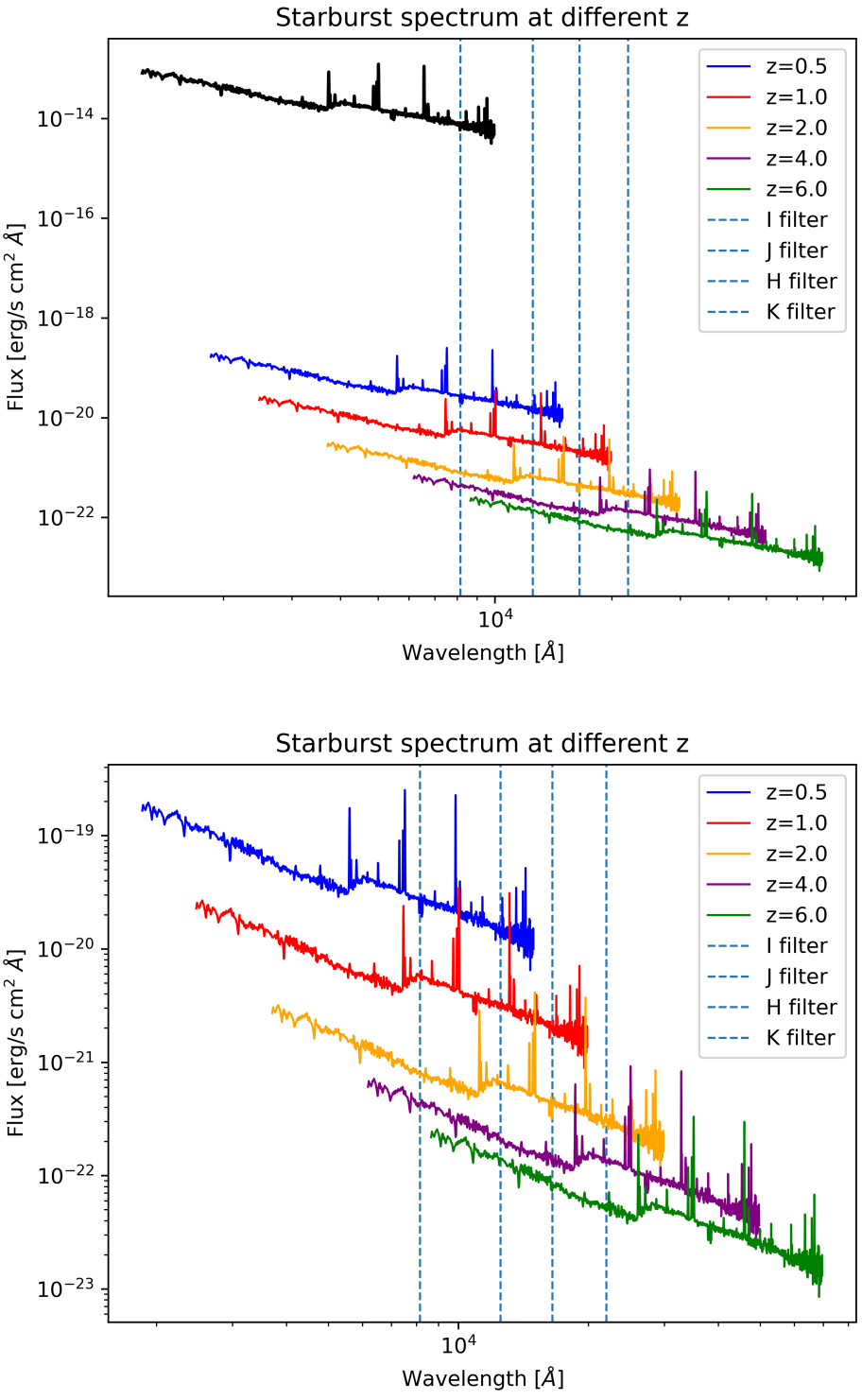

Figure 5.4: Plot showing how the clumps spectrum changes depending on redshift. Vertical dashed lines represent the wavelength centroid of the I, J, H, K MICADO filters. It is important to notice that not all the spectra are sampled by all the filters, therefore some combinations of band-redshift will not be simulated. *Upper panel*: Spectra are shown for all redshifts, starting from the local one (black) at z=0. *Bottom panel*: Closer look at the redshifted clumps spectra.

Chapter 6

ScopeSim simulations of high-z galaxies hosting star forming clumps

After the process of data preparation described in chapter 5, I simulated mock ELT observations. This work aims to study the performance of the MICADO-MORFEO instrument under different conditions: observing band, NGS asterism, redshift and clumps' parameters themselves. The 16 source images described in chapter 5, covering all possible combinations of redshifts and observing bands, are observed six times each to simulate the effect of using different NGS asterism configurations (see figure 4.1 where we display the adopted NGS asterisms used to obtain the different PSFs, see section A.1).

6.1 ScopeSim simulations of ELT data

ScopeSim requires an input image from the user in the form of a 2-D array, which describes the spatial distribution of the source on the sky plane and a spectrum in units of $photons/s/cm^2/\mathring{A}$. Since ScopeSim works using photons and counts, to simplify the process the source image has been converted from $erg/s/cm^2/Hz$ into units of $counts/s$ and the spectrum from $erg/s/cm^2/A$ to $photon/s/cm^2/Hz$.

The spectrum unit conversion has been done using the Python Astropy library (Astropy Collaboration et al 2022), which has a built-in class to perform spectral conversions for a large variety of physical units. It simply computes the energy of a photon at each frequency and then divides the

given flux by the photon energy, recovering the number of photons necessary to obtain such flux.

The images produced by Galfit are in units of $erg/s/cm^2/Hz$ and must be converted in $counts/s$ to match ScopeSim input requirements. This conversion is less trivial, because it depends on the effective collecting area of the observing telescope and on the detector quantum efficiency, but relies on the same principles as the spectrum one.

The conversion from $erg/s/cm^2/Hz$ to $count/s$, starts from the 2-D spatial distrubution image produced by Galfit. To obtain the counts per second in each pixel it is enough to multiply the $erg/s/cm^2/Hz$ value in each pixel, for the telescope collecting area and then divide for the Plank constant h. In general, the flux is defined as an energy that pass through an area in a certain time:

$$Flux = \frac{Energy}{time \cdot area} \tag{6.1}$$

Substituting known astronomic quantities and assuming to have a frequency dependent flux, the relation 6.1 becomes:

$$Flux = \frac{erg}{exptime \cdot area \cdot \nu} \tag{6.2}$$

where the exposure used in Galfit to produce images is 1s. By reversing 6.2 it is possible to retrieve the formula to convert from flux in $erg/s/cm^2/Hz$ to $photon/s$:

$$\frac{flux \cdot area}{h} = \frac{\cancel{erg}}{s \cdot \cancel{cm^2} \cdot Hz} \cdot \frac{\cancel{cm^2}}{\cancel{erg} \cdot s} = \frac{1}{s^2 \cdot s^{-1}} = \frac{photon}{s} \tag{6.3}$$

where the ELT collecting area, estimated around $11440000cm^2$, is a first order approximation and it has been computed subtracting from the primary mirror area $\pi \cdot 38.5^2$ $[m^2]$ the area of the secondary mirror producing obscuration $\pi \cdot 4.5^2$ $[m^2]$.

After the due conversions, the source images are ready to be injected into the ScopeSim simulator. In the next section, I provide a gallery of the input images that were given to Scopesim to simulate the final ELT observations.

6.2 Image input gallery

Here a gallery containing all the models used as input for ScopeSim is presented. They are in units of $photons/s$ obtained according to the procedure described in section 6.1. The input images are models, whereas the outputs

are the same models convolved with the PSF and various noise sources, as discussed in section 4.2, to produce the final ELT simulated data. On the input images, the clumps are point-like sources due to their angular size being smaller than the resolutive element of MICADO (4mas/px), which is also the scale adopted in the images.

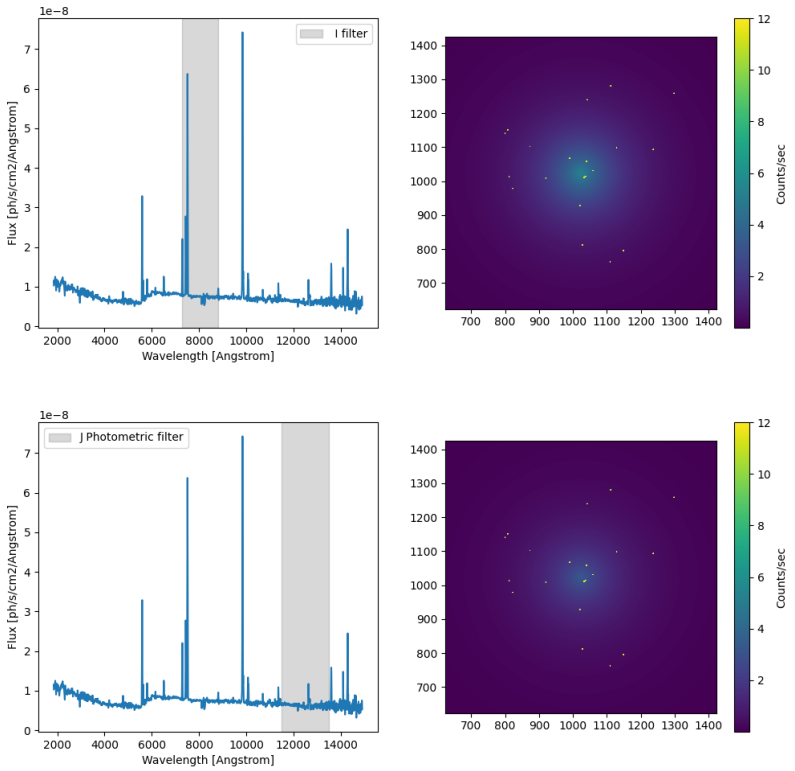

Figure 6.1: Source images and spectra used as input in ScopeSim at redshift 0.5 in the I band (*upper panel*) and J band (*bottom panel*). These are then convolved by the PSF, multiplied by the exposure time and then the noise contribution is added to produce the final data.

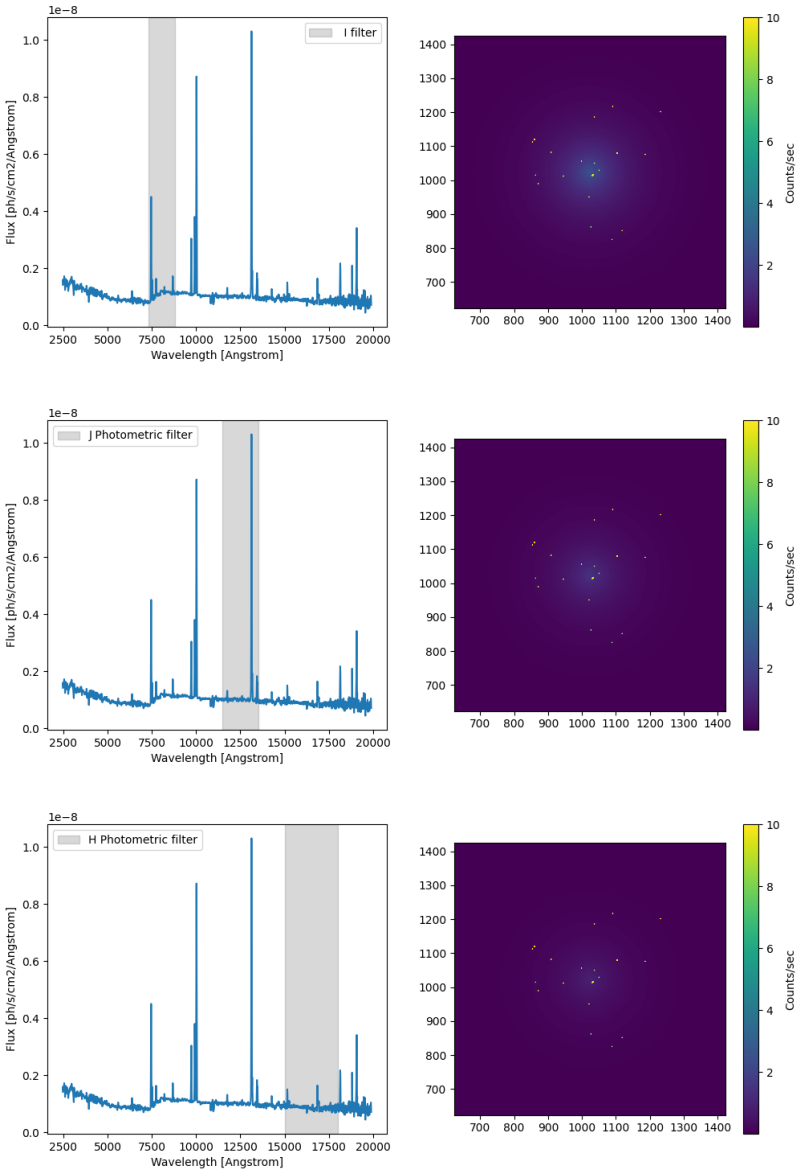

Figure 6.2: Source images and spectra used as input in ScopeSim at redshift 1 in the I band (*upper panel*), J band (*central panel*) and H band (*bottom panel*). These are then convolved by the PSF, multiplied by the exposure time and then the noise contribution is added to produce the final data.

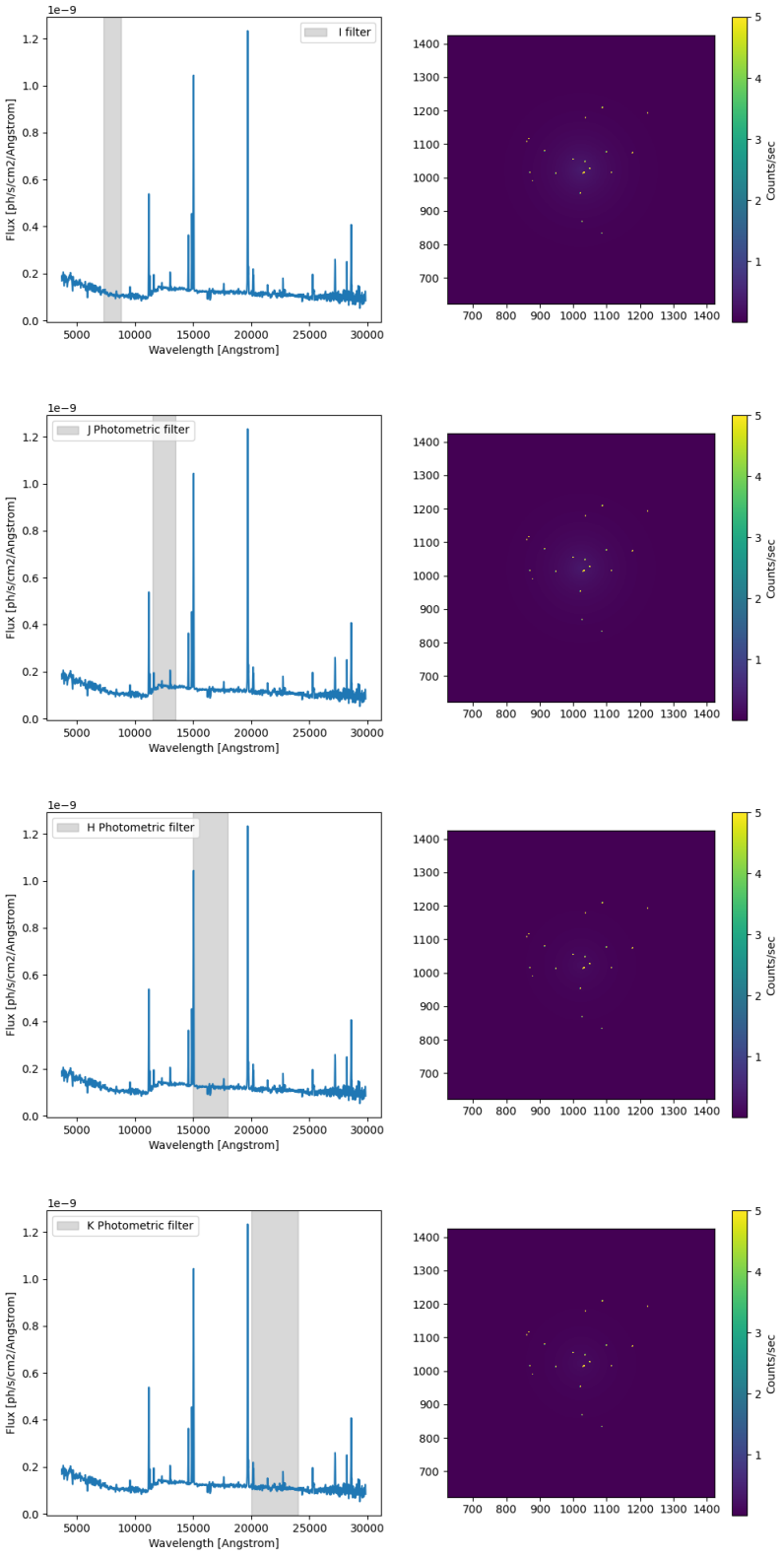

Figure 6.3: Source images and spectra used as input in ScopeSim at redshift 2 in I band (*upper panel*), J band (*second panel*), H band (*third panel*) and K band (*bottom panel*). These are then convolved by the PSF, multiplied by the exposure time and then the noise contribution is added to produce the final data.

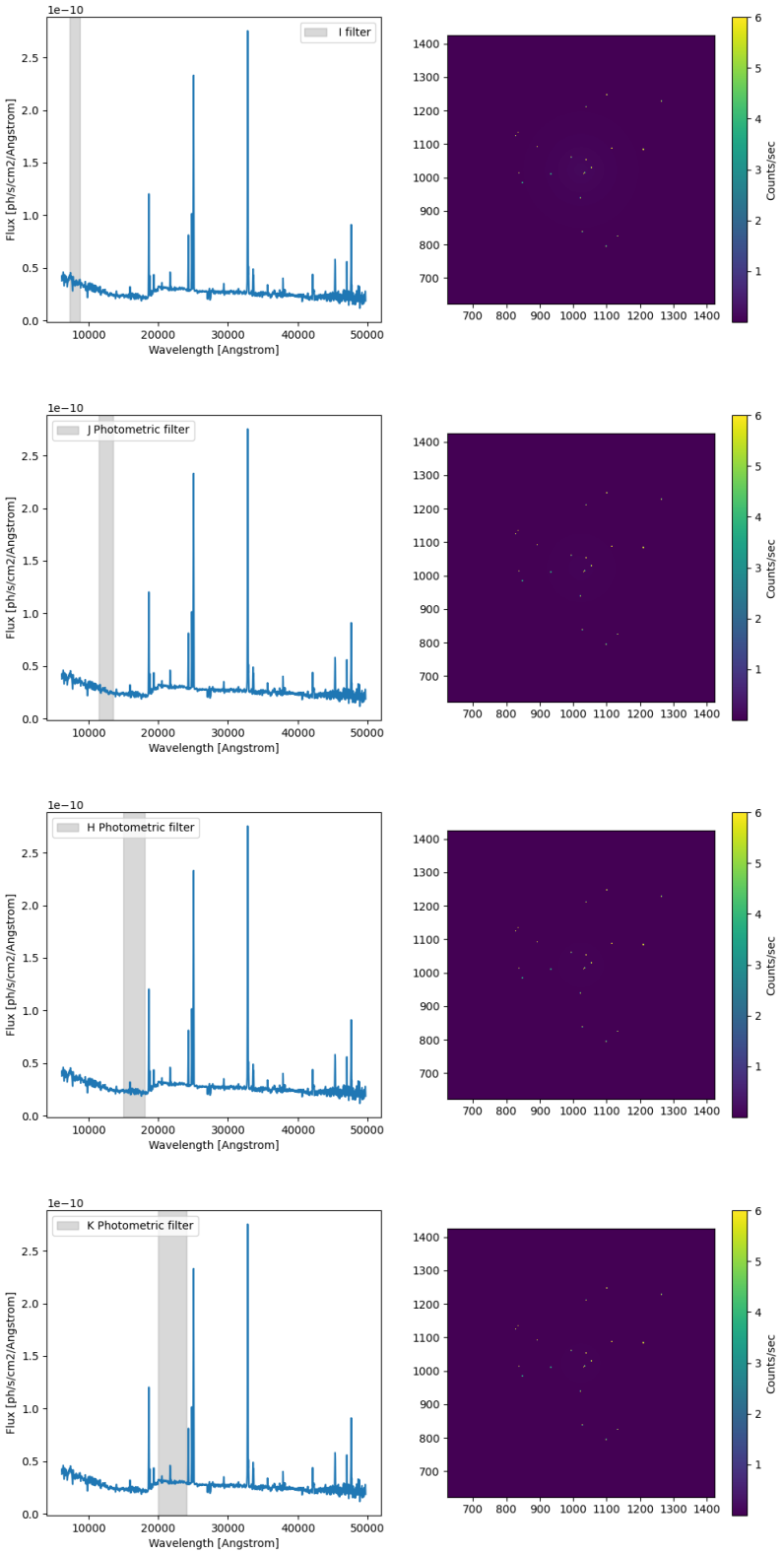

Figure 6.4: Source images and spectra used as input in ScopeSim at redshift 4 in the I band (*upper panel*), J band (*second panel*), H band (*third panel*) and K band (*bottom panel*). These are then convolved by the PSF, multiplied by the exposure time and then the noise contribution is added to produce the final data.

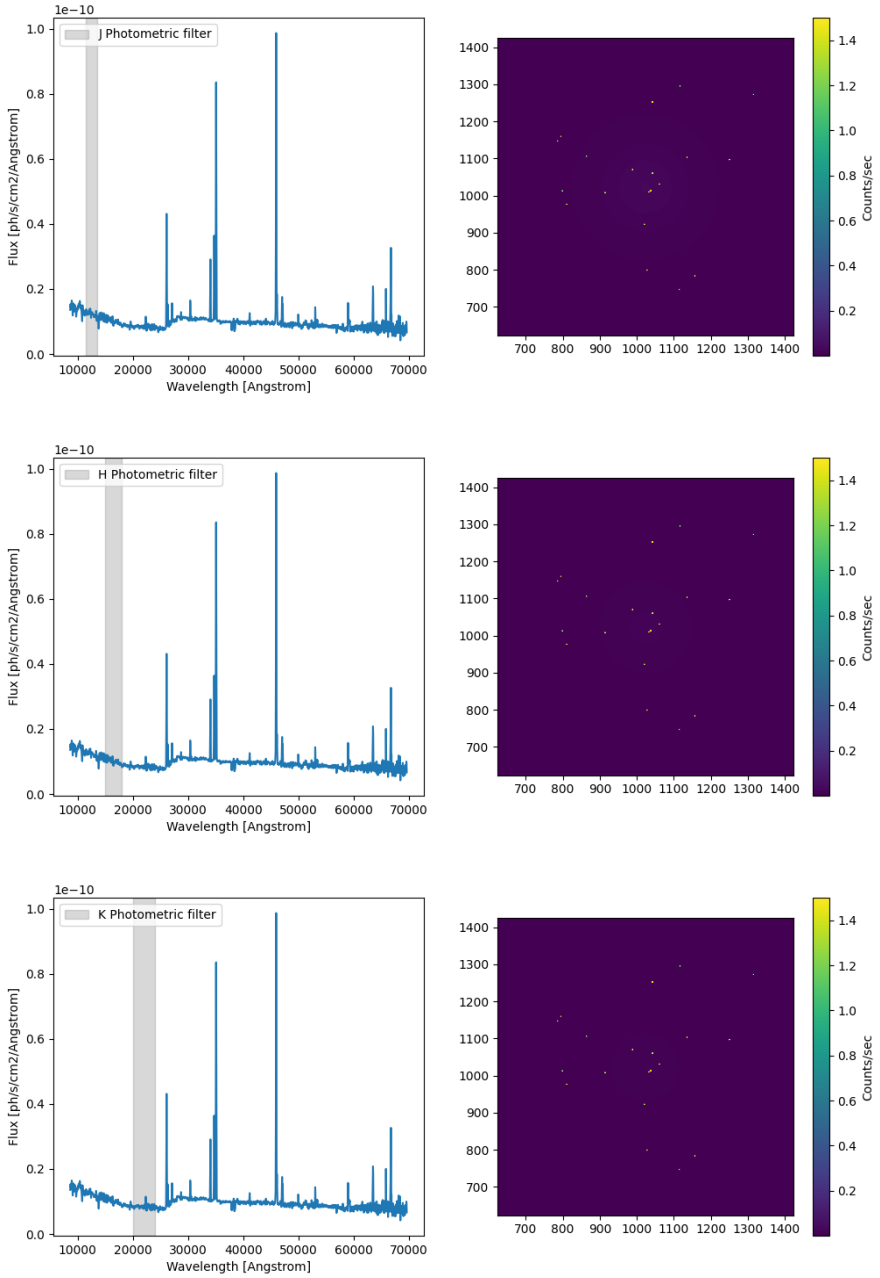

Figure 6.5: Source images and spectra used as input in ScopeSim at redshift 6 in the J band (*upper panel*), H band (*central panel*)and K band (*bottom panel*). These are then convolved by the PSF, multiplied by the exposure time and then the noise contribution is added to produce the final data.

6.3 Simulation analysis and outputs

The input data shown in section 6.2 pass through the ScopeSim simulator engine, and as result a 2-D count map is produced which resembles the read-out result of the MICADO CCD detector. The results must then be treated in the same way as of real astronomical images. Since the aim of this experiment is not to explore all the possible reduction pipelines, the images are just sky-subtracted and then the Singal-to-Noise ratio is computed to study the detectability of the single clumps. For groups of clumps separated by small projected distances (< 200 pc), also the ability of the optical system to resolve them is discussed. This aspect is of crucial importance as it has been shown (e.g., Vanzella et al. 2018) that every time the angular resolution increases (e.g., by studying lensed clumps instead of un-lensed ones or by using the JWST instead of lower-resolution imaging) the clumps appear to have smaller (tens or hundreds of pc) sizes than previously thought (hundreds pc to kpc size). For the first time, this work tries to characterize and study the ELT response to this specific scenario, aiming to help the scientific community to better understand the potential of ELT data when they will be available.

In general the Signal-to-Noise ratio (SNR) is a measure of the level the signal compared to the noise. Noise sources are variuos: in astrophysics, the noise in scietific images is both internal to the detection instrument and caused by the sky background. Mapping the two components wuold be helpful to better analyze the data and to obtain higher quality results. Not all types of noise are the same for different observations, or either during the same exposure, so the global noise contribution has to be computed for each case. A high SNR means that the signal is clear and easy to detect or interpret, while a low SNR means that the signal is corrupted or obscured by noise and it may be difficult to recover it.

In literature, different methods to estimate the signal coming from star forming clumps can be found (Forster-Schreiber et al. 2011, Elmegreen et al. 2009a). They differ in the noise estimation. Some methods fit the host galaxy and subtract its contribution from the image, in order to obtain only the clumps contribution. This could seem a sensible and straightforward method, but since it is not always obvious if what appears as a clump is indeed a separated entity or is instead part of the galaxy disk, subtracting the disk to the image can lead to the loss of key signal and produce misleading

results. On the other hand, if the noise is estimated locally in an anulus around the clump (Forster-Schreiber et al. 2011), it can become difficult in crowded fields to isolate single sources and find "empty" regions around them, thus requiring more complex analysis (e.g., like the procedure of PSF fitting used in crowded stellar fields, see Heasley 1999). In general there is not accordance between different works on how to determine pure clump signal. In addition, in this work the host galaxy has been created artificially, using a Sersic profile. Its reconstruction and subtraction would lead to have an unrealistic, perfectly subtracted image with only the clumps, thus making it useless to add the galaxy component from the beginning. For this reason I did not apply any disk subtraction previous to estimating the clump SNR. Instead, a simpler method to estimate the noise background has been used.

The procedure starts by selecting regions in the image where, by visual inspection, the astronomical signal appears absent. These regions are thus assumed to contain just the background. Several of these "empty" regions are required to perform a statistical analysis, and to retrieve the mean background and its dispersion. The background level is estimated using the pixel values measured inside the selected "empty" regions, and fitting them with a Gaussian distribution [1], as shown in figure 6.6. From the Gaussian that best fits the data, the mean value is extracted (dashed line in figure 6.6). Following this procedure, indipendent estimates of the background in different empty regions are done. Then from the mean background values computed in different regions I computed a median value to be subtracted to the whole image.

After this median background level is subtracted, the pixel values of the image are centered around 0. Now it is possible to estimate the SNR just dividing the signal in the clumps by the standard deviation computed using the mean background values from empty regions.

Usually the detection limit is fixed at $SNR = 5$; this means that, to confirm the detection of a target on the image plane, its signal must be at 5σ distance from the background level, thus to avoid the association of some random fluctuations in the noise pattern to real objects. The Rose criterion (named after Albert Rose) states that an SNR of at least 5 is needed to be able to distinguish image features with certainty. An SNR less than 5 means less than 99.98% certainty in identifying image details, according to

[1] Because noise sources are indipendent and uncorrelated, the assumed distribution for their value is a gaussian centered at the mean noise value.

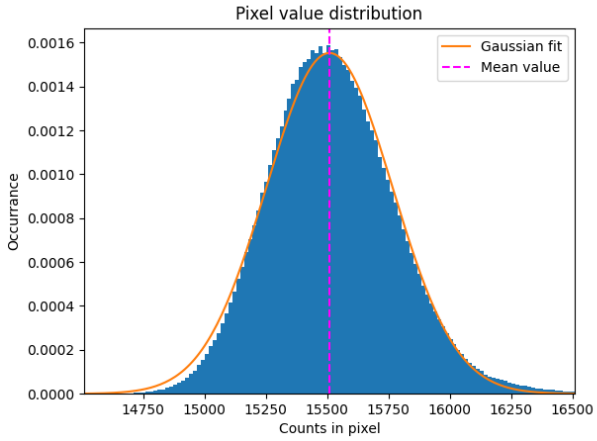

Figure 6.6: Histrogram showing the distribution of the counts in pixels in regions containing only background. The dashed line represent the estimated mean value used as background indicator for this region, this is the value that must be averaged with the ones of others empty regions and the result must be suctracred from the whole image. This image is relative to the simulation runned at z=0.5, band I, asterism 0 and is shown as a reference example.

the selected confidence interval.

In other words every sky region with intensity below 5σ around the mean background level (which is ≈ 0 for the sky subtracted image) shuold be considered as containing only noise. Sometimes the criteria for detection can be more relaxed and 3σ is choosen, which still gives 97% of probability that the signal of interest comes from a real source and it is not an observational artifact due to noise fluctuations.

All the 96 images passed through the analysis process described above. To do that, I implemented a python script which automatically computes the SNR for the clumps for all the possible combinations of z, band and NGS asterism. A clump is classified as robustly detected when its SNR is greather than 5 and as detected when SNR is greater than 3. For smaller values the clump is classified as non-detected, because there is not enough signal to be completely sure that it comes from the clump itself and not from background fluctuations.

The results are summarized in tables 6.1 and 6.2, were I report the SNR inferred for the faintest and the brightest clumps as a function of redshift, photometric band and adopted NGS asterism.

Besides detectability, also the ability of the optical system to separate close clumps has been explored. These are more qualitative results than quantitative, and are useful to define upper limits on the redshift at which

z	Filter	SNR-ast0	SNR-ast1	SNR-ast2	SNR-ast3	SNR-ast4	SNR-ast5
0.5	I	1276	1334	1242	1322	1326	1283
	J	2286	2315	2243	2300	2298	2266
1	I	1226	1250	1312	1092	1073	1037
	J	1745	2320	1930	1870	2391	2208
	H	2929	2243	2024	2899	2258	2976
2	I	200	195	189	179	367	220
	J	540	786	512	396	564	564
	H	657	1375	622	723	633	498
	K	766	397	588	716	538	384
4	I	24	30	28	28	32	41
	J	70	60	39	41	59	33
	H	52	59	31	58	83	52
	K	68	57	63	56	55	57
6	J	17	13	25	9.9	18	11
	H	21	13	20	15	23	8.8
	K	12	11	11	11	9.6	11

Table 6.1: SNR values computed for the brightest clump (ID 9) for all the combinations of redshifts, bands and NGS asterism configurations. The same results are shown in figures 6.8, 6.9 and 6.10

z	Filer	SNR-ast0	SNR-ast1	SNR-ast2	SNR-ast3	SNR-ast4	SNR-ast5
0.5	I	424	437	418	434	435	427
	J	635	641	625	637	638	629
1	I	442	441	481	387	380	374
	J	498	660	554	532	682	630
	H	754	576	522	745	581	766
2	I	60	55	56	51	104	66
	J	150	134	141	109	154	156
	H	165	345	156	180	158	125
	K	191	98	148	182	134	97
4	I	7.2	8.5	9.5	9.5	7.6	12
	J	14	14	10	11	15	7.4
	H	13	14	8.6	14	19	13
	K	17	14	16	13	15	16
6	J	5.3	3.7	7.1	3.0	4.3	2.8
	H	2.7	0.8	5.0	1.6	6.3	2.9
	K	1.3	3.3	4.5	2.8	0.2	3.7

Table 6.2: SNR values computed for the faintest clump (ID 19) for all the combinations of redshifts, bands and NGS asterism configurations. The same results are shown in figures 6.8, 6.9 and 6.10.

ELT will be able to distinguish small clumps ($R < 10pc$) close to each other ($R < 200pc$). The analysis is mainly conducted by visual inspection of the images and by analyzing the gaussians fits to the clump profiles. the spatial

profiles of the clumps.

6.4 Results

Thanks to the high sensitivity of MICADO, combined with the large collecting area of the ELT, the faintest detectable point source after 5 hours of integration has a magnitude around 30 in K band (Davies et al 2012) as can be seen in figure 6.7.

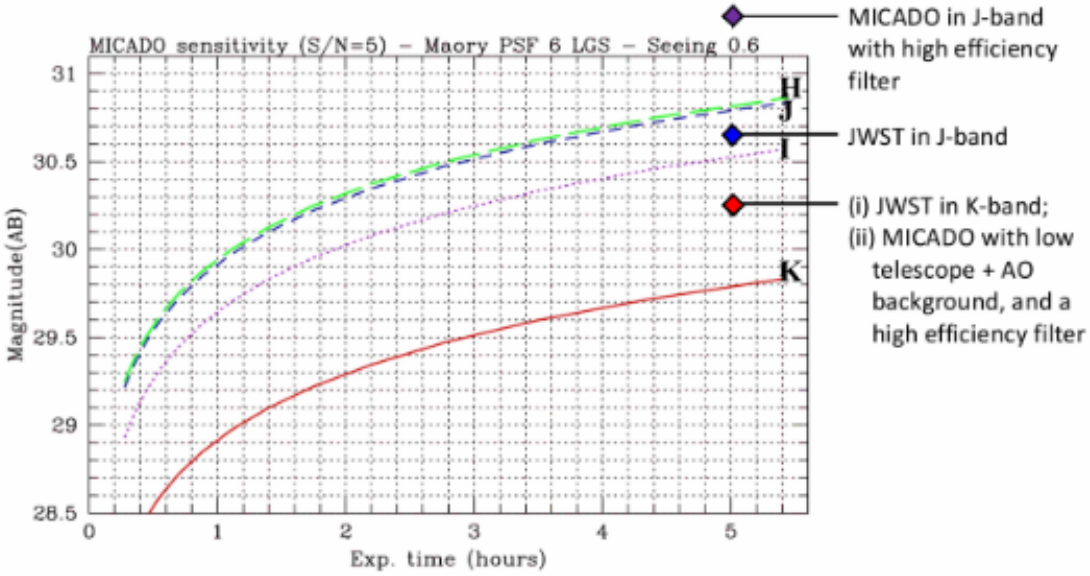

Figure 6.7: Plot showing how the magnitude limit changes when increasing the exposure time in different MICADO bands, under some fixed observing conditions. Credits: Davies et al 2012.

The behavior observed in figure 6.7 is confirmed by the analisys of my ScopeSim simulated images at high redshift, where even for the faintest clump (i.e. 30.9 magnitude in J band) at the highest redshift, the SNR is high enough to ensure the detection in some bands. After redshift 2, most clumps present a magnitude close to the estimated magnitude limit. In this experiment it is found that it is possible to detect very faint but compact objects, likely thanks to the unprecedent quality of the PSF used in this work. Notice that the PSFs discussed in chapter 3 are obtained using the most updated MORFEO parameters, and the most recent properties of the instrument, and thus must be considered reliable.

The parameters that impact on the estimation of the SNR, and so that define the clump detectability, are: redshift, observing filter and NGS asterism configration used during the observation. At different levels these three factors act on the astronomical signal. Here is reported the case of the brightest and faintest clump as reference for all the others that perform somwhere in between.

Due to the limited extension of the adopted starburst spectrum, only in the J photometric filter it is possible to perform observations at all redshifts. Thus, the J band is used as a reference to dicuss the redshift dependence, for which results are shown in figure 6.8. Here we can observe that the two lines which describe the SNR behavior for the brightest and faintest clumps steadly and rapidly decrease as redshift increases. Clumps residing above the shaded blue line should be considered as robustly detected, according to the definition discussed above. The values shown in figure 6.8 are the result of the mean over all the six NGS asterism configurations adopted. As discussed in chapter 4.1, the NGS configuration impacts the AO-correcting capability of the MICADO-MORFEO instrument, as can be seen in figure 6.9 and 6.10 looking at the difference in SNR values for the same band and same redshift, but different asterisms. The results for the brightest and the faintest clumps are shown in figure 6.9 and figure 6.10. The pattern is the same in both cases. The interesting part is that the same NGS asterism sometimes overperforms the median SNR value and other times underperforms, suggesting that the observed trend is purely due to statistical fluctuations and not to intrinsic differences in the asterism performances. This leads to the conclusion that the clump detectability is mainly driven by the brightness of the clump, while the different adopted asterisms all perform similarly well. As discussed in section 4.1, the results on the PSFs are very similar for all the NGS configurations and this leads to the results shown in figures 6.9 and 6.10.

The last parameter that changes during the simulations is the photometric band over which the target is observed. The relevance and suitability of the observing band strongly depends on the redshift and mainly on the spectrum of the target. The behavior in the I, J, H and K bands resambles what can be seen in figures 6.8, 6.9 and 6.10. While the best band to perform observations depends on the specific source, and on the properties of its redshifted spectrum, from a purely instrumental performance aspect the best band in which high-contrast observations perform the best is the K band, because there the AO-correction is better, thus sharper images can be acquired.

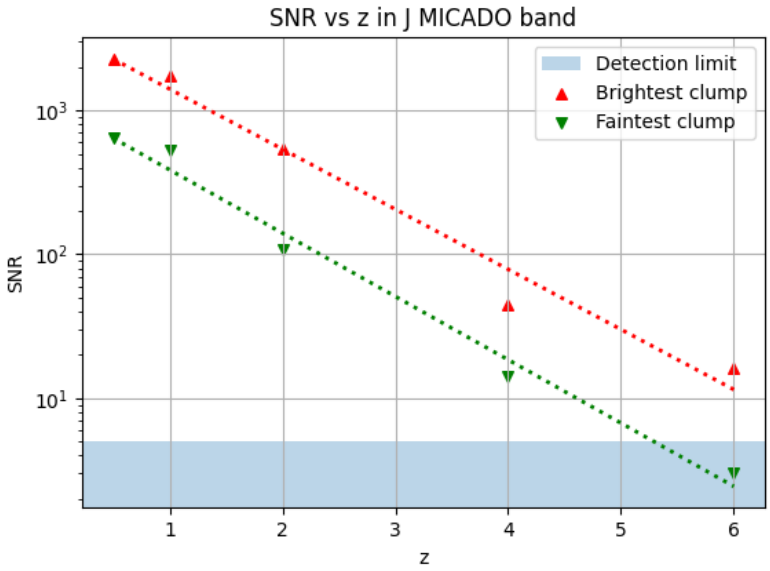

Figure 6.8: In the figure is shown the behavior of the SNR in J band as function of redshift. All the simulated clumps are located in the area between the two dotted lines. The blue area represent the detection limit set to SNR=5.

The last results from the analysis of the ScopeSim simulated data are about the ability of the optical system to resolve close clumps. In our study, two clumps of (J band) magnitude of 26.8 and 26.5, separated by a physical distance of 100 pc, result to be separated in all images up to redshift 6, as can be seen in figure 6.11, demostrating the high capability of adaptive optics at ELT in resolving the smallest structures up to very high redshifts.

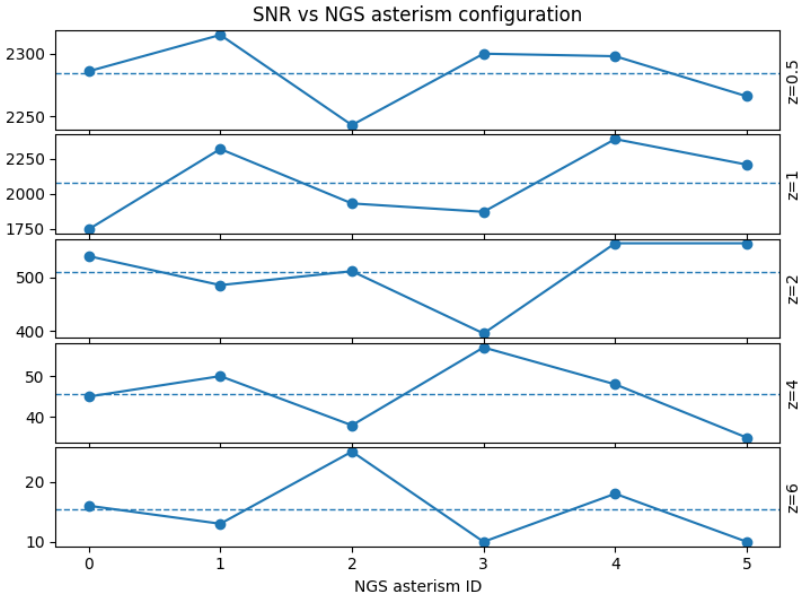

Figure 6.9: Distrubution of the computed SNR as function of the adopted NGS asterism configuration. Each slice corresponds to a redshift value, for which the dashed line represents the median of the SNR. This plot refers to the brightest clump in the ScopeSim simulated images. The values shown are refers to the J band.

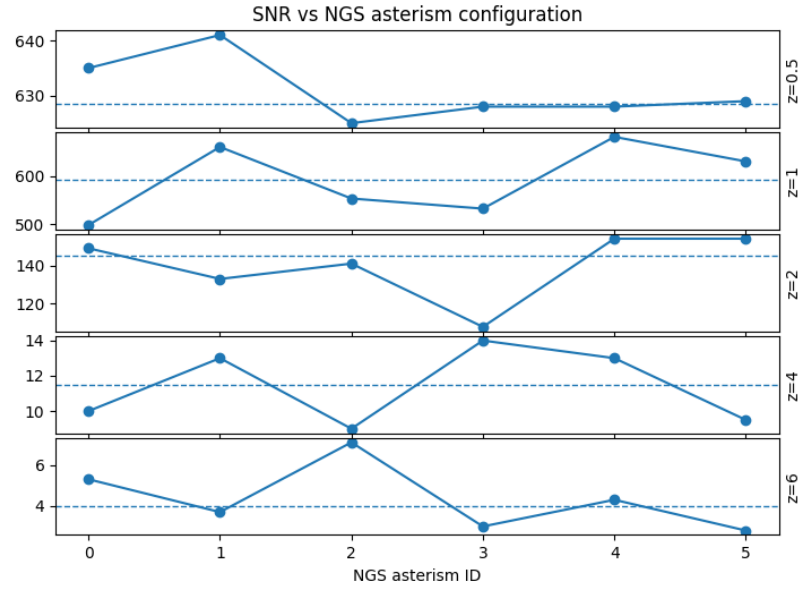

Figure 6.10: Distrubution of the computed SNR as function of the adopted NGS asterism configuration. Each slice corresponds to a redshift value, for which the dashed line represents the median of the SNR. This plot refers to the faintest clump in the ScopeSim simulated images. The values shown are refers to the J band.

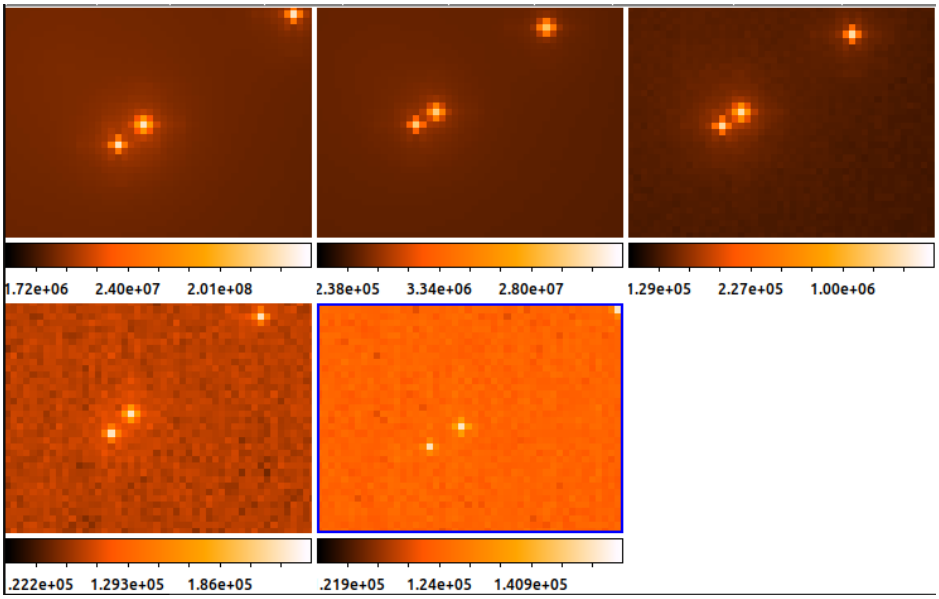

Figure 6.11: The five frames show the two clumps for which the deblending has been studied. Each frame shows the situation at a different redshift. In all the 5 cases the two clumps can be distinguished, even if not always the sampling of the inter-clump space is optimal.

Chapter 7

Summary, Results and Conclusions

To briefly reassume, the work done in this thesis consists in assessing the performance of MORFEO+MICADO in studies of high redshift star-forming clumps under different observing conditions; here I focused in particular on the impact caused by the particular choice of the NGS asterisms, which is a crucial ingredient for the AO correction.

The simulations of the MORFEO performances in terms of the quality of the adaptive optics corrected PSF have been done using the software TIPTOP, which allows to predict the instrumental PSF under several observing conditions. Then to assess the scientific capabilities of the MORFEO instrument coupled with the MICADO Near-IR imager, I have implemented the derived TIPTOP PSFs into simulations of realistic on-sky observations focusing, in the specific case, on high-z clumps. To this purpose I have used the ScopeSim software which has been designed to simulate images of user costumized sources and which accepts in input the PSFs provided by TIPTOP. The specific science case of star-forming clumps at high-z has been selected because it requires high spatial resolution and high contrast imaging, two elements that provide a perfect test bench for estimating the adaptive optics ability of ELT with its huge primary mirror. Also the possibility to resolve close clumps has been investigated in order to understand if the massive star-forming clumps with ≈ 100 pc size that are observed today with current telescopes could be broken into smaller, < 10 pc sub-structures suggested to exist based on the results from gravitationally lensed high-z systems.

Results and Conclusions

- **Impact of NGS asterism**: I found that the six NGS asterisms proposed by ESO perform all similarly well in terms of the resulting corrected PSFs. More specifically, I came up with the conclusion that whenever the NGSs are three, in a nearly triangular shape (not necessarly centered on the target) the correction is fairly good and the distance from the target and the position on the technical FoV do not produce major changes on the performance. Among the selected asterisms, the only one to have significant worse performances than the others is that where all the three NGS have H magnitudes fainter than 17: that is, although a magnitude range of H≈10-20 is allowed for the NGS, the correction is relatively poor if no star brighter than H≈17 is present. However, even the worst performing asterism among the six investigated presents a performance drop only around 8%;

- **Clump detectability**: From my simulations of clumps in a ±1 magnitude range around a reference value compatible with the properties of local SSC (see table 5.3), I found out that the vast majority of them results detected at all redshifts up to z=6. In the least performing band, i.e. the K band due to the intrinsically blue spectra of the simulated sources, the most luminous clump at z=6 is detected with a Signal-to-Noise ratio of $\approx$ 10, and higher in all the other bands. The least luminous clump, instead, results undetected in the K and H bands at z=6 (depending on the adopted asterism) but it is still clearly detected in the J band at z=6 and in all bands at lower redshifts;

- **NGS asterism effects on clump detectability**: In agreement with the results discussed in the first bullet point, I found that the selected NGS asterisms do not play any key role in the detection of the clumps, since the selected asterisms provide all very similar performances. Because of the limited number of simulations (only 20 clumps per image with fixed magnitude distribution around a reference value), random variations in the estimated SNR dominate over small-order effects induced by the different asterisms; indeed, no systematic trend toward lower performances from the worst asterism are observed in the clump simulations. This means that the 8% performance drop of the least performing asterism is overcome by other stronger noise sources.

- **Capability of resolving close clumps**: Two out of the 20 simulated clumps were positioned at a very close distance from each other, i.e. at a physical scale $\approx$ 100 pc. I found that up to z=6 it is always possible to distinguish them although the diffuse non-corrected haloes of the PSFs appear to merge. This result demonstrates the high potential of MORFEO+MICADO in breaking down the hierarchical structure of massive star-forming clumps in future high-z observations. In particular, the J band (see figure 6.11), with the best compromise between spatial resolution and sensitivuty, appears the most suitable one for these kind of observations.

Bibliography

[1] Adamo et al. “Probing cluster formation under extreme conditions: massive star clusters in blue compact galaxies”. In: (2011).

[2] Adamo et al. “The ages and metallicity of the globular clusters in the Sparkler”. In: (2022).

[3] Annibali et al. “MAORY + MICADO scientific analysis of the 1pfDM versus 2pfDM performance with realistic atmospheric profiles”. In: (2021).

[4] Annibali et al. “Young stellar populations and star clusters in NGC 1705”. In: (2009).

[5] Arcidiacono et al. “A numerical simulation study of an astrometry case for MORFEO at the ELT”. In: (2024).

[6] Arcidiacono et al. “A preliminary design review study of the scientific performance of MAORY (MORFEO)”. In: (2022).

[7] Arcidiacono et al. “Numerical simulations of MAORY MCAO module for the ELT”. In: (2018).

[8] Baruffolo et al. “MORFEO at ELT: preliminary design of the real-time computer”. In: (2022).

[9] Bian et al. “Local Analogs for High-redshift Galaxies: Resembling the Physical Conditions of the Interstellar Medium in High-redshift Galaxies”. In: (2016).

[10] Bournaud et al. “The Long Lives of Giant Clumps and the Birth of Outflows in Gas-rich Galaxies at High Redshift”. In: (2014).

[11] Brown et al. “Radii of Young Star Clusters in Nearby Galaxies”. In: (2021).

[12] Busoni et al. “MAORY/MORFEO at ELT: preliminary design of the adaptive optics subsystem”. In: (2022).

[13] Busoni et al. “MORFEO enters final design phase”. In: (2023).

[14] Calzetti et al. “The Brightest Young Star Clusters in NGC 5253.” In: (2015).

[15] Ceverino et al. “High-redshift clumpy discs and bulges in cosmological simulations”. In: (2010).

[16] Ceverino et al. “Rotational support of giant clumps in high-z disc galaxies”. In: (2012).

[17] Ciliegi et al. “MAORY: the adaptive optics module for the Extremely Large Telescope (ELT)”. In: (2020).

[18] Ciliegi et al. “MAORY/MORFEO at ELT: general overview up to the preliminary design and a look towards the final design”. In: (2022).

[19] Davies et al. “MICADO: first light imager for the E-ELT”. In: (2011).

[20] Davies et al. “MICADO: the E-ELT Adaptive Optics Imaging Camera”. In: (2012).

[21] Dekel et al. “Cold streams in early massive hot haloes as the main mode of galaxy formation”. In: (2009a).

[22] Dekel et al. “Steady outflows in giant clumps of high-z disc galaxies during migration and growth by accretion”. In: (2013).

[23] Di Matteo et al. “Evolution of galaxies in pairs: Learning from simulations”. In: (2008).

[24] Elmegreen et al. “Clumpy Galaxies in GOODS and GEMS: Massive Analogs of Local Dwarf Irregulars”. In: (2009).

[25] Elmegreen et al. “Hierarchical Star Formation in LEGUS Galaxies”. In: (2014).

[26] Immeli et al. “Gas physics, disk fragmentation, and bulge formation in young galaxies”. In: (2004a).

[27] Immeli et al. “Subgalactic Clumps at High Redshift: A Fragmentation Origin?” In: (2004b).

[28] Leschinski et al. “ScopeSim: A flexible general purpose astronomical instrument data simulation framework in Python”. In: (2021).

[29] Martins et al. “Near-Infrared spectroscopy of the super star cluster in NGC1705”. In: (2012).

[30] Martorano et al. “The Size-Mass relation at Rest-Frame 1.5µm from JWST/NIRCam in the COSMOS-WEB and PRIMER-COSMOS fields”. In: (2024).

[31] Messa et al. “Multiply lensed star forming clumps in the A521-sys1 galaxy at redshft 1”. In: (2022).

[32] Mestric et al. “Exploring the physical properties of lensed star-forming clumps at $2 < z < 6$”. In: (2022).

[33] Neichel et al. “TIPTOP: a new tool to efficiently predict your favorite AO PSF”. In: (2021).

[34] Peng et al. “Detailed Decomposition of Galaxy Images. II. Beyond Axisymmetric Models”. In: (2010).

[35] Plantet et al. “Sky coverage assessment for the European ELT: a joint evaluation for MAORY/MICADO and HARMONI”. In: (2022).

[36] Popesso et al. “The Main Sequence of star forming galaxies across cosmic times”. In: (2022).

[37] Reina-Campos et al. “Introducing EMP-Pathfinder: modelling the simultaneous formation and evolution of stellar clusters in their host galaxies”. In: (2022).

[38] Sattari et al. “Fraction of clumpy star-forming galaxies at $0.5 < z < 3$ in UVCANDELS: Dependence on stellar mass and environment”. In: (2321).

[39] Scoville et al. “Cosmic Evolution of Gas and Star Formation”. In: (2023).

[40] Shibuya et al. “MORPHOLOGIES OF 190,000 GALAXIES AT z=0-10 REVEALED WITH HST LEGACY DATA. II. EVOLUTION OF CLUMPY GALAXIES Morphologies of 190.000 galaxies at redshift z=0-10 revealed with HST Legacy data. Evolution of clumpy galaxies.” In: (2016).

[41] Tacconi et al. “High molecular gas fractions in normal massive star-forming galaxies in the young Universe”. In: (2010).

[42] van der Wel et al. “3D-HST+CANDELS: The evolution of the galaxy Size-Mass distribution since z=3”. In: (2014).

[43] van der Wel et al. “Stellar Half-Mass Radii of $0.5 < z < 2.3$ Galaxies: Comparison with JWST/NIRCam Half-Light Radii”. In: (2023).

[44] Vanzella et al. “An extremely metal poor star complex in the reionization era: Approaching population III stars with JWST”. In: (2023).

[45] Vanzella et al. “Early results from GLASS-JWST. VII: evidence for lensed, gravitationally bound proto-globular clusters at z=4 in the Hubble Frontier Field A2744”. In: (2022).

[46] Vanzella et al. “Massive Star cluster formation under the microscope at z=6”. In: (2018).

[47] Zanella et al. “A contribution of star-forming clumps and accreting satellites to the mass assembly of z 2 galaxies”. In: (2019).

[48] Zanella et al. “An extremely young massive clump forming by gravitational collapse in a primordial galaxy”. In: (2015).

[49] Bournaud. “Bulge growth through disk instabilities in high-redshift galaxies”. In: (2015).

[50] Ciotti. “Stellar systems following the R 1/n law”. In: (1991).

[51] Hubble. “Extragalactic Nebulae”. In: (1926).

[52] Noll. “Zernike polynomials and atmospheric turbulence”. In: (1976).

Appendices

Appendix A

Appendix: image gallery

A.1 PSF gallery

For completeness here are reported all the PSF obtained with al the possible combination of asterisms and IJHK filters. Only the PSF in the centre of the field of view is reported, for a total of 24 images, 6 for each observing filter.

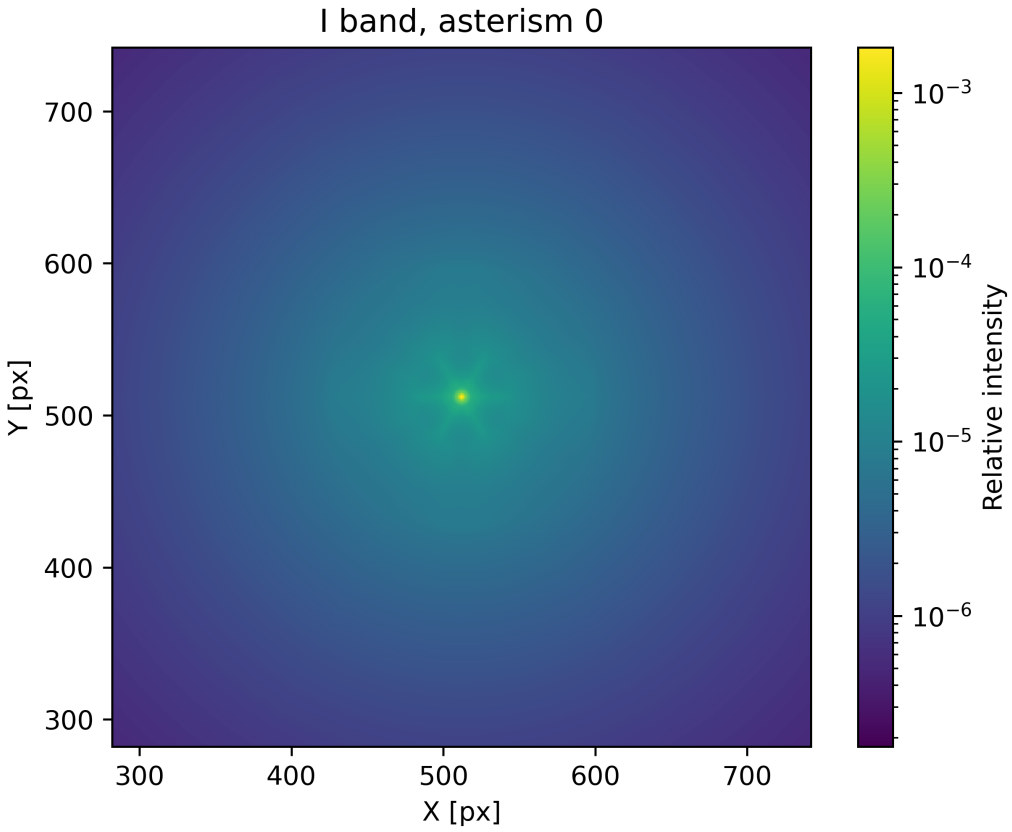
I band, asterism 0
700
600
500
400
300
Y [px]
300
400
500
600
700
X [px]
10^{-3}
10^{-4}
10^{-5}
10^{-6}
Relative intensity

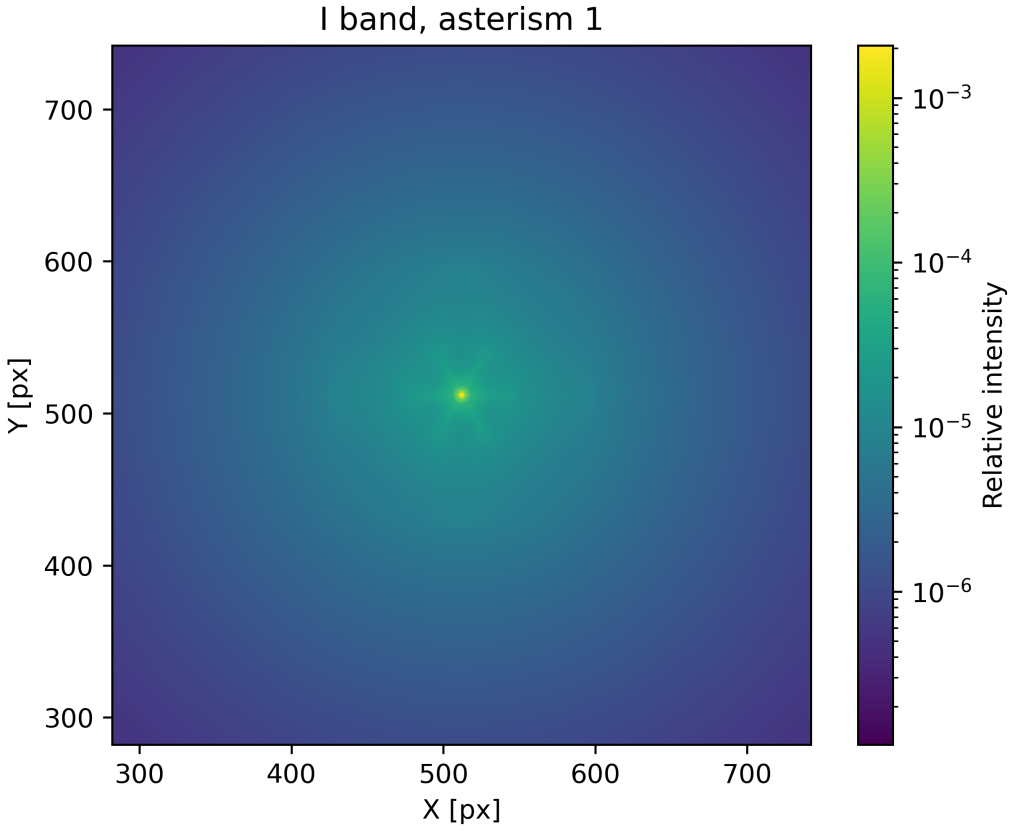
I band, asterism 1
700
600
500
400
300
Y [px]
300
400
500
600
700
X [px]
10^{-3}
10^{-4}
10^{-5}
10^{-6}
Relative intensity

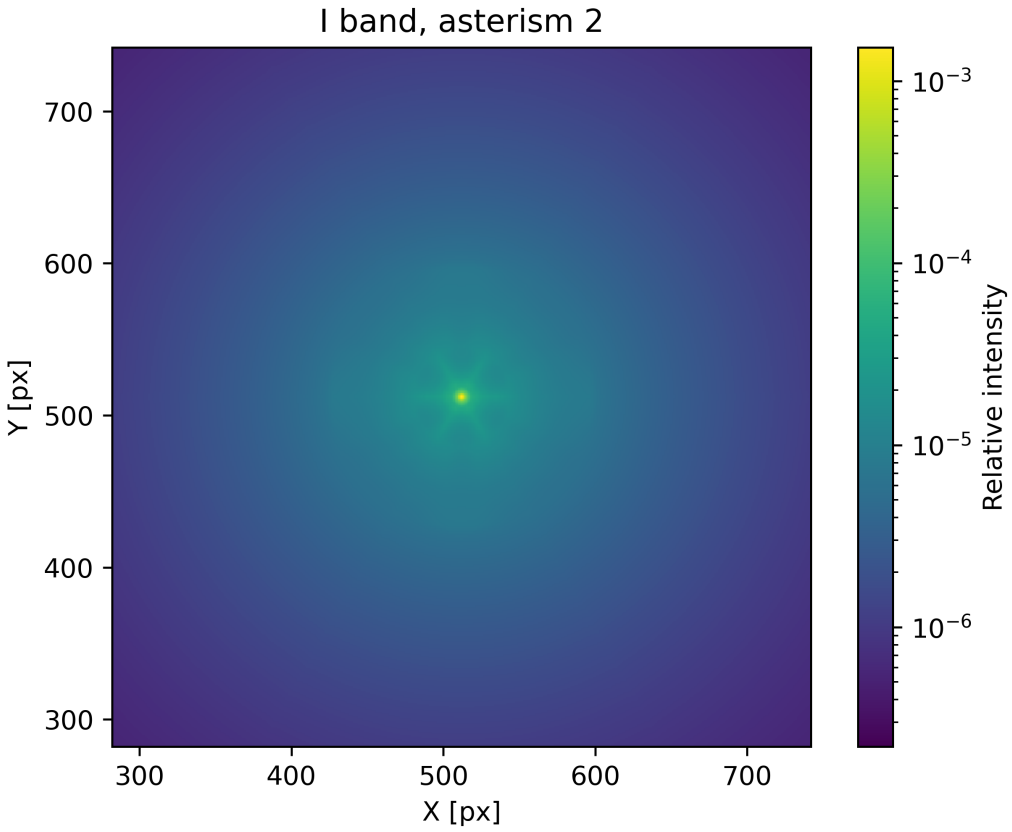
I band, asterism 2
700
600
500
400
300
Y [px]
300
400
500
600
700
X [px]
10^{-3}
10^{-4}
10^{-5}
10^{-6}
Relative intensity

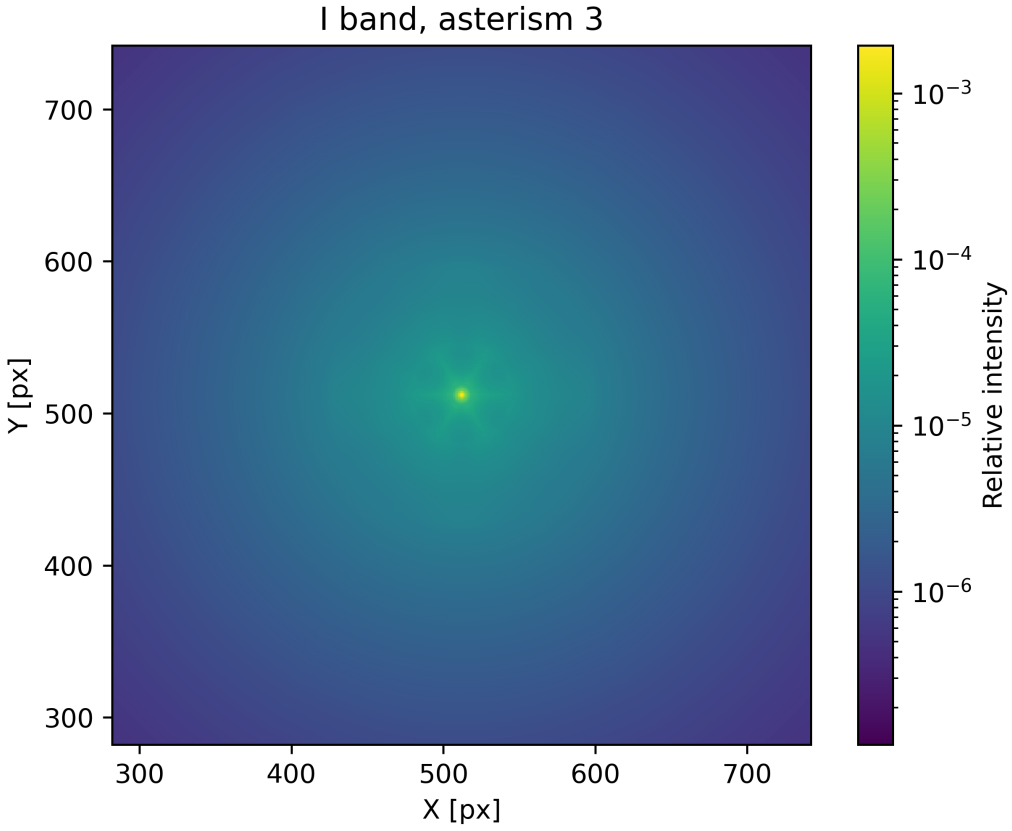
I band, asterism 3
700
600
500
400
300
Y [px]
300
400
500
600
700
X [px]
10^{-3}
10^{-4}
10^{-5}
10^{-6}
Relative intensity

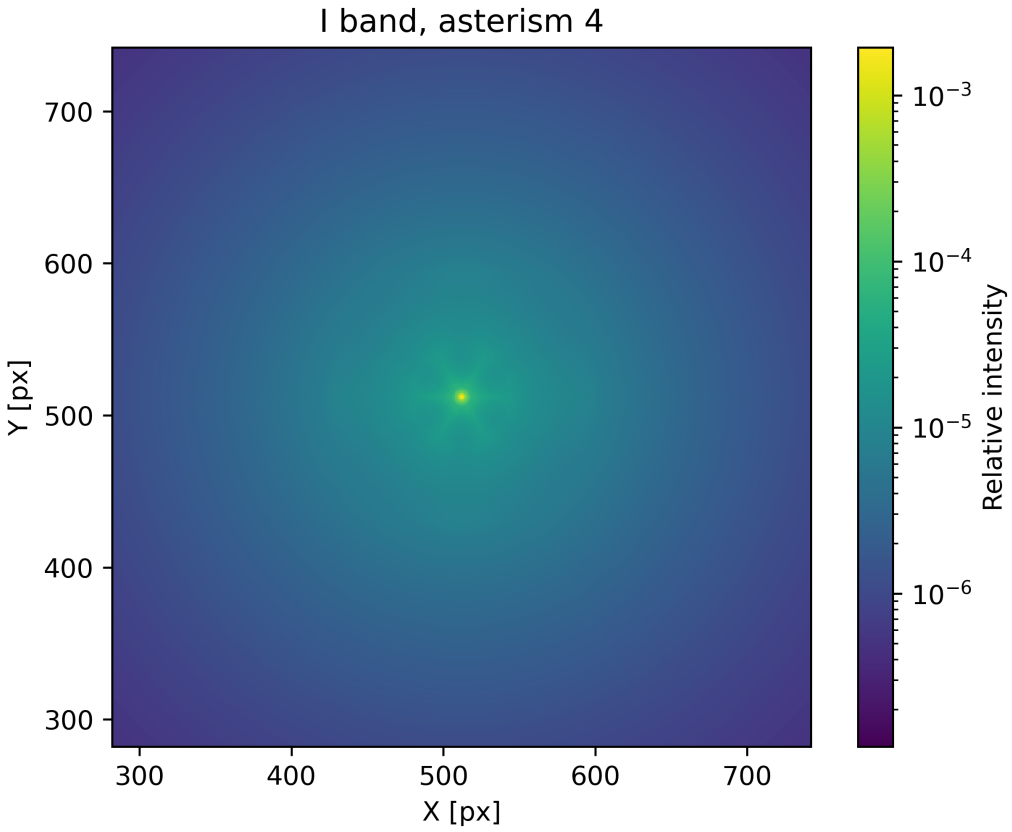
I band, asterism 4
700
600
500
400
300
Y [px]
300
400
500
600
700
X [px]
10^{-3}
10^{-4}
10^{-5}
10^{-6}
Relative intensity

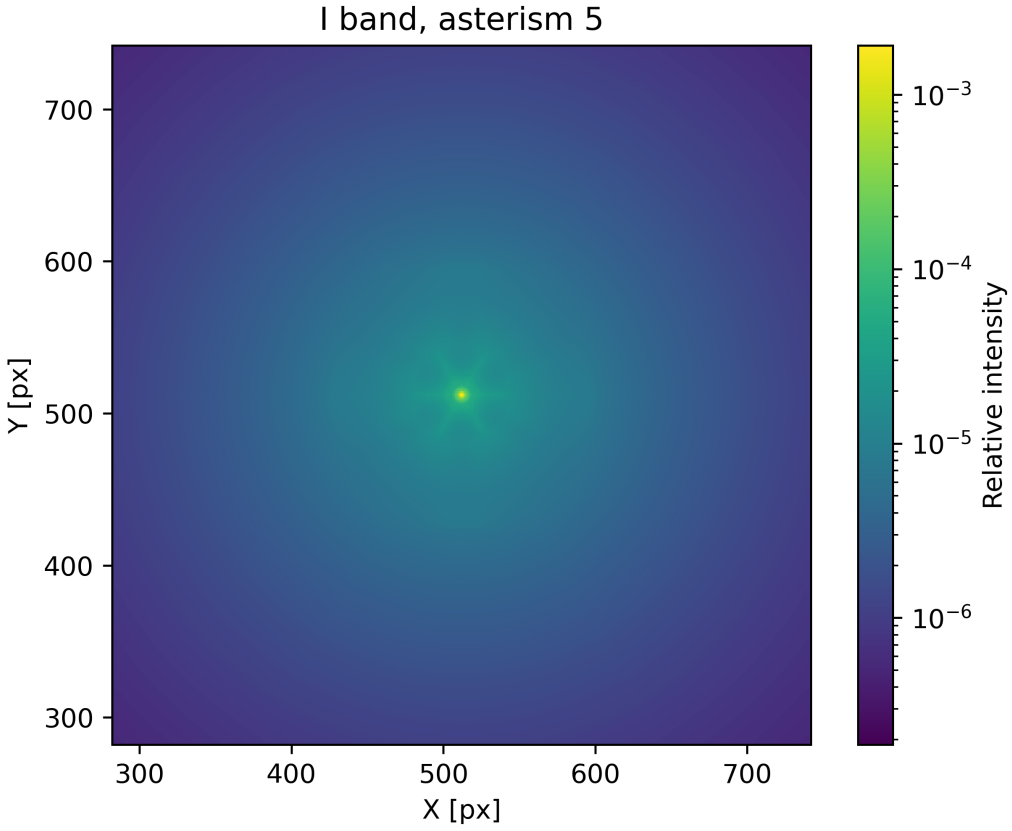
I band, asterism 5
700
600
500
400
300
Y [px]
300
400
500
600
700
X [px]
10^{-3}
10^{-4}
10^{-5}
10^{-6}
Relative intensity

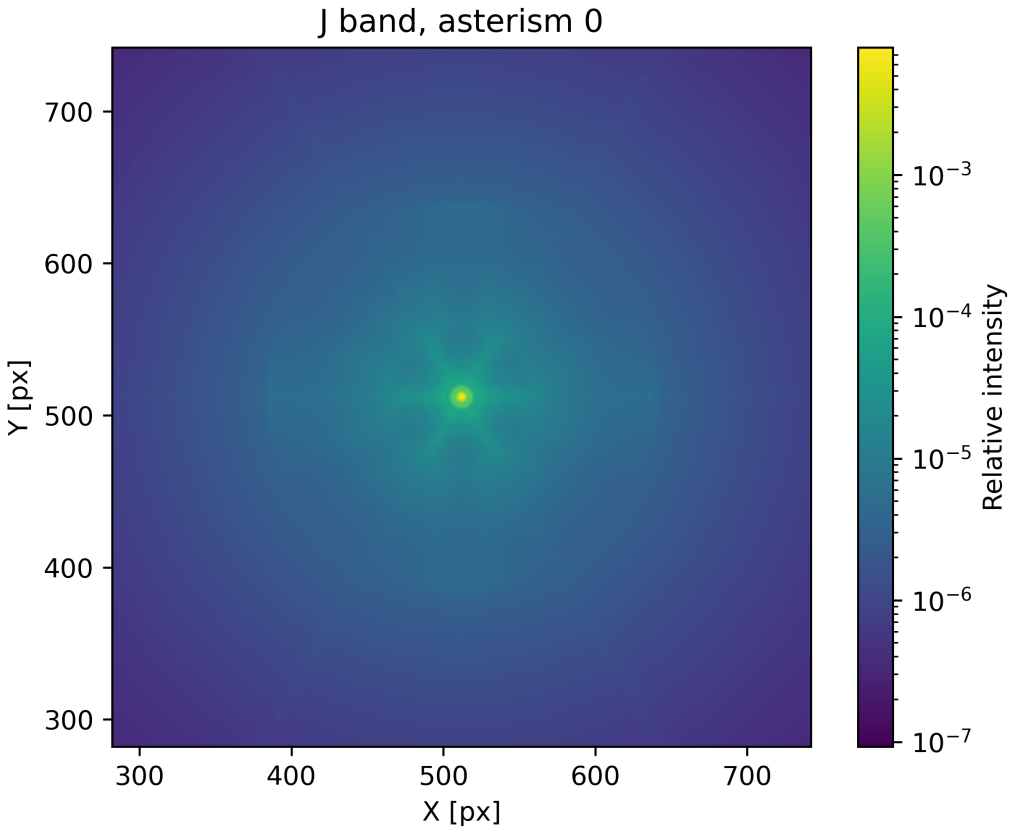
J band, asterism 0
700
600
500
400
300
Y [px]
300
400
500
600
700
X [px]
10^{-3}
10^{-4}
10^{-5}
10^{-6}
10^{-7}
Relative intensity

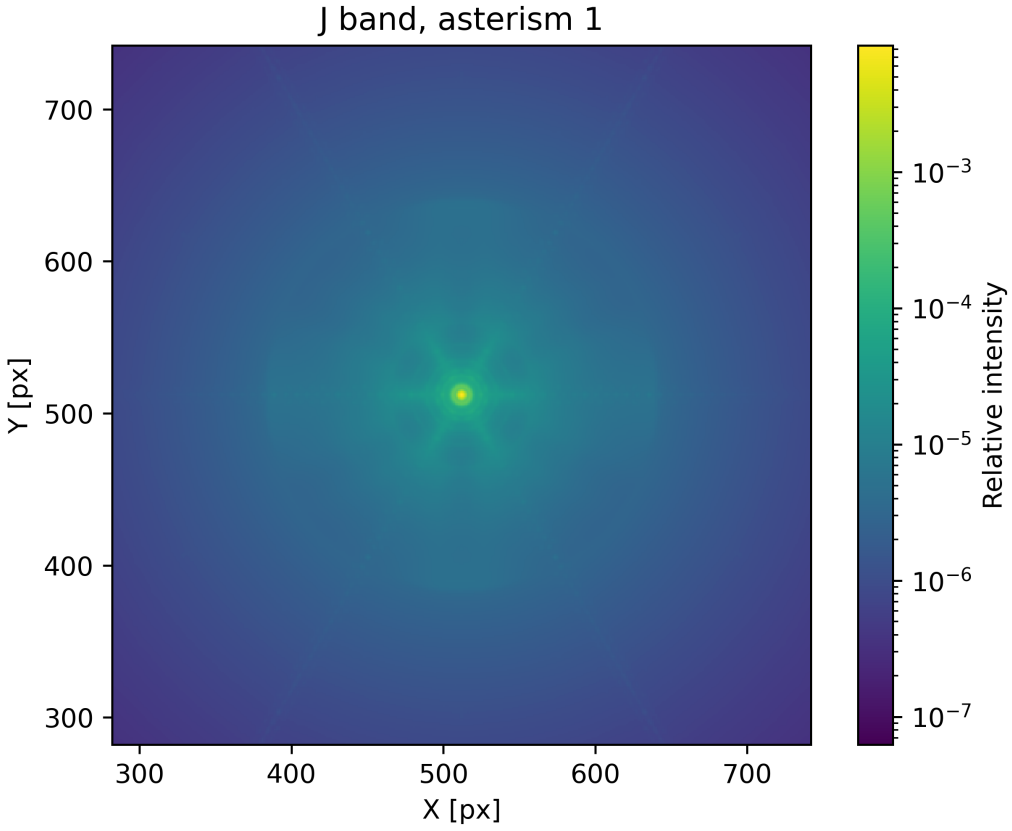
J band, asterism 1
700
600
500
400
300
Y [px]
300
400
500
600
700
X [px]
10^{-3}
10^{-4}
10^{-5}
10^{-6}
10^{-7}
Relative intensity

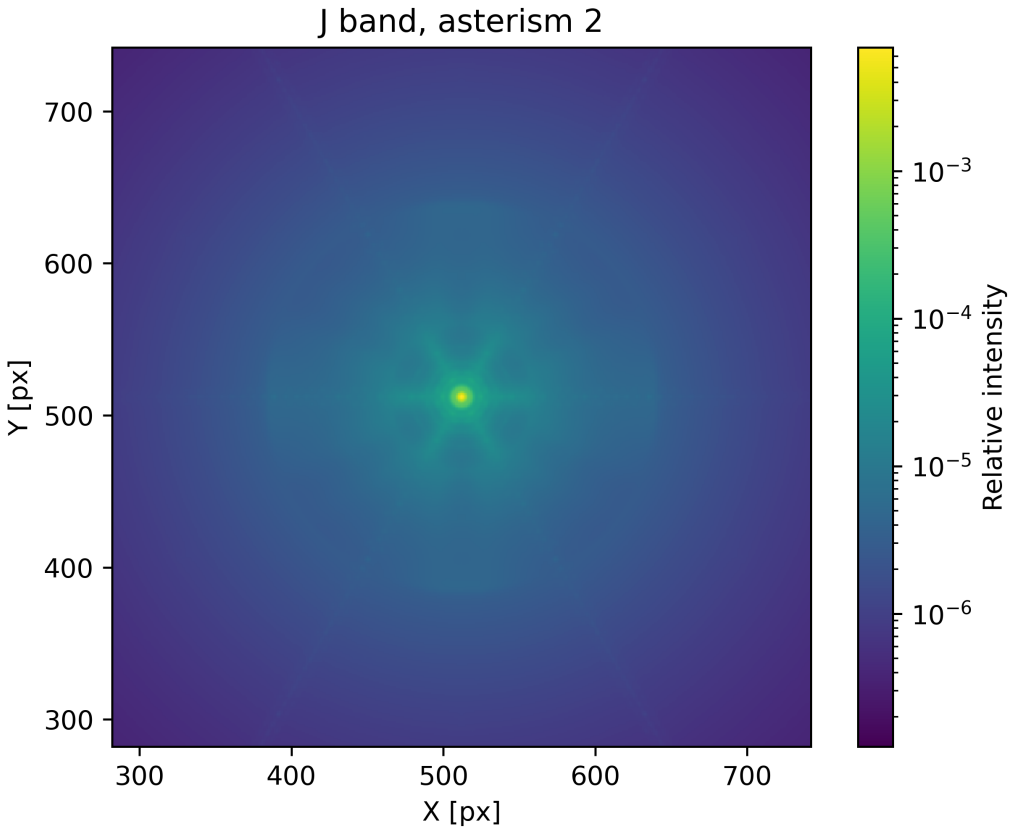
J band, asterism 2
700
600
500
400
300
Y [px]
300
400
500
600
700
X [px]
10^{-3}
10^{-4}
10^{-5}
10^{-6}
Relative intensity

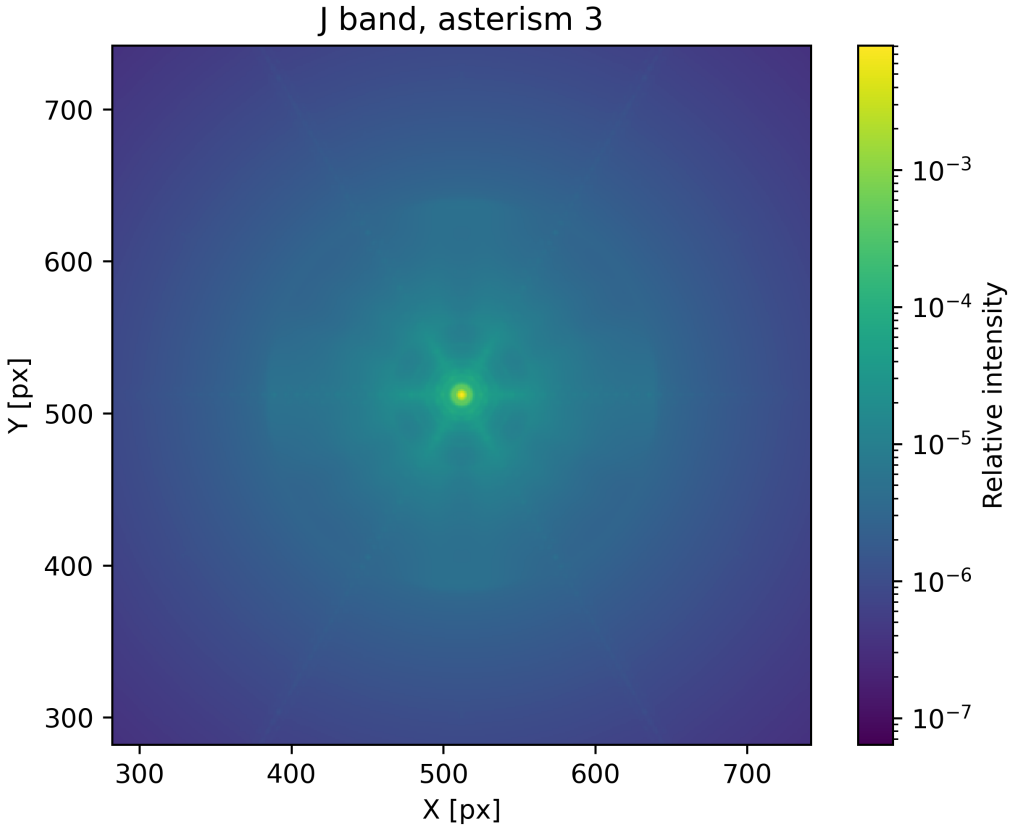
J band, asterism 3
700
600
500
400
300
Y [px]
300
400
500
600
700
X [px]
10^{-3}
10^{-4}
10^{-5}
10^{-6}
10^{-7}
Relative intensity

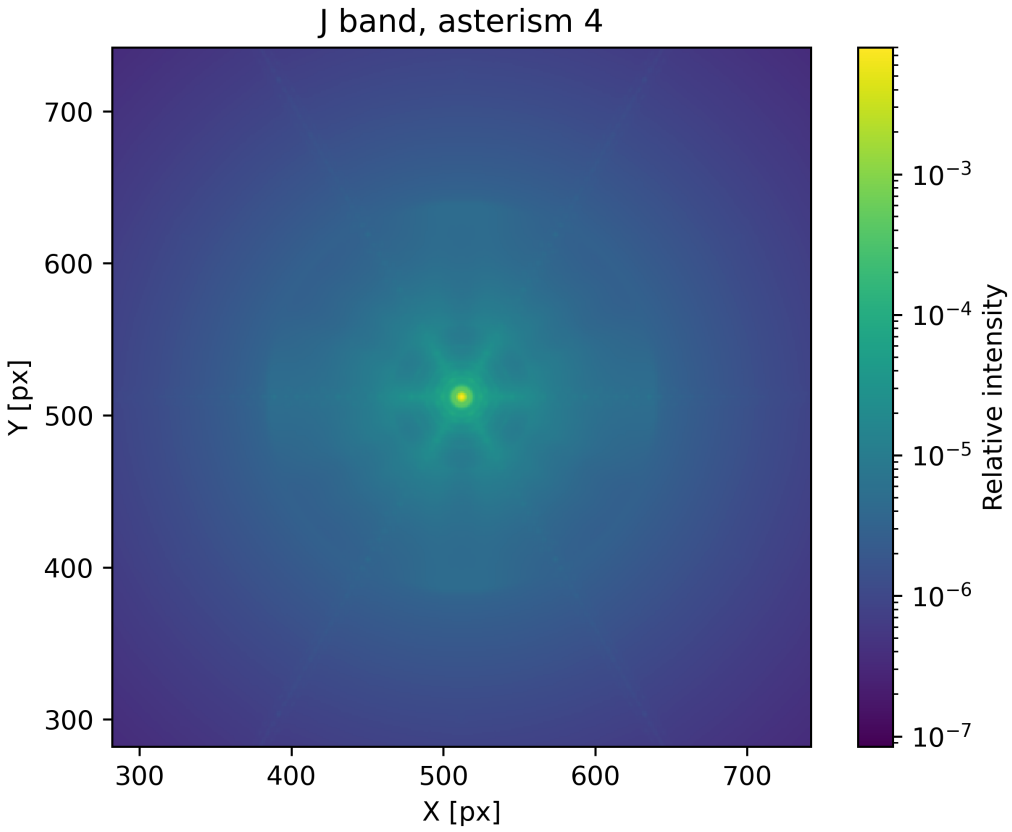
J band, asterism 4
700
600
500
400
300
Y [px]
300
400
500
600
700
X [px]
10^{-3}
10^{-4}
10^{-5}
10^{-6}
10^{-7}
Relative intensity

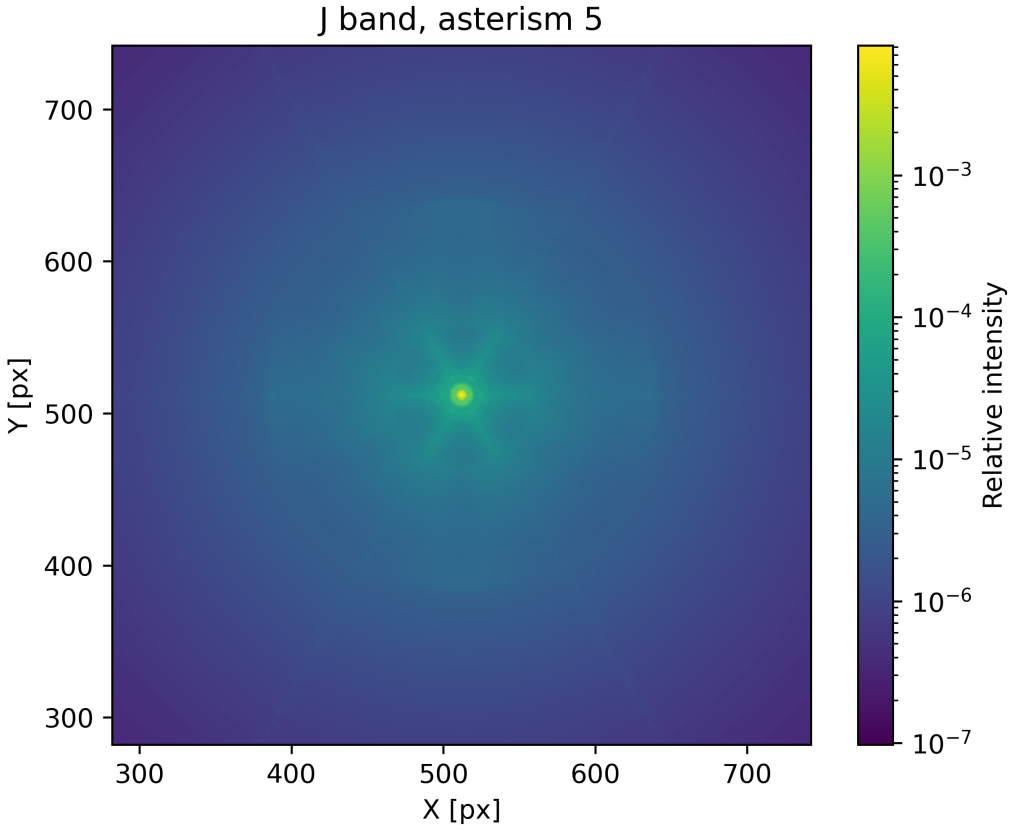
J band, asterism 5
700
600
500
400
300
Y [px]
300
400
500
600
700
X [px]
10^{-3}
10^{-4}
10^{-5}
10^{-6}
10^{-7}
Relative intensity

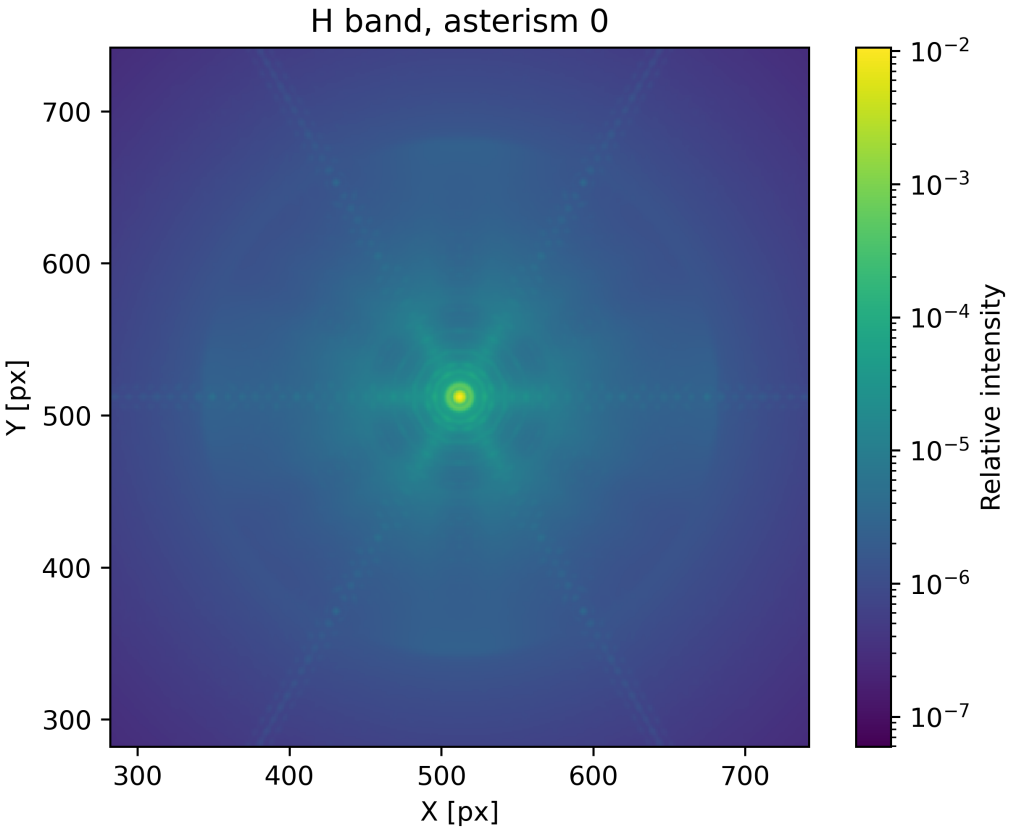
H band, asterism 0
700
600
500
400
300
Y [px]
300
400
500
600
700
X [px]
10^{-2}
10^{-3}
10^{-4}
10^{-5}
10^{-6}
10^{-7}
Relative intensity

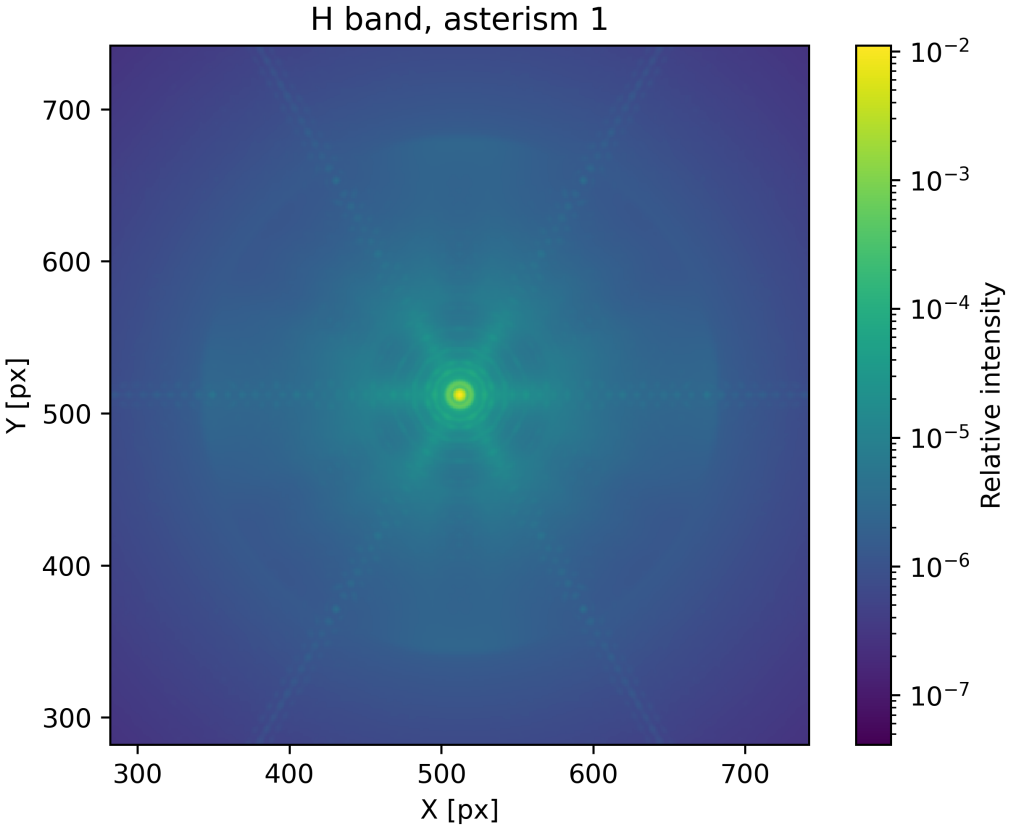
H band, asterism 1
700
600
500
400
300
Y [px]
300
400
500
600
700
X [px]
10^{-2}
10^{-3}
10^{-4}
10^{-5}
10^{-6}
10^{-7}
Relative intensity

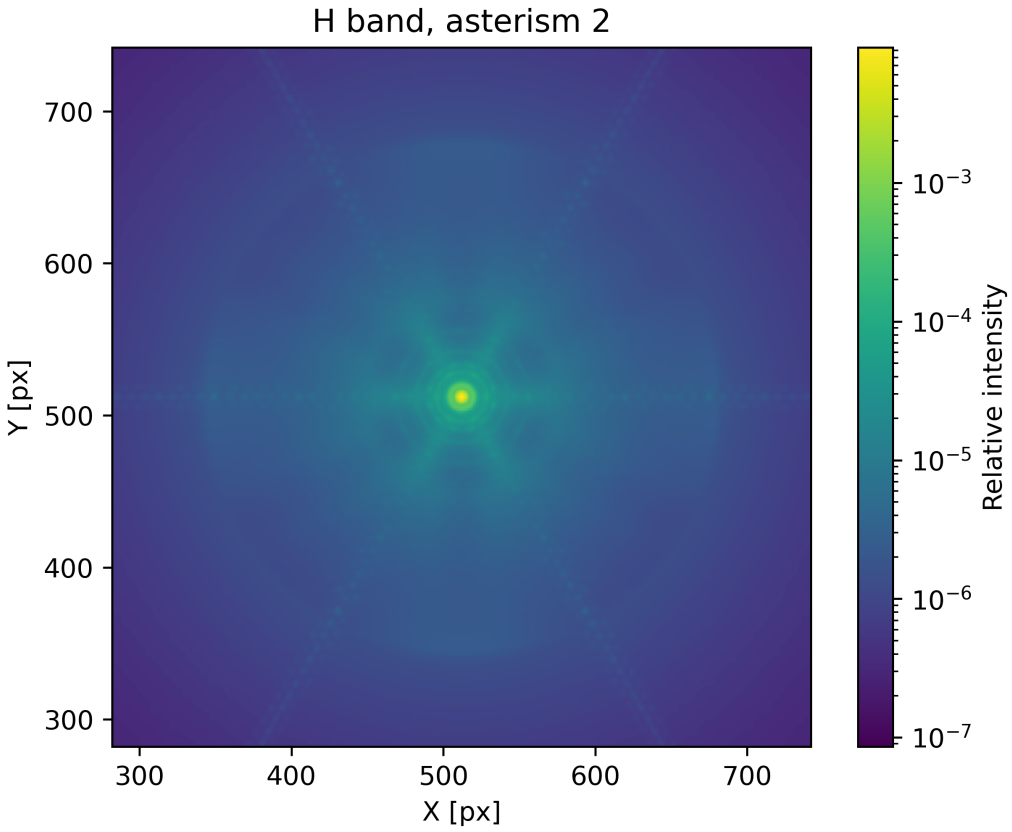
H band, asterism 2
700
600
500
400
300
Y [px]
300
400
500
600
700
X [px]
10^{-3}
10^{-4}
10^{-5}
10^{-6}
10^{-7}
Relative intensity

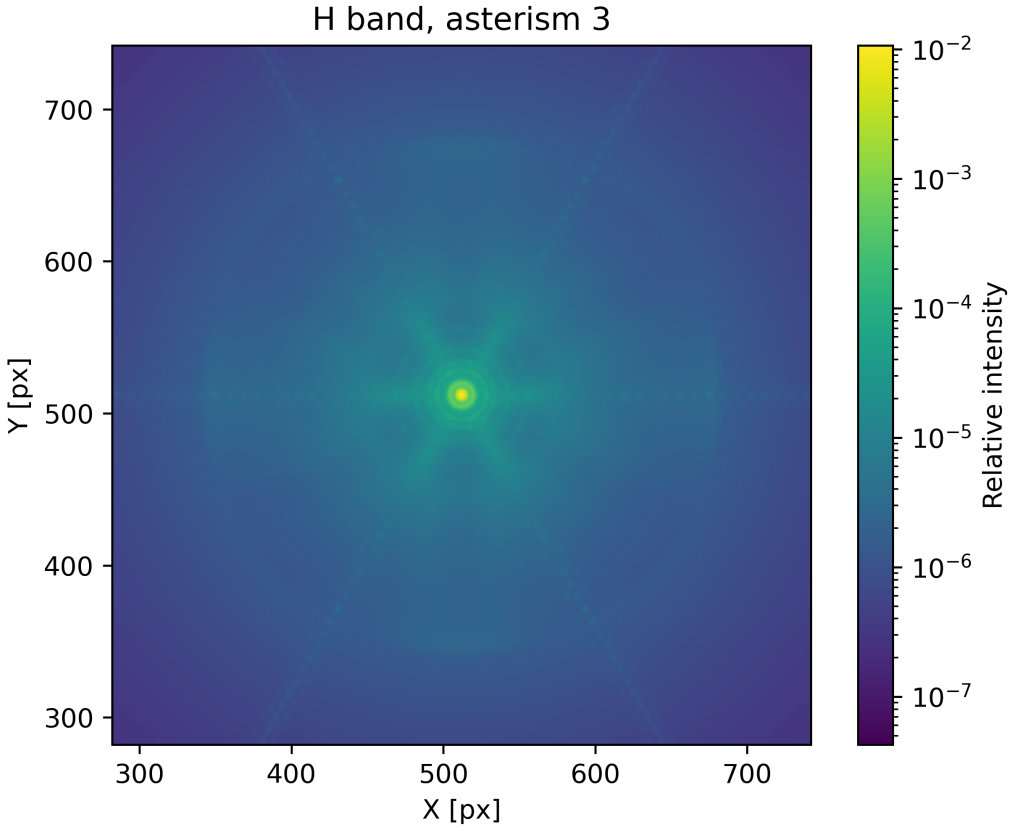
H band, asterism 3
700
600
500
400
300
Y [px]
300
400
500
600
700
X [px]
10^{-2}
10^{-3}
10^{-4}
10^{-5}
10^{-6}
10^{-7}
Relative intensity

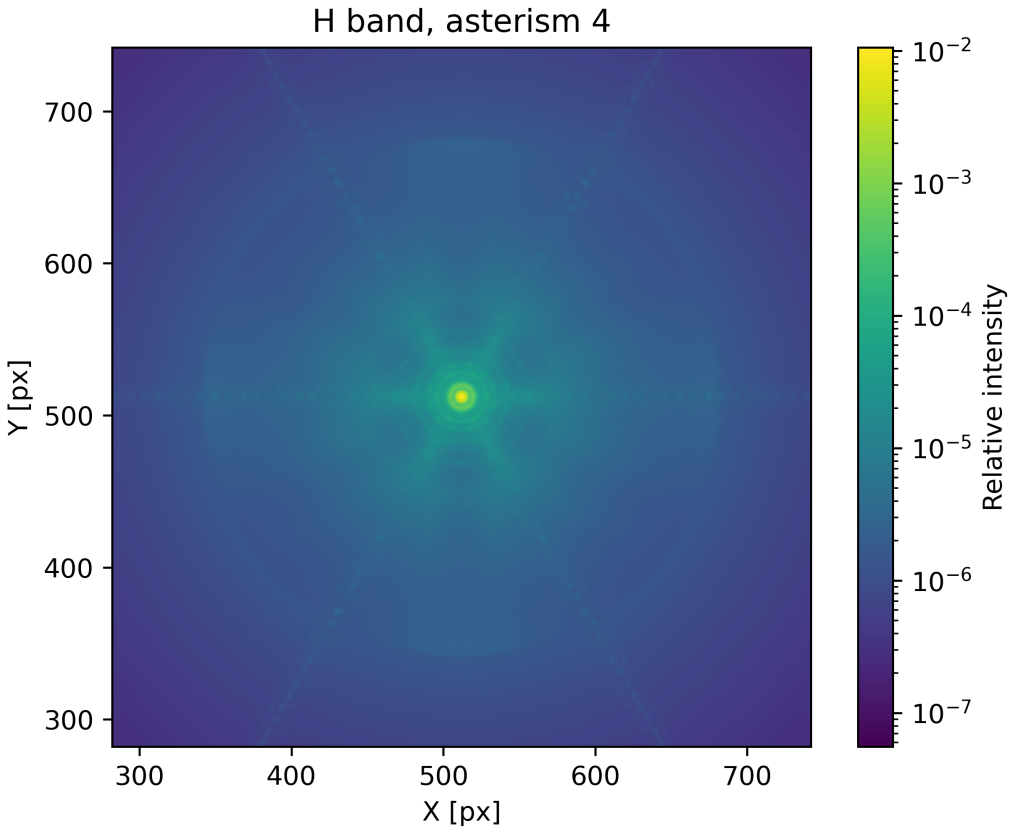
H band, asterism 4
700
600
500
400
300
Y [px]
300
400
500
600
700
X [px]
10^{-2}
10^{-3}
10^{-4}
10^{-5}
10^{-6}
10^{-7}
Relative intensity

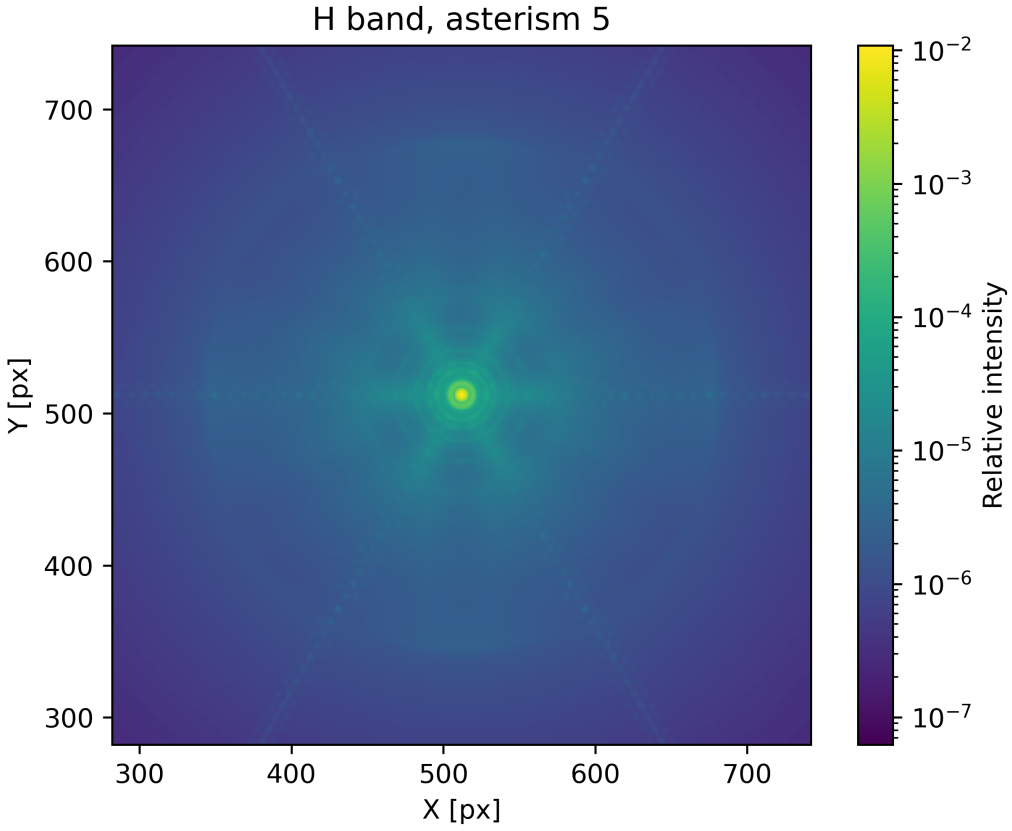
H band, asterism 5
700
600
500
400
300
Y [px]
300
400
500
600
700
X [px]
10^{-2}
10^{-3}
10^{-4}
10^{-5}
10^{-6}
10^{-7}
Relative intensity

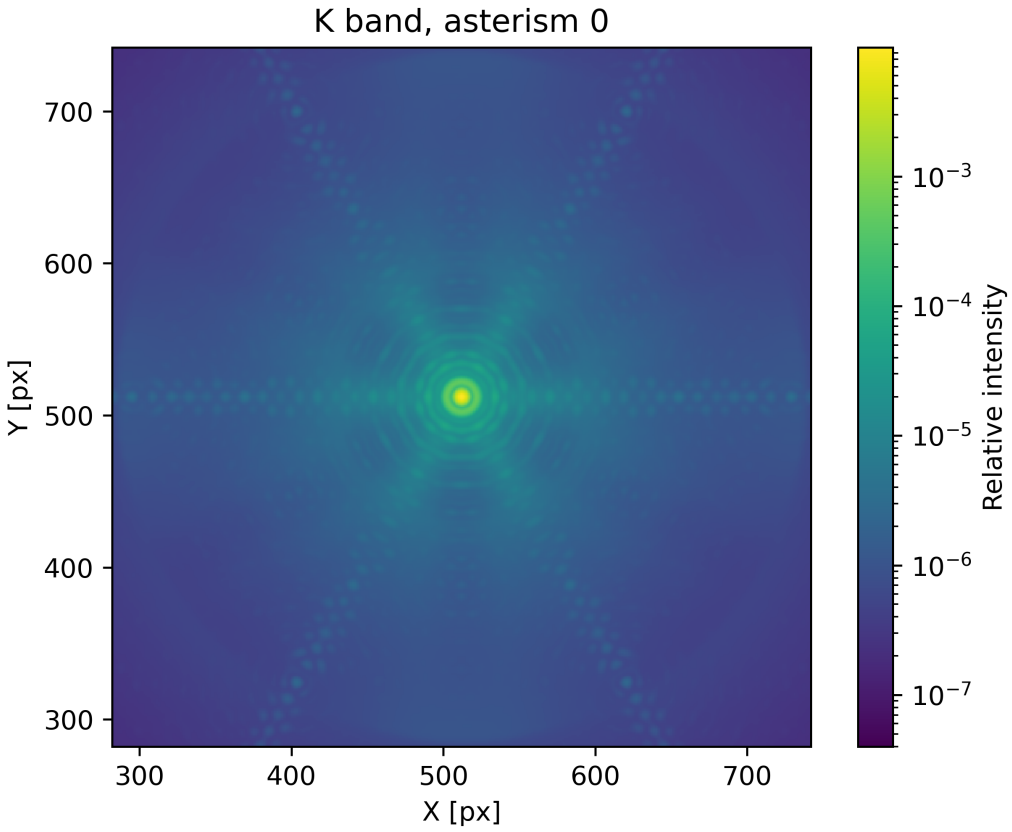
K band, asterism 0
700
600
500
400
300
Y [px]
300
400
500
600
700
X [px]
10^{-3}
10^{-4}
10^{-5}
10^{-6}
10^{-7}
Relative intensity

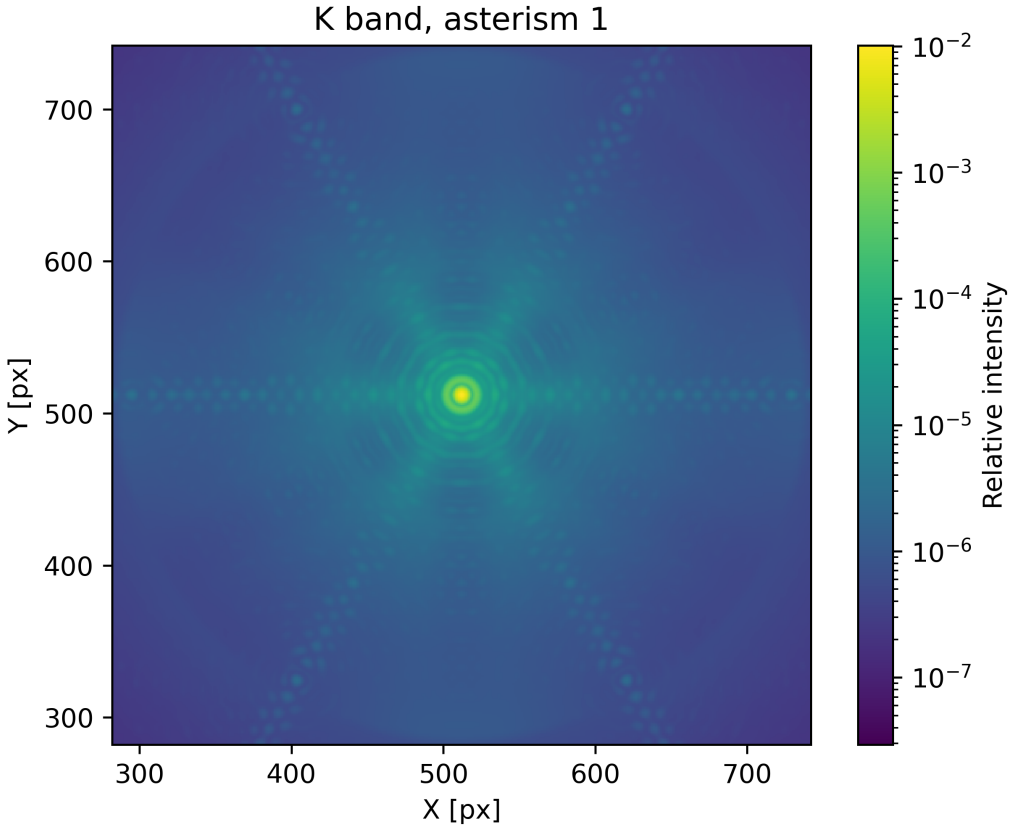
K band, asterism 1
700
600
500
400
300
Y [px]
300
400
500
600
700
X [px]
10^{-2}
10^{-3}
10^{-4}
10^{-5}
10^{-6}
10^{-7}
Relative intensity

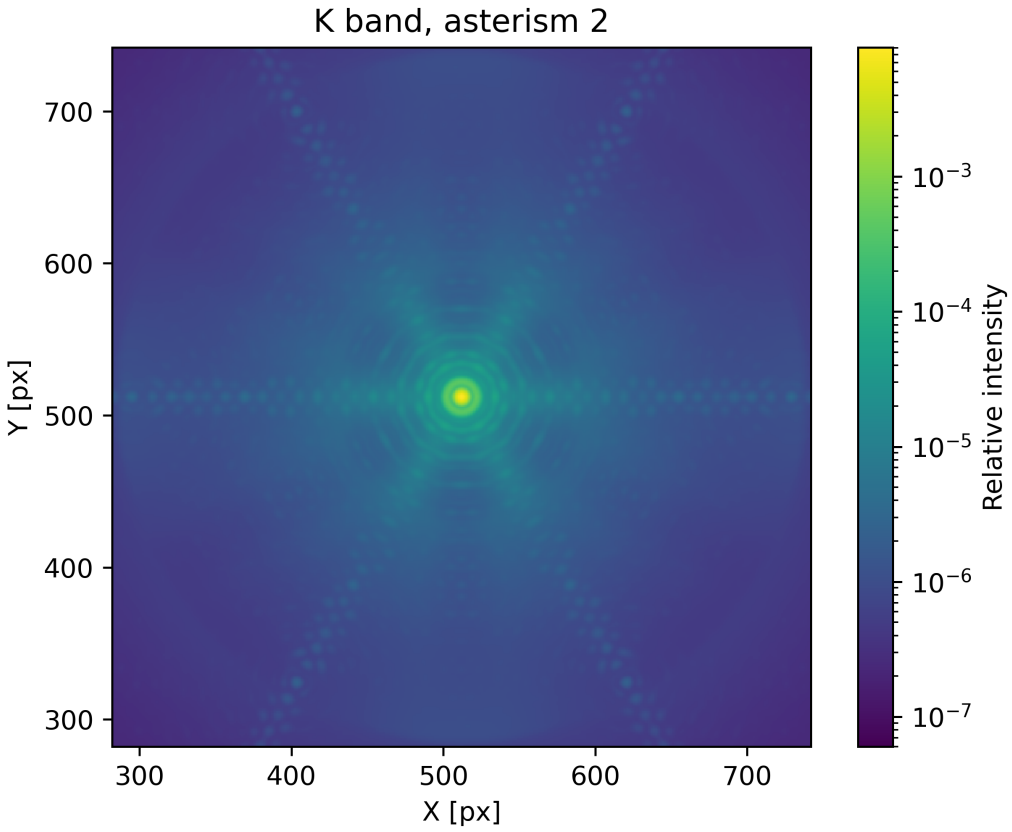
K band, asterism 2
700
600
500
400
300
Y [px]
300
400
500
600
700
X [px]
10^{-3}
10^{-4}
10^{-5}
10^{-6}
10^{-7}
Relative intensity

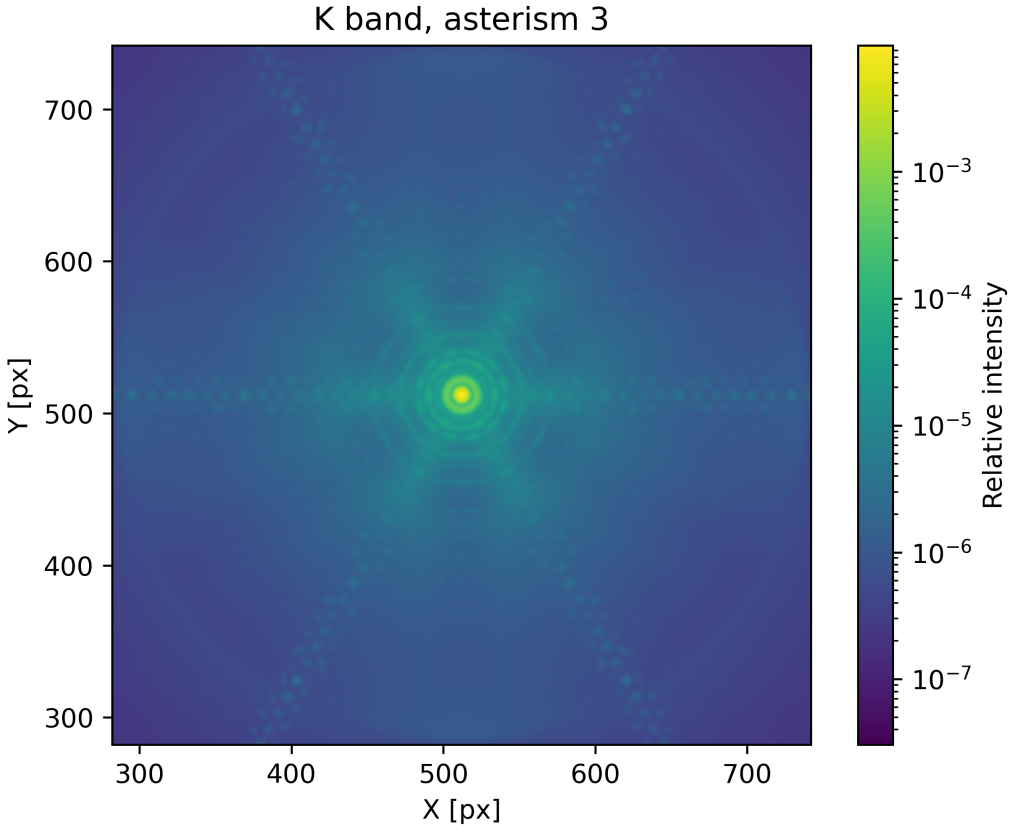
K band, asterism 3
700
600
500
400
300
Y [px]
300
400
500
600
700
X [px]
10^{-3}
10^{-4}
10^{-5}
10^{-6}
10^{-7}
Relative intensity

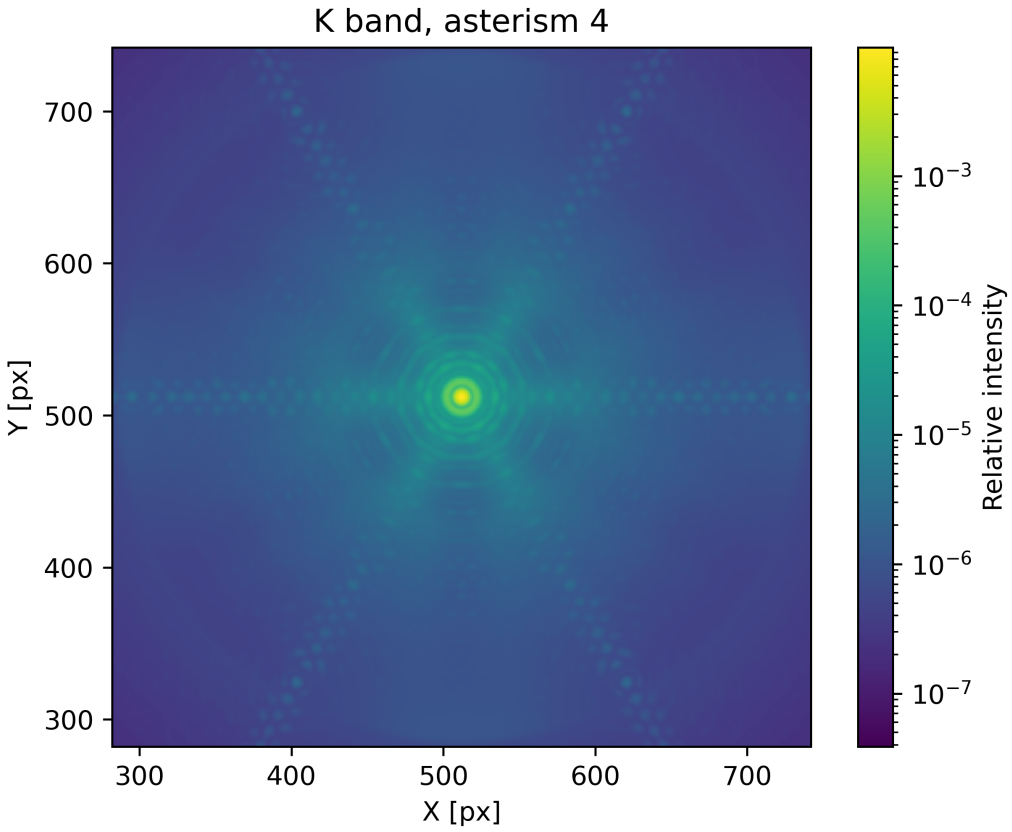
K band, asterism 4
700
600
500
400
300
Y [px]
300
400
500
600
700
X [px]
10^{-3}
10^{-4}
10^{-5}
10^{-6}
10^{-7}
Relative intensity

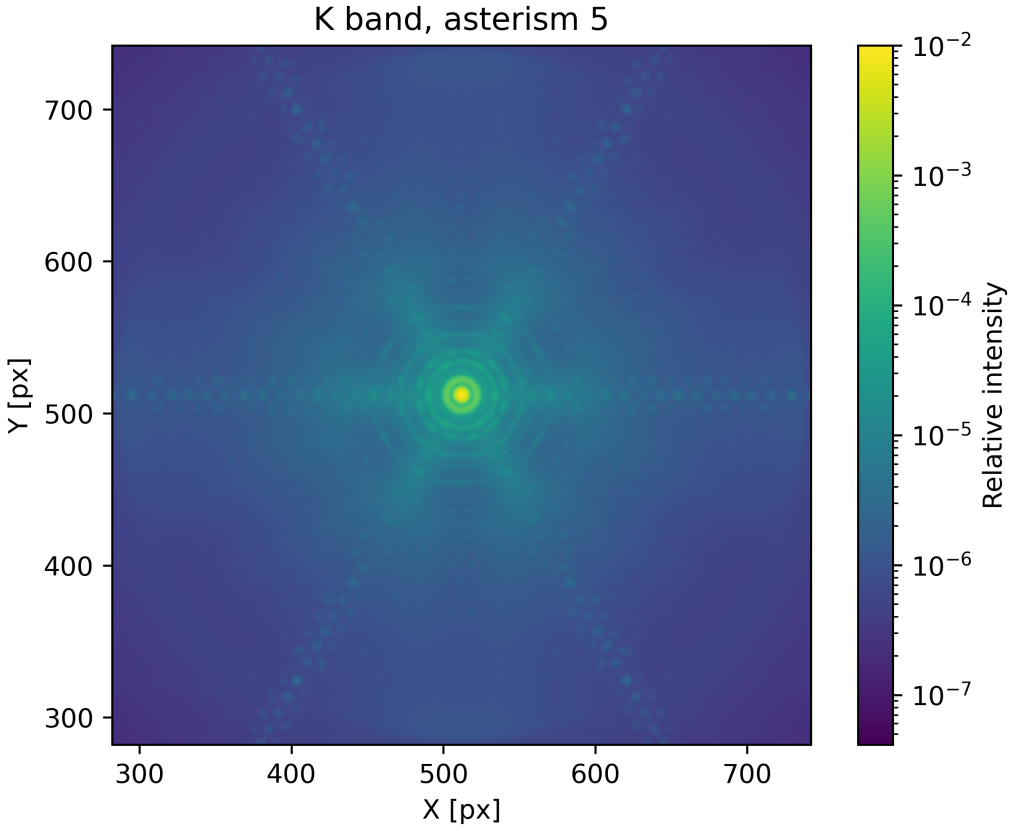
K band, asterism 5
700
600
500
400
300
Y [px]
300
400
500
600
700
X [px]
10^{-2}
10^{-3}
10^{-4}
10^{-5}
10^{-6}
10^{-7}
Relative intensity

A.2 ScopeSim output image gallery

Here is presented a gallery showing the image outputs produced by Scopesim. Since all the asterisms perform similar, only the case of asterism 0 is presented in all the available bands at all redshifts.

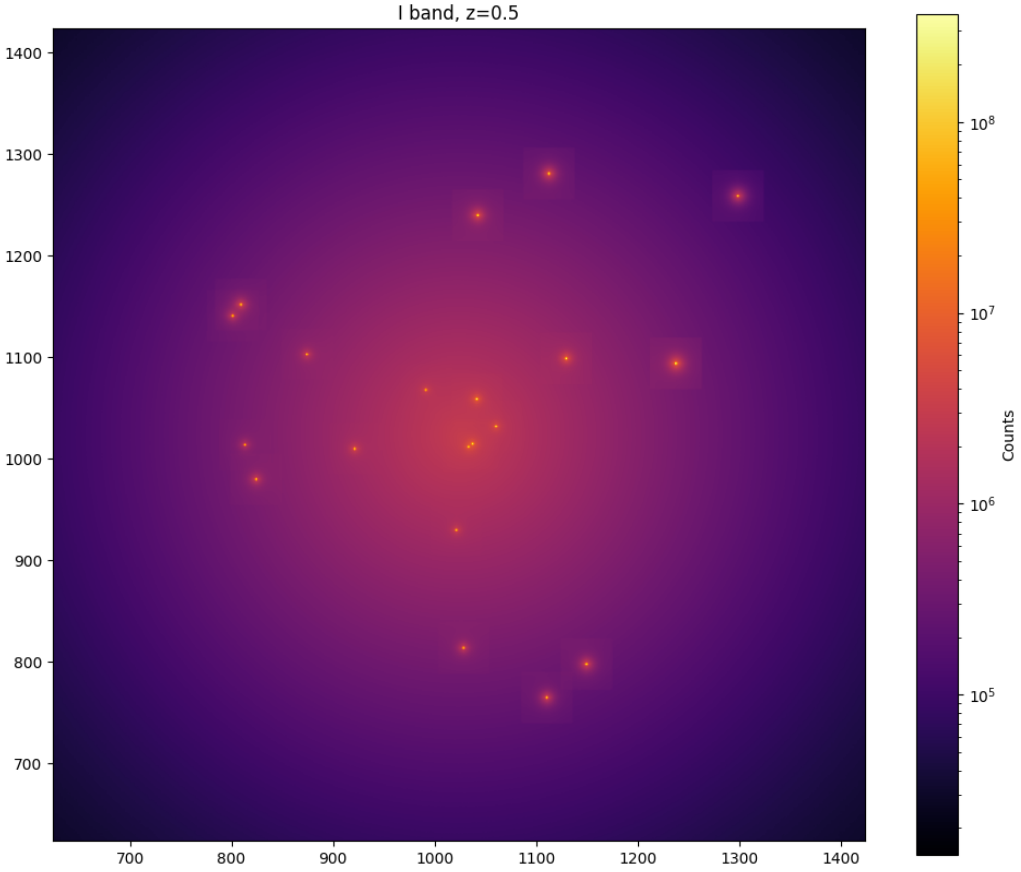

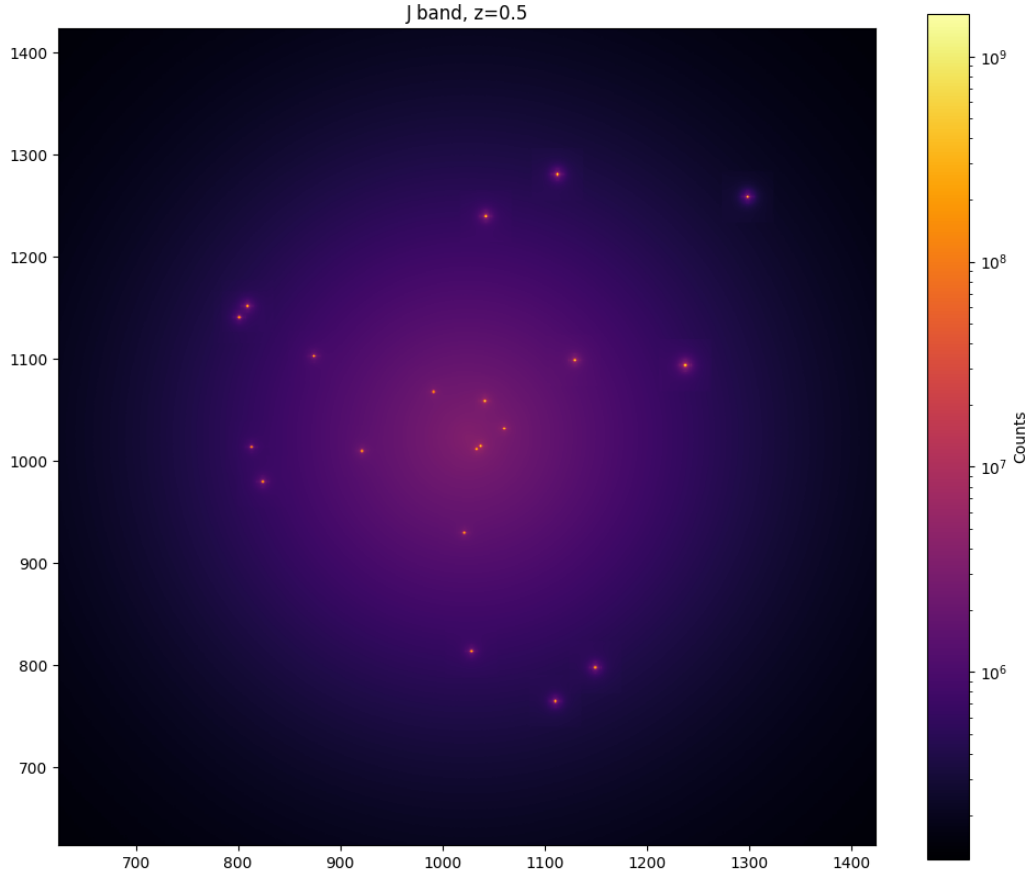
J band, z=0.5
1400
1300
1200
1100
1000
900
800
700
700
800
900
1000
1100
1200
1300
1400
10^9
10^8
10^7
10^6
Counts

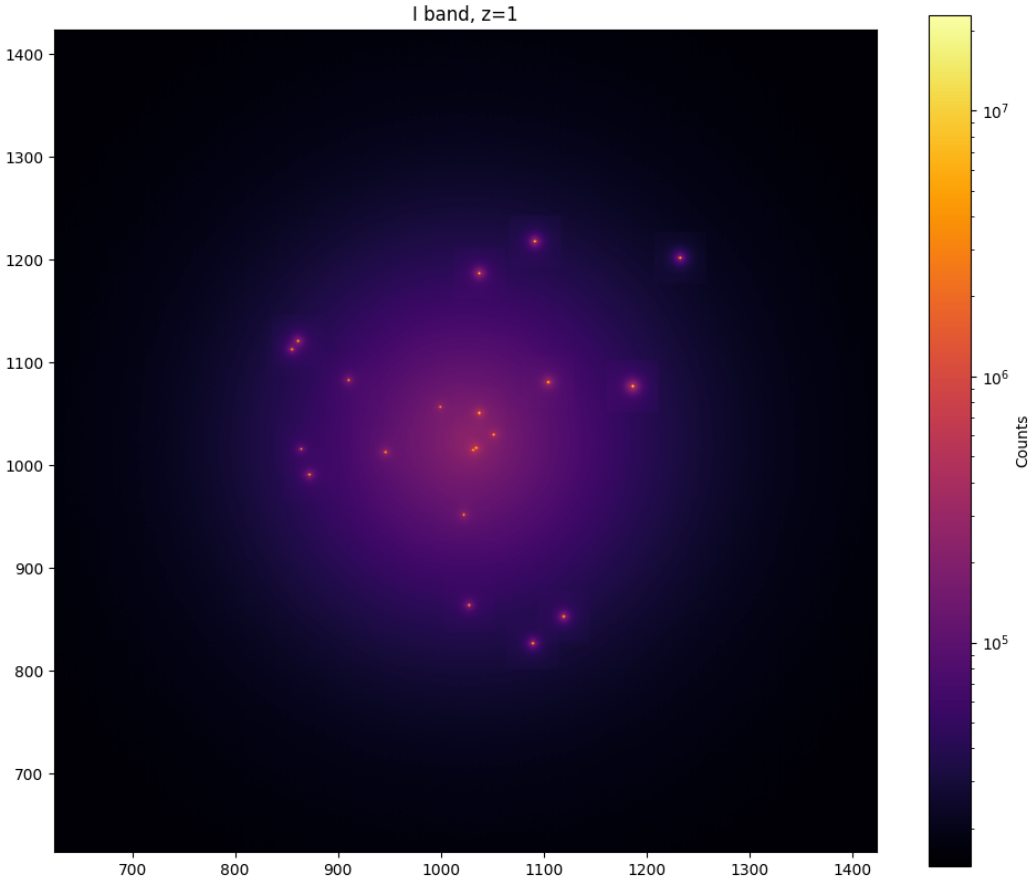
I band, z=1
1400
1300
1200
1100
1000
900
800
700
700
800
900
1000
1100
1200
1300
1400
10^7
10^6
10^5
Counts

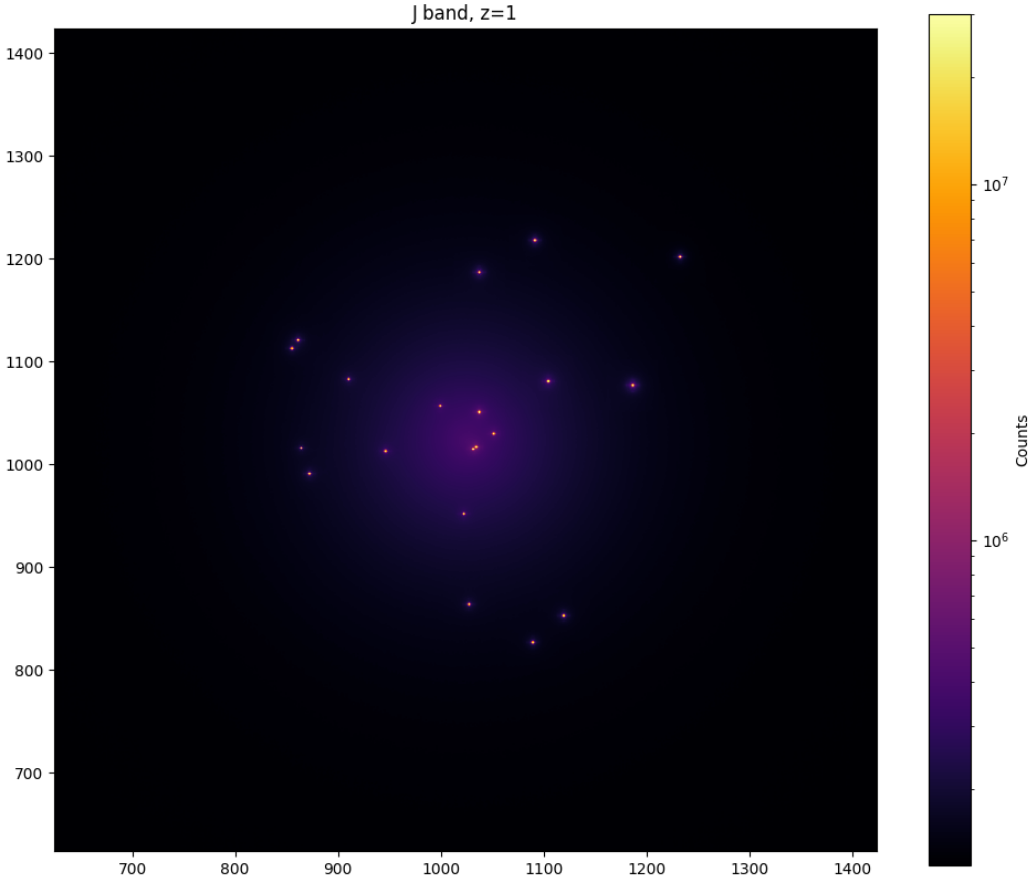
J band, z=1
1400
1300
1200
1100
1000
900
800
700
700
800
900
1000
1100
1200
1300
1400
10^7
10^6
Counts

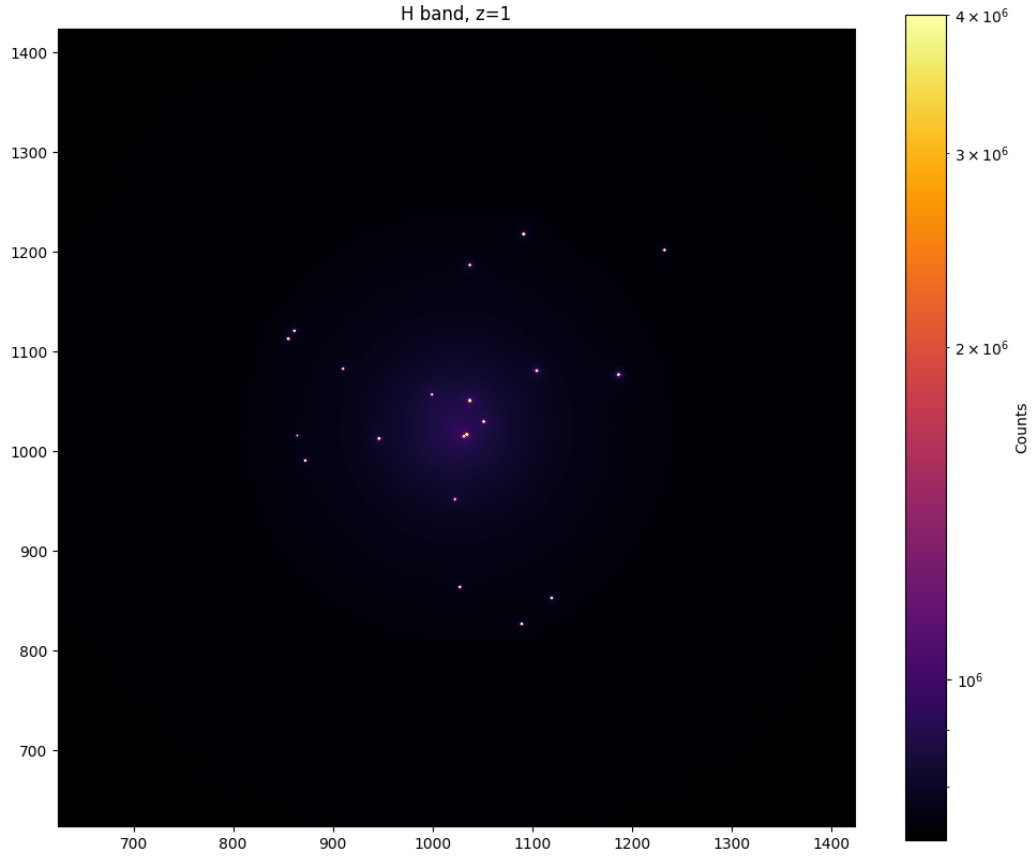
H band, z=1
1400
1300
1200
1100
1000
900
800
700
700
800
900
1000
1100
1200
1300
1400
4×10^6
3×10^6
2×10^6
10^6
Counts

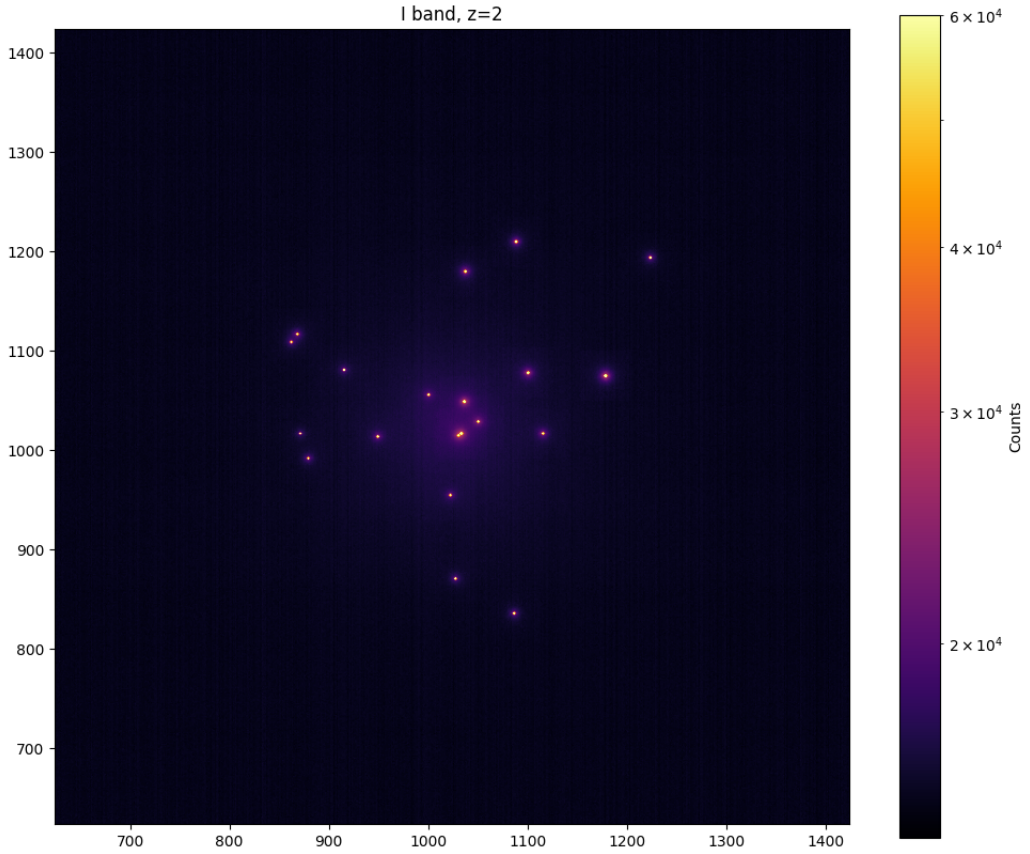
I band, z=2
1400
1300
1200
1100
1000
900
800
700
700
800
900
1000
1100
1200
1300
1400
6 × 10^4
4 × 10^4
3 × 10^4
2 × 10^4
Counts

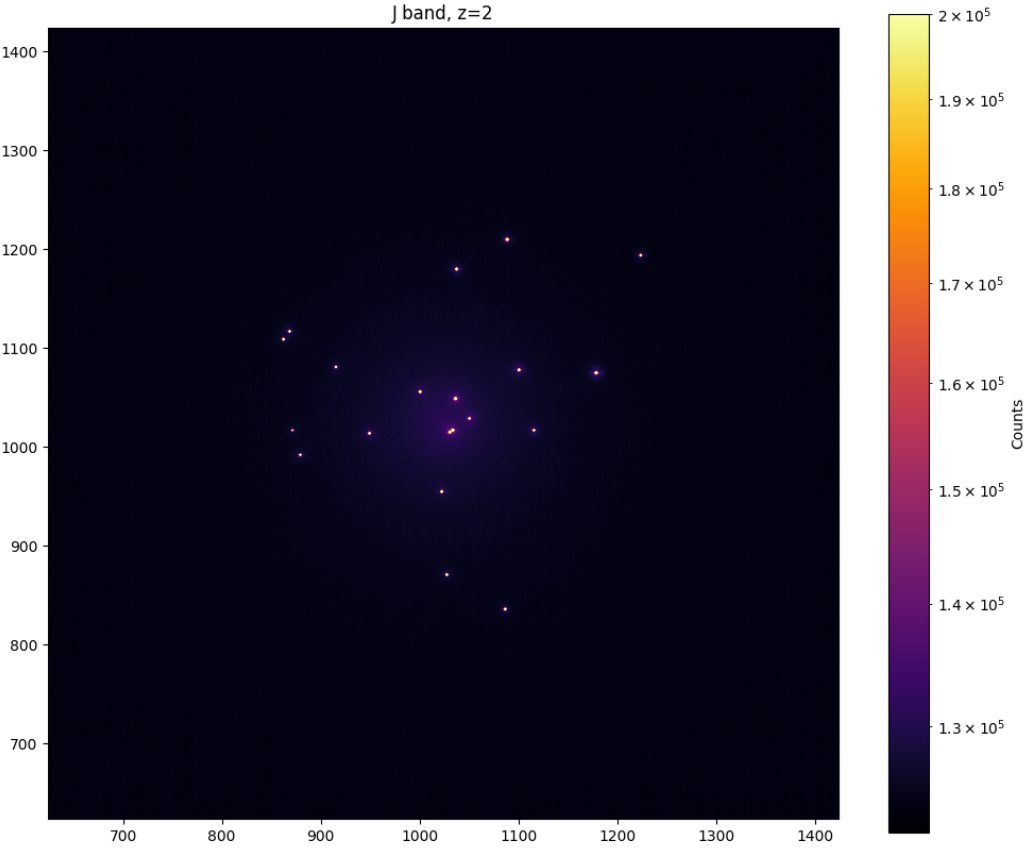
J band, z=2
1400
1300
1200
1100
1000
900
800
700
700
800
900
1000
1100
1200
1300
1400
2 × 10^5
1.9 × 10^5
1.8 × 10^5
1.7 × 10^5
1.6 × 10^5
1.5 × 10^5
1.4 × 10^5
1.3 × 10^5
Counts

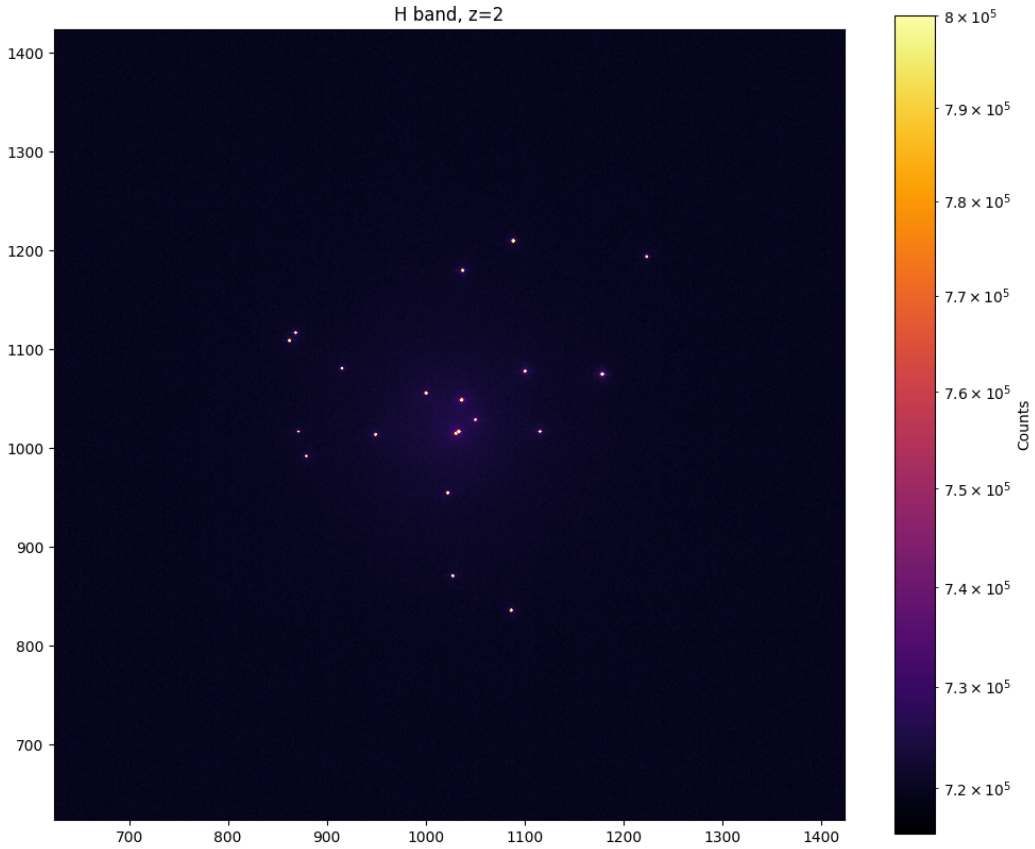
H band, z=2
1400
1300
1200
1100
1000
900
800
700
700
800
900
1000
1100
1200
1300
1400
8×10^5
7.9×10^5
7.8×10^5
7.7×10^5
7.6×10^5
7.5×10^5
7.4×10^5
7.3×10^5
7.2×10^5
Counts

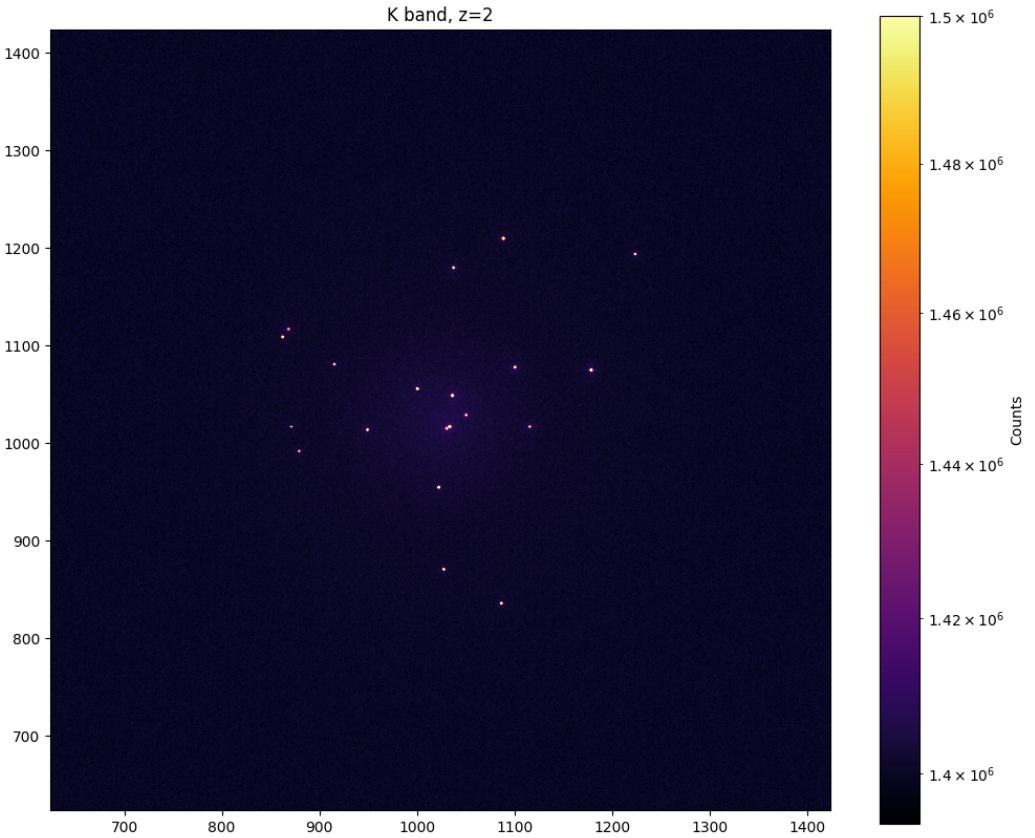
K band, z=2
1400
1300
1200
1100
1000
900
800
700
700
800
900
1000
1100
1200
1300
1400
1.5×10^6
1.48×10^6
1.46×10^6
1.44×10^6
1.42×10^6
1.4×10^6
Counts

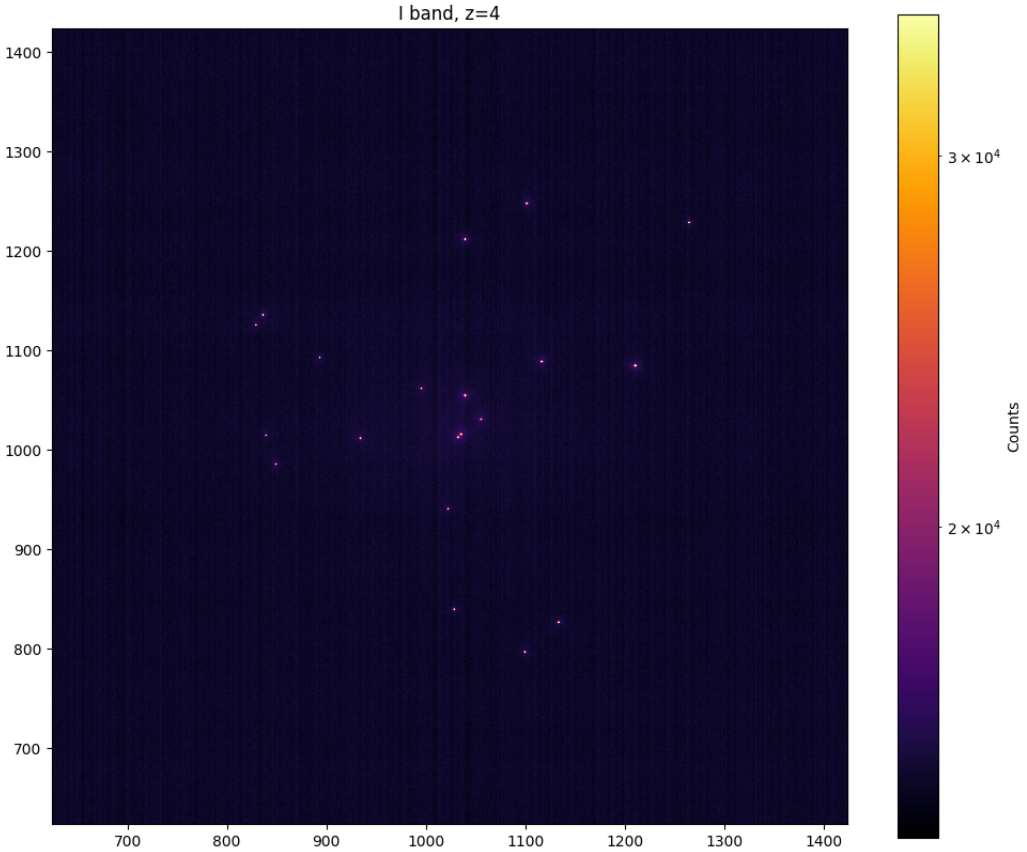
I band, z=4
1400
1300
1200
1100
1000
900
800
700
700
800
900
1000
1100
1200
1300
1400
3×10^4
2×10^4
Counts

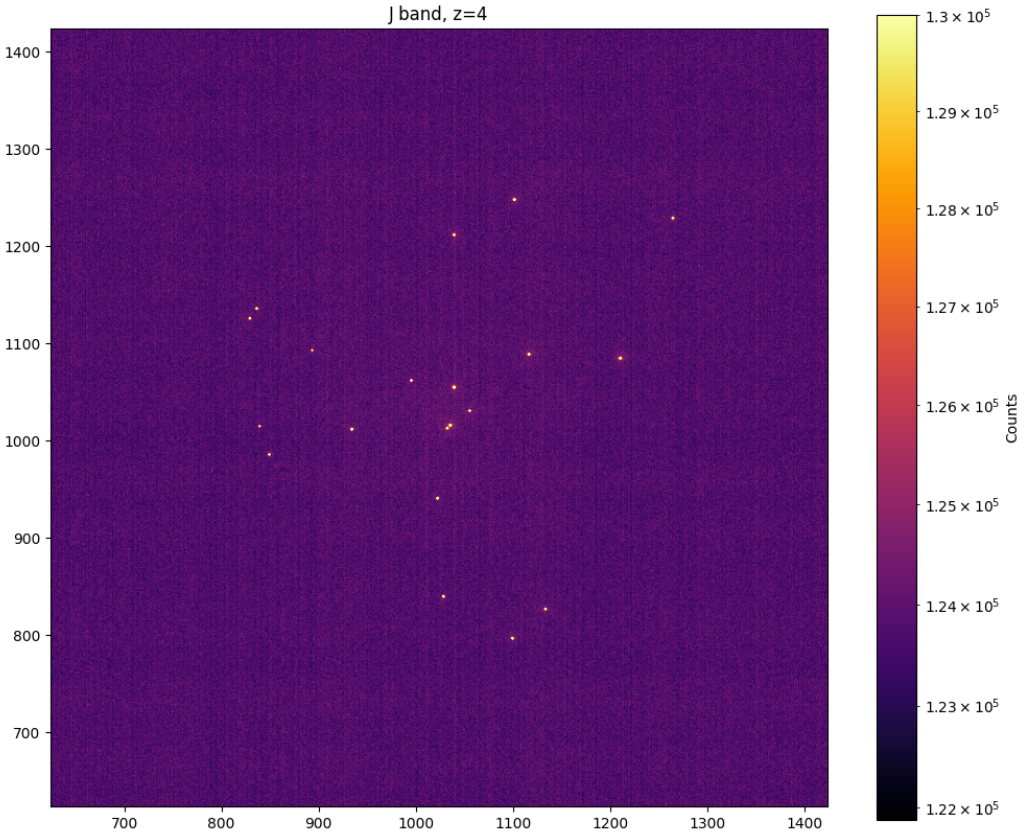
J band, z=4
1400
1300
1200
1100
1000
900
800
700
700
800
900
1000
1100
1200
1300
1400
1.3×10^5
1.29×10^5
1.28×10^5
1.27×10^5
1.26×10^5
1.25×10^5
1.24×10^5
1.23×10^5
1.22×10^5
Counts

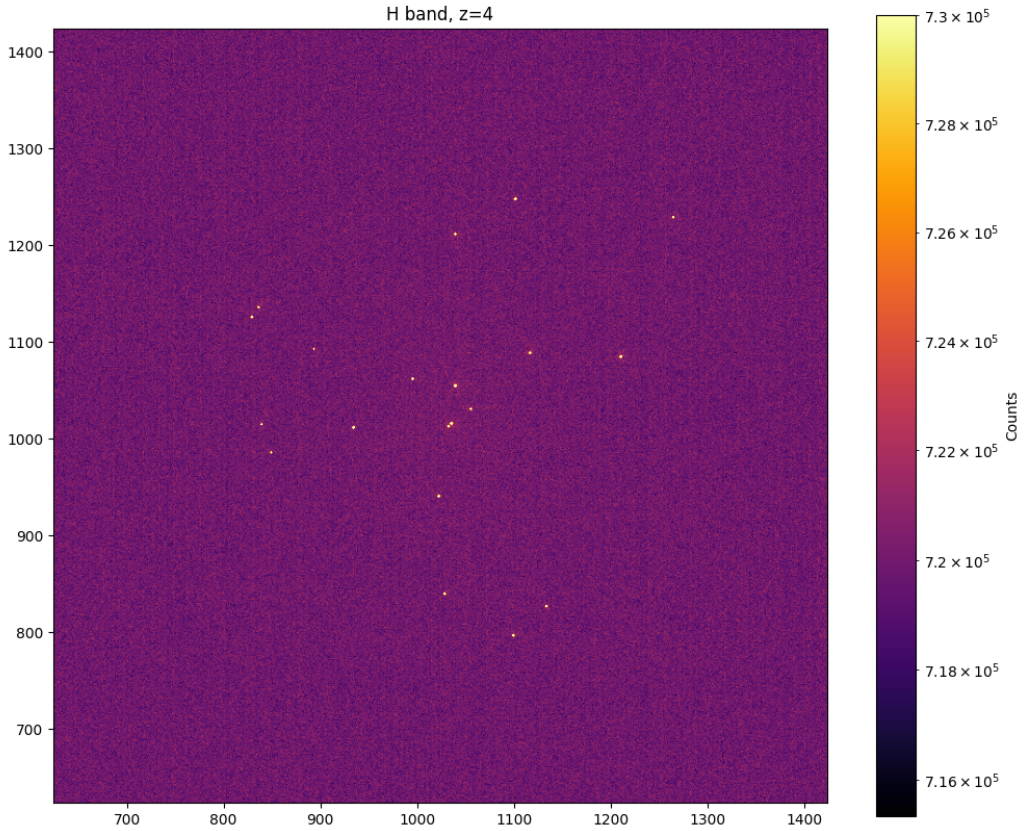
H band, z=4
1400
1300
1200
1100
1000
900
800
700
700
800
900
1000
1100
1200
1300
1400
7.3 × 10^5
7.28 × 10^5
7.26 × 10^5
7.24 × 10^5
7.22 × 10^5
7.2 × 10^5
7.18 × 10^5
7.16 × 10^5
Counts

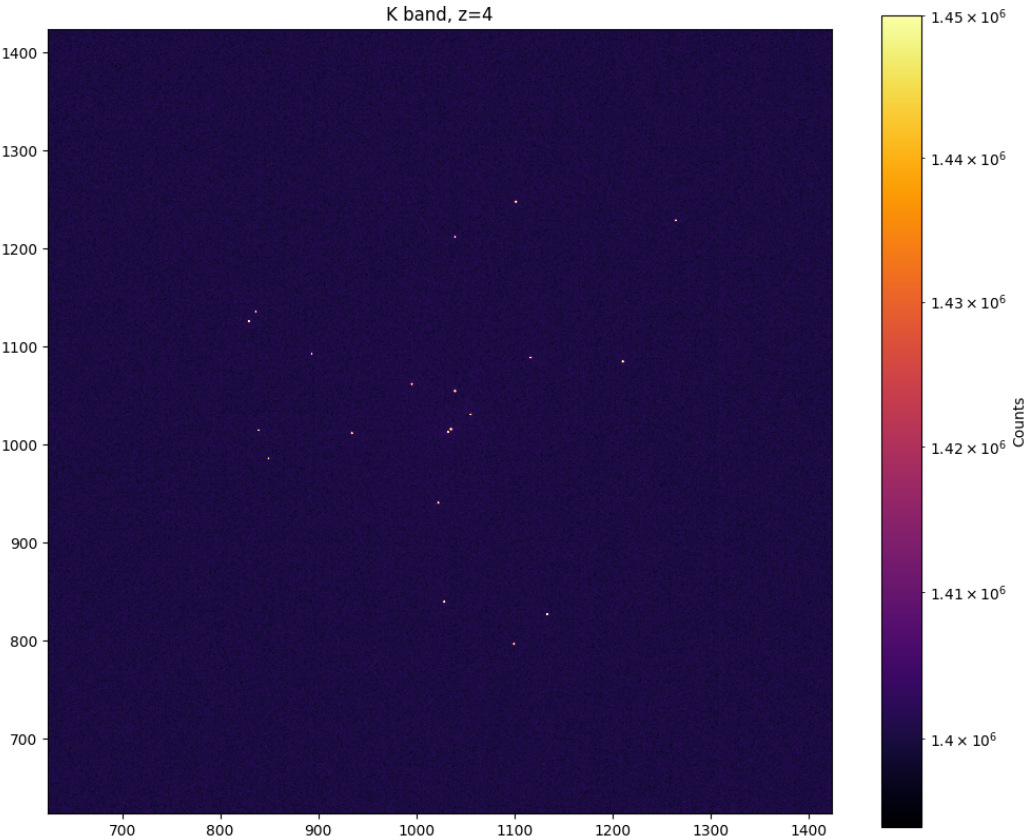
K band, z=4
1400
1300
1200
1100
1000
900
800
700
700
800
900
1000
1100
1200
1300
1400
1.45 × 10^6
1.44 × 10^6
1.43 × 10^6
1.42 × 10^6
1.41 × 10^6
1.4 × 10^6
Counts

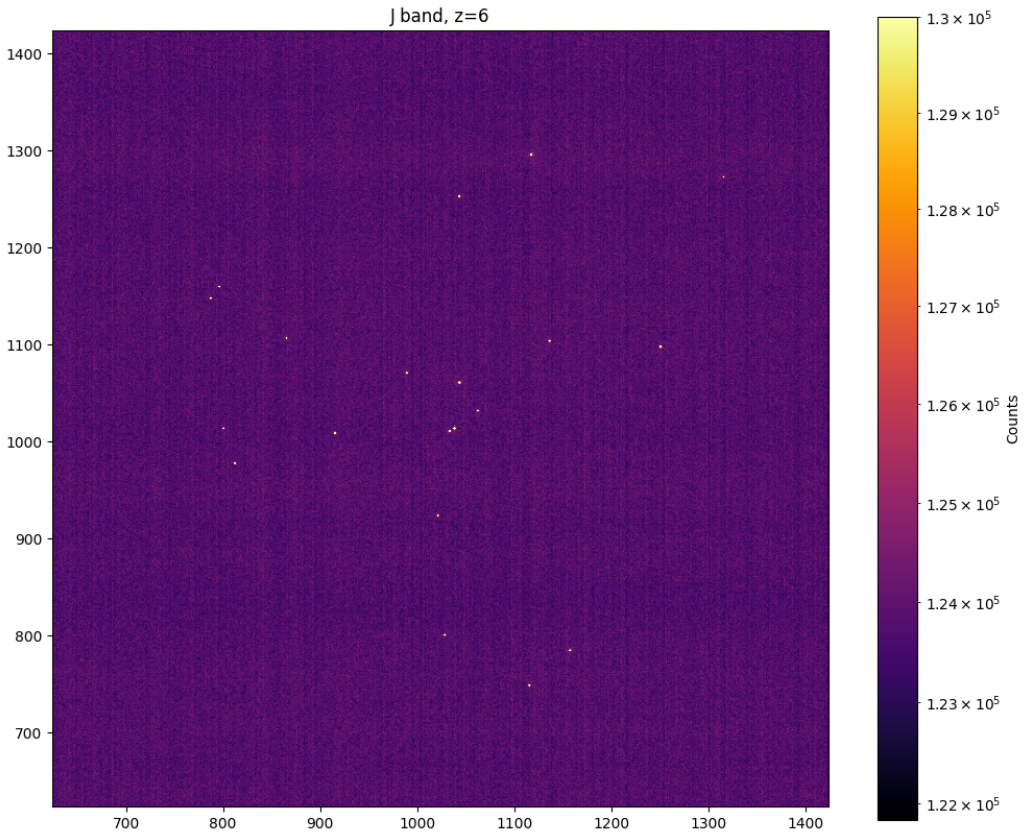
J band, z=6
1400
1300
1200
1100
1000
900
800
700
700
800
900
1000
1100
1200
1300
1400
1.3 × 10^5
1.29 × 10^5
1.28 × 10^5
1.27 × 10^5
1.26 × 10^5
1.25 × 10^5
1.24 × 10^5
1.23 × 10^5
1.22 × 10^5
Counts

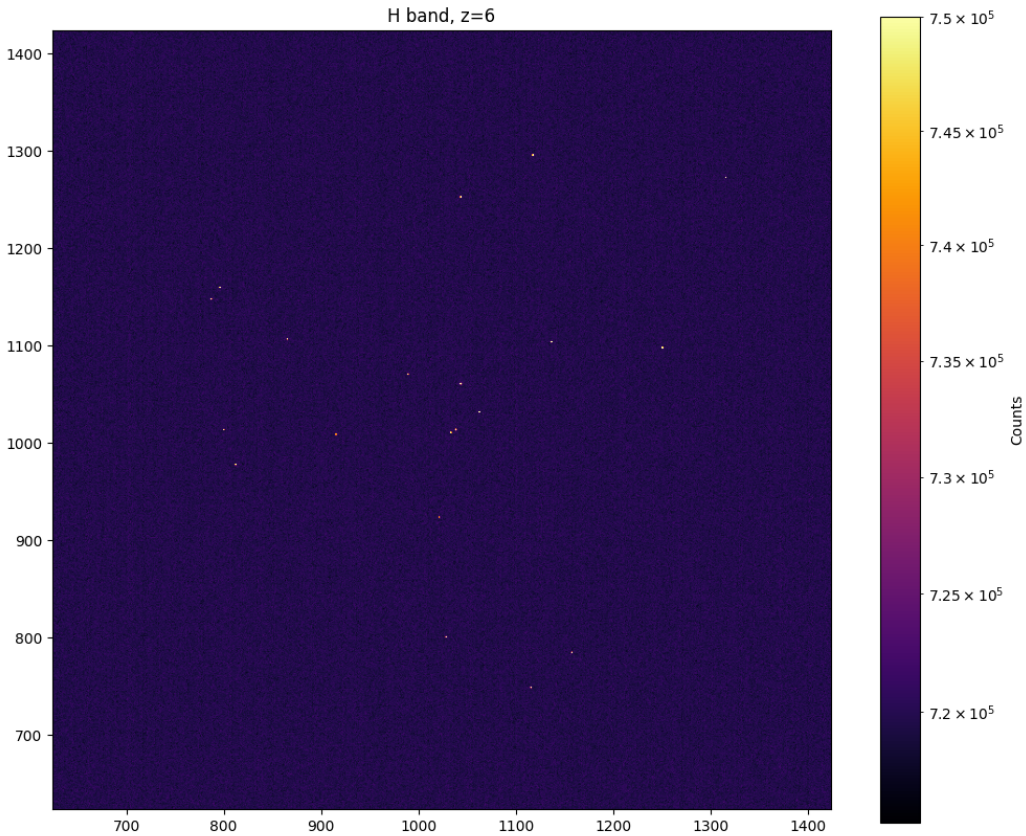
H band, z=6
1400
1300
1200
1100
1000
900
800
700
700
800
900
1000
1100
1200
1300
1400
7.5 × 10^5
7.45 × 10^5
7.4 × 10^5
7.35 × 10^5
7.3 × 10^5
7.25 × 10^5
7.2 × 10^5
Counts

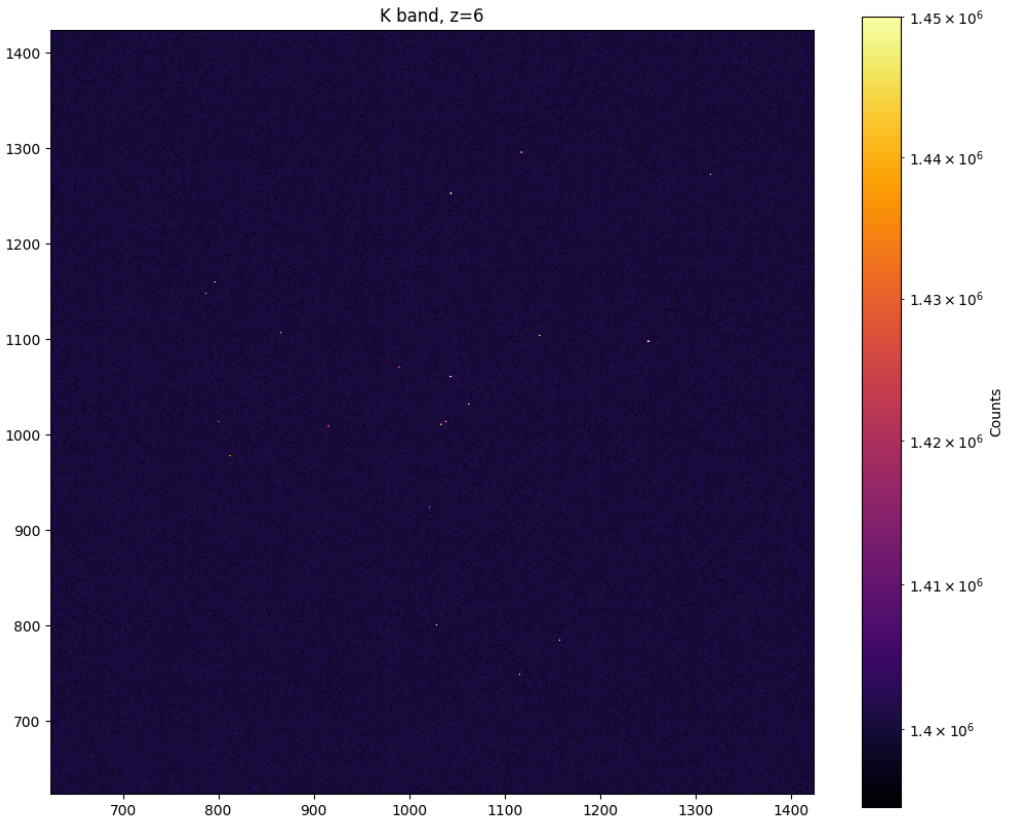
K band, z=6
1400
1300
1200
1100
1000
900
800
700
700
800
900
1000
1100
1200
1300
1400
1.45×10^6
1.44×10^6
1.43×10^6
1.42×10^6
1.41×10^6
1.4×10^6
Counts